Imperial College London
Department of Electrical and Electronic Engineering

Piezoelectric Energy Harvesting From Low Frequency And Random Excitation Using Frequency Up-Conversion

Pit Pillatsch

November 2013

Supervised by Prof. Eric M. Yeatman
and Prof. Andrew S. Holmes

Submitted in part fulfilment of the requirements for the degree of
Doctor of Philosophy in Electrical and Electronic Engineering of
Imperial College London
and the Diploma of Imperial College London

Declaration

I herewith certify that all material in this dissertation which is not my own work has been properly acknowledged.

Pit Pillatsch

The copyright of this thesis rests with the author and is made available under a Creative Commons Attribution Non-Commercial No Derivatives licence. Researchers are free to copy, distribute or transmit the thesis on the condition that they attribute it, that they do not use it for commercial purposes and that they do not alter, transform or build upon it. For any reuse or redistribution, researchers must make clear to others the licence terms of this work

Abstract

The field of energy harvesting comprises all methods to produce energy locally and from surrounding sources, e.g. solar illumination, thermal gradients, vibration, radio frequency, etc. The focus of this thesis is on inertial power generation from host motion, in particular for low frequency and random excitation sources such as the human body. Under such excitation, the kinetic energy available to be converted into electrical energy is small and conversion efficiency is of utmost importance. Broadband harvesting based on frequency tuning or on non-linear vibrations is a possible strategy to overcome this challenge. The technique of frequency up-conversion, where the low frequency excitation is converted to a higher frequency that is optimal for the operation of the transducer is especially promising. Regardless of the source excitation, energy is converted more efficiently. After a general introduction to the research area, two different prototypes based on this latter principle and using piezoelectric bending beams as transducers are presented, one linear design and one rotational. Especially for human motion, the advantages of rotational designs are discussed. Furthermore, magnetic coupling is used to prevent impact on the brittle piezoceramic material when actuating. A mathematical model, combining the magnetic interaction forces and the constitutive mechanical and electrical equations for the piezoelectric bending beam is introduced and the results are provided. Theoretical findings are supported by experimental measurements and the calculation model is validated. The outcome is the successful demonstration of a rotational energy harvester, tested on a custom made shaking set-up and in the real world when worn on the upper arm during running.

Acknowledgements

This is the place where I want to thank all the people that helped me through the completion of my PhD thesis and those who shared the hard and the, far more numerous, great moments with me.

First of all, I want to express my sincerest gratitude to my supervisors Professor Eric M. Yeatman and Professor Andrew S. Holmes. It has always been my opinion that the topic of any project you are working on should come second to the people you are working with. Working with Eric and Andrew has been a great pleasure because of the liberties I enjoyed in choosing my own paths while at the same time being able to rely on their incredible knowledge and support when in doubt.

I also want to thank Michael Riedel and Klaus van der Linden from Johnson Matthey for their help in choosing piezoelectric materials for my application and Lamia Baker from Imperial Innovations for her enthusiasm and relentless efforts to further the commercialisation of the patent that we filed.

I had the chance to work with amazing researchers during my PhD. Among them I want to thank emeritus lecturer Dr. Martin Clark as well as Dr. Paul Mitcheson and his students Alwyn Elliott, James Lawson and James Dicken for fruitful discussions throughout the journey. During my exchange at the University of California, Berkeley I was lucky to work with the bright Dr. Lindsay Miller, one of the most enjoyable researchers to work with I have ever met. Through this collaboration I also enjoyed working with Professor Einar Halvorsen and I am very thankful to Professor Paul Wright for making all this possible.

A thesis can not be completed without financial support and I want to acknowledge the Engineering and Physical Sciences Research Council (EPSRC) for this as well as the Institution of Engineering and Technology (IET) and the Fonds National de la Recherche (FNR) in Luxembourg for various travel grants.

I am not exaggerating when I say that, to me, the Optical and Semiconductor Devices Group is the best working environment I have ever been in. Nowhere else have people been this helpful and shown this much support to each other, sharing many lunch and tea breaks together and welcoming everyone. There are many people that deserve a special mention – "our corner": Emiljana, Aifric, Hadri and William. Tzern, whose patience knows no limits when explaining electronics to me and Susan, without whom I would probably still be waiting for half of my orders at this stage. Dave, Evi, Kaushal, Anisha, Bob, Munir, Krystallo, Taz, Manuel, Alexey, Chen and Mario. I am especially thankful to Edd, who has been a great friend over the last three years.

Outside of Imperial College, Emily will always be a dear friend and I am grateful that I met Julie, who probably does not even know how much of an influence she has had on my life. Hiroki, Maddy, Sandra and Steve belong to that rare group of friends who you know will always be there for you, no matter where in the world you end up being. A big thank you goes to Rosie for making the final stages of writing up and submitting much brighter by her presence.

Finally, I want to thank my parents for still putting up with my "crazy" ideas and without whom not only the PhD would never have been possible. I am also fortunate to have two older brothers who have very different personalities so that I can discuss everything to do with sciences and academia at great lengths with Lex and everything concerning life in general with Luc over a cup of coffee in his garden.

Fir meng Famill – Merci fir alles

"When things are tough, you get tougher." – Chrissie Wellington, four-time IronMan Triathlon World Champion

"What would you attempt to do if you knew you could not fail? [...] when you remove the fear of failure, impossible things suddenly become possible!" – Regina Dugan, director of the Defense Advanced Research Projects Agency (DARPA)

Contents

List of Figures

List of Tables

List of Symbols

Greek Symbols

α_{mag}	Angle of magnetic force	[°]
α	Angle of rotational base excitation	[°]
β	Angle between eccentric proof mass and inertial frame	[°]
γ	Angular deflection of an eccentric proof mass	[°]
δ	Dirac delta function	[-]
δ_{rs}	Kronecker delta	[-]
δ_r	Logarithmic decrement for the r^{th} vibration mode	[-]
ε_{33}^S	Permittivity component in z-direction at constant stress	[F/m]
ε_{ij}^T	Permittivity components at constant strain	[F/m]
ζ_1	Modal damping of the first vibration mode	[-]
ζ_r	Modal damping of the r^{th} vibration mode	[-]
κ_r	Modal coupling term in the electrical circuit equation for the r^{th} vibration mode	[-]
λ_r	Eigenvalue for the r^{th} vibration mode	[-]
$\rho_{\tilde{s}}$	Mass density of substructure layer	[kg/m^3]
$\rho_{\tilde{p}}$	Mass density of piezoelectric layer	[kg/m^3]
η_r	Modal mechanical coordinate for the r^{th} vibration mode	[-]
θ_s	Piezoelectric backwards coupling coefficient for a series connected bimorph piezoelectric beam	[Vm^3/N]
$\tilde{\theta}_r^s$	Modal electromechanical coupling term of the r^{th} vibration mode for a series connected bimorph piezoelectric beam	[Vm^3/N]
$\phi_r(x)$	Mass normalized eigenfunction of the r^{th} vibration mode	[-]

$\phi_s(x)$	Mass normalized eigenfunction of the s^{th} vibration mode	[-]
ω	Angular external excitation frequency	[rad/s]
ω_1	Undamped natural frequency of the first vibration mode in short circuit condition	[rad/s]
ω_j	Undamped natural frequency of the j^{th} vibration mode in short circuit condition	[rad/s]
ω_k	Undamped natural frequency of the k^{th} vibration mode in short circuit condition	[rad/s]
ω_r	Undamped natural frequency of the r^{th} vibration mode in short circuit condition	[rad/s]
Ω_0	Angular displacement limit	[rad]

Latin Upper Case Letters

A	Curve fitting parameter	[-]
A_e	Electrode area	[m^2]
A_r	Modal amplitude constant	[-]
B	Curve fitting parameter	[-]
C	Capacitor	[F]
$C_{\tilde{p}}$	Capacitance of the piezoelectric layer	[F]
$C_{\tilde{p}}^{eq,s}$	Equivalent piezoelectric capacitance for a series connected bimorph beam	[F]
D	Curve fitting parameter	[-]
$\mathbf{D}$	Vector of electric displacement components in the piezoelectric layer	[C/m^2]
D_3	Electric displacement component in z-direction	[C/m^2]
D_i	Electric displacement component	[C/m^2]
D_e	Electrical Damping	[Ns/m]
D_p	Parasitical Damping	[Ns/m]
E	Curve fitting parameter	[-]
E_3	Electric field component in z-direction	[V/m]
E_i	Electric field component	[V/m]
E_{max}	Maximal energy stored in a proof mass	[J]
F_0	Magnetic force at initial gap	[N]
F_{ES}	Electrostatic force	[N]

F_{mag}	Magnetic force	[N]
F_{magz}	Magnetic force component in z-direction	[N]
F_r	Modal force for the r^{th} vibration mode	[N]
F_x	Inertial reaction force in x-direction	[N]
F_y	Inertial reaction force in y-direction	[N]
I	Moment of inertia	[kgm^2]
I_t	Moment of inertia of the tip mass about the free end of the piezoelectric beam	[kgm^2]
L	Beam length	[m]
L_{RT}	Rocking table drive connection to pivot distance	[m]
$M(x,t)$	Internal bending moment term	[Nm]
M_i	Moment	[Nm]
P	Power	[W]
P_{max}	Maximal power that can be converted from the proof mass	[W]
P_{out}	Power output of an energy harvester	[W]
P_{res}	Maximal power that can be converted from the proof mass at resonance under sinusoidal excitation	[W]
Q	Static tip force on a bending beam	[N]
R	Resistor	[Ω]
R_l	Load resistance	[Ω]
R_m	Radius of a semi-circular eccentric proof mass	[m]
$S_1^{\tilde{p}}$	Strain component of the piezoelectric layer in the x-direction	[-]
S_{ij}	Strain component	[-]
T	Transistor	[-]
T_{ij}	Stress component	[N/m^2]
T_r	Period of oscillation of the r^{th} vibration mode	[s]
T_{LT}	Linear table period	[s]
V	Voltage	[V]
V_{peak}	Voltage of the first peak in a decaying waveform	[V]
Y_0	External excitation amplitude	[m]
YI	Bending stiffness term	[Nm^2]
$Y_{\tilde{s}}$	Young's modulus of the substructure layer	[N/m^2]
Z_L	Proof mass travel limit	[m]

Latin Lower Case Letters

$a(t)$	External acceleration	[m/s^2]
a_0	External acceleration amplitude	[m/s^2]
a_{LT}	Linear table acceleration	[m/s^2]
b	Beam width	[m]
$\bar{c}_{11}^E$	Elastic stiffness at constant electric field	[N/m^2]
c_a	Air damping coefficient	[Ns/m]
$c_s I$	Strain rate damping coefficient	[Ns/m]
d	Vertical gap between permanent magnets	[m]
d_0	Minimal vertical gap between permanent magnets	[m]
d_{31}	Piezoelectric strain constant	[m/V]
d_{kij}	Piezoelectric strain constants	[m/V]
d_{cap}	Gap between capacitor plates	[m]
Δd	Relative vertical gap between permanent magnets	[m]
$\bar{e}_{31}$	Effective piezoelectric stress constant $=d_{31}/s_{11}^E$	[Vm/N]
f	External excitation frequency	[Hz]
$f(x,t)$	Distributed force per length	[N/m]
g	Gravity	[m/s^2]
g_{fit}	Gaussian curve fit function	[-]
h	Initial gap between permanent magnet and cylinder proof mass	[m]
$h_{\tilde{p}}$	Thickness of the piezoelectric layer	[m]
$h_{\tilde{p}c}$	Distance between the neutral axis and the center of the piezoelectric layer	[m]
$h_{\tilde{s}}$	Thickness of the substructure layer	[m]
$i_{\tilde{p}}(t)$	Dependent current source of a single piezoelectric layer	[A]
$i_{\tilde{p}}^s(t)$	Dependent current source of the series connected piezoelectric layer	[A]
k	Spring stiffness	[N/m]
$\mathbf{n}$	Unit outward normal vector	[-]
n	Number of oscillations taken into account for the determination of the logarithmic decrement	[-]
n_{ext}	Number of external moments acting on a system	[-]
m	Proof mass	[kg]

m_p	Mass per length of the piezoelectric beam	[kg/m]
m_{mag}	Combined proof and magnet mass	[kg]
r	Distance of an eccentric point mass from the axis of rotation	[m]
r_{mag}	Distance between permanent magnets	[m]
r_{RT}	Rocking table drive shaft offset	[m]
r_x	X-component of the distance of an eccentric point mass from the axis of rotation	[m]
r_y	Y-component of the distance of an eccentric point mass from the axis of rotation	[m]
s_{11}^E	Elastic compliance at constant electric field $=1/\bar{c}_{11}^E$	[m^2/N]
s_{ijkl}^E	Elastic compliance constants at constant electric field	[m^2/N]
t	Time	[s]
$v(t)$	Piezoelectric voltage	[V]
v_{LT}	Linear table velocity	[m/s]
v_{peak}	Exponential curve fit to the peaks of a decaying piezoelectric voltage waveform	[-]
v_{rel}	Relative velocity between permanent magnets	[m/s]
$v_s(t)$	Voltage across a series connected bimorph piezoelectric beam	[V]
$w(x,t)$	Displacement relative to a fixed base	[m]
w_0	Displacement of a cantilever beam under static tip load	[m]
$w_b(x,t)$	Base displacement	[m]
$w_{rel}(x,t)$	Displacement of the beam relative to the base	[m]
x_{LT}	Linear table position	[m]
z_t	Tip displacement of the piezoelectric beam	[m]
z_{mag}	Displacement of the combined proof and magnet mass	[m]

Acronyms

AC	Alternating Current
ADC	Analog-to-Digital Converter
AlN	Aluminium Nitride

BSN	Body Sensor Network
CDRG	Coulomb Damped Resonant Generator
DC	Direct Current
ECG	Electrocardiography
EEG	Electroencephalography
EPSRC	Engineering And Physical Sciences Research Council
FFT	Fast Fourrier Transform
FEM	Finite Element Method
IC	Integrated Circuit
IET	Institution Of Engineering And Technology
IOP	Institute Of Physics
MEMS	Microelectromechanical System
Op-Amp	Operational Amplifier
PZT	Lead Zirconate Titanate
PVDF	Polyvinylidene Fluoride
RF	Radio Frequency
RMS	Root Mean Square
VDRG	Velocity Damped Resonant Generator
WHO	World Health Organization
WSN	Wireless Sensor Network/Node

1 Introduction

This chapter is meant to briefly set the scope covered in this thesis and to outline the research objectives as well as the structure of this document. The literature review in chapter 2 will then provide a much more detailed and specific overview.

1.1 Energy Harvesting and Body Sensor Networks

The market for microelectromechanical systems is forecast to grow from US$8 billion in 2005 to over US$200 billion in 2025 [1] and the market for wireless sensor networks is expected to grow from US$0.45 billion to over US$2 billion in 2021 [2]. This shows the increasing importance of these technological fields. With the ongoing miniaturisation of electronic devices and the accompanying reduction in energy consumption, new ways to power these devices are nowadays in reach. The use of batteries is often inconvenient due to the required maintenance and the resulting cost. In the case of medical implants the need to recharge or replace the batteries is cumbersome since it might result in consecutive surgeries [3].

There are two major solutions to the latter problem being investigated today. On the one side a lot of research effort goes into wireless power transfer methods. In [4], Denisov gives a comparison of the efficiency of ultrasonic and inductive implementations of this principle for power transfer through human tissue. On the other side the field of energy harvesting from ambient sources, such as vibration, thermal gradients, light or radio frequency (RF) electromagnetic radiation is of high interest. The advantage of this approach is obvious. In any type of wireless sensor network (WSN), be it in the surveillance of buildings or in the monitoring of machine tools in a production plant, sensor nodes that are able to power themselves without requiring any maintenance are highly desirable.

Body Sensor Networks (BSN) are a subgroup of wireless sensor networks

and focus purely on monitoring and communicating health related indicators. Diabetes, cardiovascular disease, hypertension, stroke and cancer are major concerns, related to the obesity epidemic society is facing, according to the World Health Organisation (WHO) [5]. Monitoring body functions such as the vital signs, i.e. breathing, heart rate, blood pressure and temperature, or blood oxygenation and glucose levels is beneficial from a medical point of view for fighting diseases. Automated drug delivery systems can be used to optimise the amount of medication administered and reduce adverse effects.

In athletics, knowledge about the body's response to training stress pushes athletes to better performance. Measuring sweat pH, for instance, clearly indicates the risk of dehydration. Soldiers, fire fighters and other professionals who need to work in heavy protective clothing could benefit from this knowledge – only recently two soldiers died from heat exhaustion, the BBC reports [6]. The advent of personal activity trackers such as the fitbit® or Jawbone Up wristband, monitoring the number of steps walked, sleep quality, etc., suggest a general trend for these devices to become part of our lives.

Such systems should provide "fit and forget" solutions. To enhance quality of life, they should go mostly unnoticed. The need for batteries is a major inhibitor here. Energy harvesting, i.e. locally generating electricity from the human body, is tackling this challenge. However, the human body is a very challenging environment. Some of the most common methods of energy harvesting such as solar illumination, thermal gradients and RF do not work well inside the human body – temperature differences are small and tissue attenuation is high (both, for light and RF). Motion energy harvesting suffers from the slow and random motions of the human body.

This research is focussed on methods of energy harvesting tailored to exactly these kind of vibrations. The principle does not exclusively work for human bodies but is generally applicable where low frequency, large amplitude, random vibrations are present.

1.2 Research Objectives

Section 1.1 already gives a brief overview of the general importance of energy harvesting for microelectronics. A large economic growth is foreseen and

the convenience of a perpetual power supply for the ever growing number of electronic devices that are nowadays in use is undeniable.

However, especially for body sensor networks, current implementations are not satisfactory and the devices still suffer from various drawbacks. In the case of scavenging energy from human motion there is still ample room for novel solutions. It is this field that is particularly challenging due to the numerous existing constraints. There are a number of possible applications, such as medical implants for monitoring body functions, automated drug delivery systems and diagnostic tools which could provide better data for further evaluation of a person's state of health. The entertainment and sports industry and general electronic devices could be areas for these technologies, depending on the power requirements of future products. However, it is important to be realistic about these technologies, for instance, the energy consumption of mobile phones is quite high, and laws of physics make it extremely difficult to replace the battery by a micro-generator. Activity tracking devices are a potential application as the power output of a harvester is directly related to the host motion - a device could work as a sensor and generator simultaneously. Ultimately, these technologies have the potential to improve quality of life, which makes this research an all the more worthwhile endeavour. Inertial energy harvesters are promising to provide viable solutions but have to overcome the problems associated with non harmonic, aperiodic excitation combined with the limited available energy due to the generally low frequencies (this will be discussed in section 2.4.2).

The core objectives of this project can be summarised in these bullet points:

- Identifying the potential areas of application where energy harvesting can be used
- Determining the requirements that have to be met
- Analysing the drawbacks of current solutions through literature review
- Developing strategies to overcome these challenges
- Ultimately, implementing these strategies in a prototype device and investigating its performance

1.3 Thesis Structure

The structure of this text is divided into 6 chapters and the outline of each one is as follows:

- Chapter 1 sets the framework for this project and discusses the main objectives and goals.
- Chapter 2 gives a thorough literature review, identifying the current state of the art and the challenges that this thesis will address. Different applications and energy sources for harvesting are discussed before going further into the topics of motion and inertial harvesting. Strategies for low frequency and broadband excitation are laid out.
- Chapter 3 describes the first prototype of a piezoelectric energy harvester with linear proof mass motion and employing the principle of frequency up-conversion. In addition to describing the device, experimental results are presented and a commercial integrated circuit for voltage regulation is evaluated.
- Chapter 4 builds on experiences gained from the linear prototype and the piezoelectric modelling of chapter 5 to introduce a rotational energy harvester, still using frequency up-conversion. The three prototype iterations are described with experimental results and conclusions drawn from each one. For the finalised device, extensive measurements in the real world during running and on a custom built linear table in the laboratory are presented.
- Chapter 5 introduces analytical modelling for piezoelectric bending beams with magnetic actuation. The distributed parameter method for a series connected piezoelectric bimorph beam is adapted to accommodate tip forcing from a set of permanent magnets. The magnetic forces are also modelled. The system is verified trough experimental results both under static initial tip deflection and under magnetic excitation.
- Chapter 6 summarises the findings and original contributions of this research. Suggestions for further work in this area are then given.

2 Literature Review

This chapter presents the literature review, marking the state of the art in the field of energy harvesting. Given that the focus of this research is primarily on vibration energy harvesting for low frequency and random host excitation and more specifically targeted at the human body, the first section will introduce potential applications and sensors for this purpose. This is important in order to base future choices on the actual power requirements.

After that, the broader scope of energy harvesting will be discussed with an introduction on energy sources available for harvesting and the description of a generic flow chart of the different components involved in such a system. This chapter then progressively narrows the field down to vibration based devices and the associated challenges for human motion before discussing the main strategies currently pursued in research to overcome them.

2.1 Sensors and Applications

In section 2.4.2 the physical limits for inertial energy harvesting will be discussed. They are directly linked to the device volume and mass. This means that if the aim is a small system, the power output will be small as well. It is thus highly important to investigate what the power requirements of some potential applications and sensors are in order to judge the feasibility in the first place.

Arguably the most prominent human motion energy harvester that is actually commercially available is built into the Seiko Kinetic range of wristwatches [7, 8]. The Kinetic movement is based on the principle of an automatic, i.e. self-winding, watch. In a purely mechanical design an eccentric oscillating mass, often referred to as the rotor, winds up a coil spring via a ratchet. The energy stored in the spring is then used to power the movement. Instead of the ratchet and spring, the Kinetic rotor acts on a gear box with a ratio of 1:100 that makes a magnetic generator wheel spin at

increased speed. Together with a generator coil, this makes it possible to convert the motion of the wrist into electrical energy for powering a quartz movement. The high gear ratio is needed to generate sufficient output voltages, which nevertheless can barely reach 2 V [9]. Based on data found in the technical guide for the Seiko 5M62A/5M63A caliber [7] a power consumption of 1.25 μW can be assumed for the movement. This, together with the claim that 12 hours of normal wearing provide enough energy for one additional day of run time, i.e. a total of 48 hours, results in an average power output of 5 μW. This is based on assumptions and not experimentally verified, however a range of several μW is a reasonable estimate as a first starting point.

Recently, Kwong [10] gave a good overview of what is feasible at the μW level. On the front-end signal acquisition, EEG sensors are now reaching levels in the range of hundreds of nW and ADCs consume tens of pJ per sample. Further examples include a processor executing an algorithm for epileptic seizure detection at only 0.99 μW (see also [11]) and wireless communication achieved at 440 μW at 1 Mbps [12]. Data transmission is often a bottleneck due to its high demands in power. However, duty cycling or event based transmission and limiting the amount of data that needs to be transmitted [13] are all valid strategies to counteract this problem. A further example of an EEG system can be found in [14], the interesting part being that it is powered purely by body heat. Liu et al. [15] achieved an electrocardiography (ECG) system with an application specific integrated circuit and a 9 μW power consumption.

Chandrakasan provides another review of ultra low power electronics for biomedical applications in [16]. He also arrives at the assumption of 5 μW for the power output of the Seiko Kinetic harvester and a well known implant, the cardiac pacemaker, is listed with a power consumption under 10 μW. Wong et al. achieved an IC for pacemaker applications with a power consumption as low as 8 μW.

Wireless and implantable MEMS based blood pressure and heart rate monitoring systems exist [17, 18, 19] and the device presented by Fassbender et al [20, 21] only requires less than 300 μW while actually transmitting data. Generally, pressure sensors are useful for medical applications; Allen presented the use for wirelessly monitoring aneurysm pressure with an endovascularly-implantable device [22]. He discusses how MEMS based de-

vices that were initially intended for harsh environment use can be adapted to human applications where they need to operate for the remainder of a patient's life. A MEMS sensor for in vivo monitoring of blood oxygenation has been presented by Bingger et al. [23] and is interesting because it is extravascular. This optical sensor can also be used for long term monitoring of pulse and respiratory frequencies.

Bashirullah [24] stresses the importance of in vivo wireless biomedical devices as a major technology driver. He lists the main challenges as coming from trade-offs between implant size, power dissipation and system functionality. He also discusses safety and design considerations for successful systems. Further work on implanted wireless devices is presented by Sawan [25], Yuce et al. [26], Sauer et al. [27] and Huang [28]. Moving outside of the body, Teng et al. produced a very comprehensive review on wearable medical systems for personal health [29].

More recently, sweat pH measuring systems are starting to become of interest as presented by Caldara et al. [30] and Curto et al. [31]. They offer a good indication of a person's state of hydration, which is not only interesting in high performance sports but also for people wearing heavy protective clothing during their work, such as fire-fighters or soldiers. In these situations, body temperature is another variable that can be used, as described in [32] by Moran et al. and Tharion et al. [33], for the evaluation of heat stress by calculating a physiological strain index. Temperature sensors can have very low-power consumption; Lin et al. [34], for instance, presented a device operating at 1 V and consuming 220 nW.

Glucose sensors will become more and more important in the future due to the rising numbers of diabetes patients. Acquiring reliable data is extremely valuable for targeted treatment. Croce et al [35], introduced a CMOS-based continuous glucose monitoring system requiring 140 μW to operate. The interest in this area is not new with research dating back to 1988 by McKean and Gough [36].

In summary, Richard Feynman's view applies here as well, there is plenty of room at the bottom [37], and there already are a number of interesting sensor systems that can operate in the nW to μW range with more to come in the future.

In view of these technological advancements, it is however important to keep the patient and the potential implications in mind. Lodder provides

a highly interesting overview on the long-term performance of various implants [38]. Generally, durability and biocompatibility are major issues. For the example of implantable closed-loop insulin delivery systems it is stated that the battery life of around 7 years is generally acceptable. However, the article also says that 47% of pumps were reimplanted due to battery failure.

The World Health Organization (WHO) provides a good general introduction into medical device regulations [39] and Maisel et al. investigate their safety issues [40, 41, 42]. In a study on the performance of pacemakers and implanted cardiac defibrillators he concludes that 23.6% of malfunctions were due to battery/capacitor abnormalities and 27.1% were due to electrical issues.

2.2 Energy Sources

2.2.1 Overview

It has been discussed already that energy harvesting describes all methods that use energy sources in the surroundings to locally produce electricity. It is then important to have an understanding of which kind of sources are the most promising for each application as this will influence the choice of the appropriate transduction mechanism. Good overviews are given by Chandrakasan et al. in [43, 16] and by Romero et al. with a more specific focus on human power [44].

2.2.2 Solar Energy

Solar energy harvesters encompass all devices that make use of light radiation for energy conversion. They are a very viable option and currently present the highest achievable power output of the presented methods in outdoor use (1500 $\mu W/cm^2$). The big drawback however is that, inside a building or on cloudy days, the power output can drop down to 10 $\mu W/cm^2$ [45]. Furthermore, inside the human body the principle does not work at all for obvious reasons. It is nonetheless interesting for body worn devices and for integration in clothes. The large area available is beneficial here.

2.2.3 Thermal Energy

Thermal energy harvesters make use of the Seebeck effect that describes the conversion of heat energy into electricity. The theoretic maximal power output is limited by the Carnot efficiency, which is dependent on the temperature difference between the hot and the cold side of the device. Furthermore, the actual device efficiency depends on the ZT value, which is a function of a material's Seebeck coefficient, thermal and electrical conductivity and temperature. Skin worn applications generally provide a usable temperature gradient depending on the weather for outside use and on the air conditioning in an office building for example. In industrial applications, thermoelectric generators are commercially available, e.g. for harvesting energy from hot water pipes [46]. Leonov and Torfs show ample work on thermal harvesting from body heat [47, 14, 48] and another example is given by Watkins et al. [49]. Ramadass and Chandrakasan introduced a low startup voltage interface circuit [50]. Mitcheson discusses motion harvesters in comparison to thermal harvesters and concludes that the effectiveness (the ratio of harvested energy to theoretically available energy) of current thermal harvesters can indeed reach up to 70 %, even under small thermal gradients, whereas inertial devices suffer from very low effectiveness values [51]. However, similar to photovoltaic devices, the application inside the human body is limited because temperature differences are very small, if present at all.

2.2.4 Radio Frequency

Visser and Vullers provide a comprehensive introduction into wireless power transport [52]. They make the clear distinction between radio frequency (RF) energy harvesting and RF energy transport. RF energy transport refers to systems using a dedicated source, whereas GSM 900, GSM1800 and WiFi ambient electromagnetic fields are stated as the most interesting for energy harvesting as these are omnipresent and thus qualify as a surrounding source. Piñuela et al. presented a comprehensive study on the available ambient RF power levels in and around London, UK and designed prototype harvesters specific to each band they investigated [53]. Another prototype implementation of an RF energy harvesting wireless sensor node (WSN) was developed by Nishimoto et al. [54].

For human body applications, inductive power delivery systems use a

dedicated source. Denisov compares and discusses inductive and ultrasonic power delivery [4], and Bashirullah explains that wireless powering of biomedical implants is primarily done via low frequency inductively coupled links as this minimises RF heating due to tissue absorption [24]. These systems are interesting and highly useful in a medical environment although they technically fall outside of the category of energy harvesting as discussed earlier.

2.2.5 Mechanical Energy

Mechanical energy has been used for energy harvesting in various forms, such as vibrations [55], fluid flows [56, 57, 58], pressure fluctuations [59], direct forces [60, 61], inertial reaction forces [62] and sound [63]. Commercial harvesters exist for industrial applications, e.g. vibrating machine tools [64, 65]. The use for human body applications has been investigated and since this will be the focus of this research a thorough introduction into vibration energy harvesting will be given in section 2.4.

2.2.6 Glucose

Previously, it was discussed that the monitoring of glucose levels is a major area of research and highly valuable for medical purposes. However, the abundance of oxygen and glucose inside the human body also makes glucose fuel cells an option for implantable energy harvesting. A potential advantage of such devices is the combination of sensing and power generation. One of the problems has been the limited lifetime inside the human body, typically less than 30 days for enzymatic catalysts. However, progress is being made in non-enzymatic and platinum fuel cells and Onescu and Erickson presented a single layer fuel cell, capable of a 2 $\mu W/cm^2$ power output [66].

2.3 Generic Energy Harvesting System

The main purpose of energy harvesting is to transform a present excess energy from the surroundings into a usable form to power a specific application. It is not strictly necessary to produce electricity, a windmill for example can be used to convert wind energy into rotational kinetic energy for milling grains or pumping water. The basic function is common to any

type of device and involves certain steps that are depicted, for the case where electricity is produced, in the flow chart in figure 2.1.

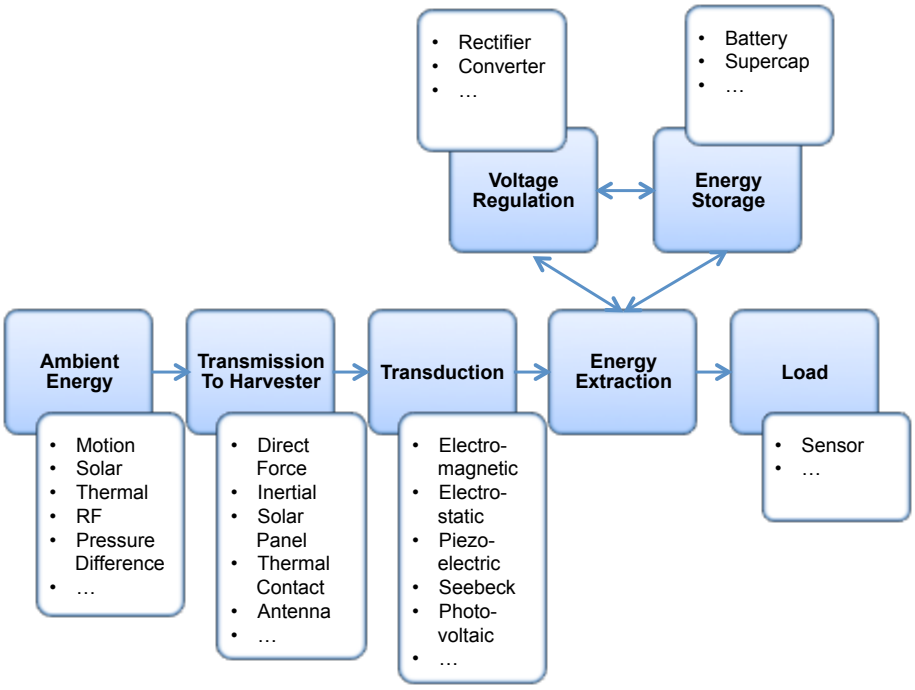

Figure 2.1: General operational flow chart for an energy harvesting system

The first block is reserved for the ambient source as discussed in section 2.2. Without the presence of an initial energy source the entire principle can not work. Vibrations, solar illumination, radio frequency, pressure fluctuations, fluid flows, thermal gradients can all be used as a starting point.

The link between the source and the actual conversion mechanism is represented by the second block. In the case of motion energy harvesting this can be a direct force or an inertial force coupling. Thermal contact would be the link for thermoelectric harvesters.

The third block describes the actual principle of transduction being used. This can be any physical principle that transforms a certain form of energy into electricity. A wide range of possibilities are nowadays under investigation - for motion type harvesters, piezoelectric, electromagnetic and electrostatic implementations have been proven, as will be discussed in detail in section 2.5. The Seebeck effect is the corner stone of thermal harvesting, where temperature gradients are converted into an electric potential and

the photovoltaic effect is applicable to light sources of any kind.

After transformation into electrical energy, circuitry is needed to extract the generated power from the transducers. It might be necessary to rectify and regulate the output voltage. This is strongly dependent on the used mechanism and some of the implications will be explained in section 2.5. A buffer or energy store handles periods of high demand by the load just as well as periods of low supply by the source. These three blocks work together and can be integrated to a certain extent. In other cases, it might not be necessary to include an intermediate energy storage solution.

Finally the last link in the chain is the load that consumes the generated power. In a wireless sensor network this could for example be a simple temperature sensor with data transmission to a central computer.

It should be mentioned that this system constitutes a generic example and that some functionality or blocks can be added and others left out depending on the application. For instance, intermediate energy storage might not always be necessary as for the device described by He [67], where low power pulses representing sensor data are transmitted directly. In the case of frequency tuning for resonant vibration harvesters, the electronic system might be more complex and require a feedback loop that acts upon the transduction mechanism in order to adjust to changing operation conditions. Also, it is important not to lose the overview of the entire system when working on one particular building block as each block can be affected by the preceding and following ones. For this reason energy harvesting platforms incorporating the entire functionality are now becoming of interest (cf. [68] for an example by Bandyopadhyay and [69] for a complete sensor node by Reilly et al.).

2.4 Kinetic Energy Harvesting

2.4.1 Overview

The main focus of this research is on devices for converting human motion into electricity. The purpose of the following sections will be to give an overview of this field, covering resonant energy harvesters and inertial designs. The theory will be laid out and the consequent challenges in body motion harvesting discussed. Vibration energy harvesting has long been a

major research topic, the method proposed by Meninger et al. [55] for example dates back to 2001 and further work on vibration harvesting by the same group of people was presented by Amirtharajah, Chandrakasan et al. in [70, 71]. Other early examples include work on piezoelectric harvesting by Zaitsu et al. [72], efficiency of piezoelectric power generation by Goldfarb and Jones [73] and piezoelectric impact-induced vibration harvesting by Umeda et al. [74, 75]. In terms of human application, Starner provides a good general overview including typical power requirements and potential body locations for energy harvesting [76] and Kymissis et al. [77] as well as Shenk [78] discuss energy harvesting in shoes. Around the same time patents on piezoelectric energy harvesting can be found by Smalser [79] and Kimura [80], utilising a cantilever beam.

Beeby gives an introduction into different vibration sources [81]. Good general overviews of the field are given by Mitcheson et al. [3], Paradiso et al. [82] and by Cook-Chennault et al. [83] with comparisons to non-regenerative power supply systems and a focus on piezoelectric devices. Kim et al. also focus on piezoelectric MEMS devices [84], and work on design considerations and optimisation of the power output has been introduced by Dutoit et al. [85] and Roundy et al.[45, 86].

2.4.2 Power Limits

The principle of an inertial harvester is based on a proof mass moving relative to the device frame. This motion is caused by inertial reaction forces to an external acceleration. One of the big advantages of these devices is that they only require a single attachment point to the host structure as compared to direct force operated devices that usually have two mechanical connections to components that provide a relative motion. For sensor nodes that are installed, for example, on existing machinery, the possibility to just mount a single device in any location is ideal. The conversion from mechanical to electrical energy is achieved through a damping force provided by a transducer. Figure 2.2 shows a schematic drawing of a generic inertial generator with m being the proof mass, Z_L the proof mass travel limit, k the stiffness of the suspension and D_e and D_p the electrical and parasitic damping respectively [87]. The three main types of transduction currently discussed in the literature are electrostatic, piezoelectric and electromag-

netic and they will be introduced in detail in section 2.5.

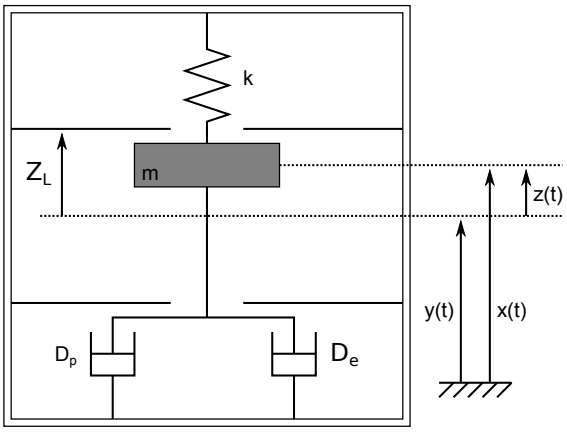

Figure 2.2: Schematic construction of inertial generators [87]

Regardless of the transducer type an upper boundary for the maximally achievable power output by an inertial micro-generator can easily be given. The energy needed to displace a mass is calculated as the product of the force acting on it and the distance of travel. The force is given by the product of acceleration and the mass itself. In case of harmonic excitation with angular frequency ω and excitation amplitude Y_0, the maximum external acceleration of the frame a_0 calculates to $Y_0\omega^2$. Assuming operation in both directions, over the full cycle, the travelled distance sums up to 4 Z_L and the resulting energy calculates to equation (2.1):

$$E_{max} = 4Y_0 Z_L \omega^2 m \tag{2.1}$$

The step from energy per cycle to continuous power is simply a matter of multiplying E_{max} with the excitation frequency $f = \frac{\omega}{2\pi}$ which gives equation (2.2):

$$P_{max} = \frac{2}{\pi} Y_0 Z_L \omega^3 m \tag{2.2}$$

Equation (2.2) gives a theoretic limit under the assumption that the acceleration is constant and a_0 for the entire travel distance, which can never be the case in practice. In [3], Mitcheson et al. use equation (2.2) as a starting point and later on arrive at equation (2.3) for so called velocity-damped resonant generators (VDRG) and coulomb damped resonant gener-

ators (CDRG) under sinusoidal external acceleration at the device resonant frequency:

$$P_{res} = \frac{1}{2} Y_0 Z_L \omega^3 m \tag{2.3}$$

This is more accurate and by a factor $\frac{\pi}{4}$ lower than (2.2). More detailed analysis of the performance limits for the three previously mentioned transduction types is also given by Mitcheson et al. [88, 87].

2.4.3 Human Motion Harvesting

Considering the characteristics of human motion and comparing them with equation (2.3), the challenges become obvious. First of all, the power output is dependent on the excitation frequency, which tends to be very low. Another point is that the excitation is usually highly discontinuous and random; equation (2.3) is valid for harmonic operation at resonance. Furthermore, human motion is generally very large compared to the intended device size. As a consequence resonant devices lose their advantage of dynamically magnifying a small input vibration and are thus not the best solution for this application.

In [89] actual frequency and acceleration measurements were performed on human subjects and discussed. Similar data collection can be found in [90], where the potential of different points on the body for powering specific devices is investigated. A table giving rough guidelines on the predominant frequencies and accelerations at various locations is presented in [91]. For walking subjects under normal gait, the highest excitations were measured at the ankle with up to 2.5 g and 1.7 Hz. The chest, shoulder and wrist sit at the low end, around 0.3 g to 0.5 g and between 1 Hz and 2 Hz. Further examples and discussions of human motion harvesting are given by Miao et al. [92] and Mitcheson et al. [51, 3].

Excitation is a given factor, and so the only handles for maximising the power output are the mass and its travel. This in turn means that the power output is ultimately dependent on the device dimensions, which places a limit on the realistically achievable miniaturisation. One way to optimise the use of the available space is to revert to a high density material, e.g. steel (7.8 g/cm^3), gold (19.3 g/cm^3) or even iridium or osmium (both around 22.6 g/cm^3), for the proof mass. Silicon, with its low density of only

2.3 g/cm^3, is often used for fully integrated devices.

As discussed, the power output is limited by the excitation and the device dimensions. It is then important to improve the overall effectiveness of the transduction. The aim is to narrow the gap between what is theoretically possible and what is achieved in real devices. Most real systems also exhibit varying excitation and require finding methods to increase the operational frequency bandwidth of the device or to adjust its resonance frequency to the excitation. Such strategies will be discussed in section 2.6. The actual mechanism of power extraction can not be neglected either. It can be enhanced by impedance matching between the source and the load. One example is implemented by Toh [93], investigating maximum power point tracking for a continuously rotating harvester designed to power, for example, a pressure sensor for car tires.

In summary, most research questions about human motion harvesting devices revolve around the following points:

- Low frequencies
- Random excitation
- Proof mass size and weight (affects device dimensions)
- Proof mass travel limits (affects device dimensions)
- Host motion amplitude
- Effectiveness of conversion
- Adverse effects on the wearer

2.5 Transduction Mechanisms for Kinetic Harvesters

2.5.1 Categorisation

The main transduction principles used for vibrational energy harvesting have generally been classified into three different categories: electrostatic, piezoelectric and electromagnetic [86]. However, a piezoelectric material, e.g. a bimorph bending beam, can be modelled as a current source in

parallel with a capacitor and so, the piezoelectric principle arguably falls under the broader category of electrostatic harvesters. For this reason, the distinction will be made in this thesis between moving electrode and piezoelectric devices within that category. A novel electrostatic approach based on reverse electrowetting was introduced by Krupenkin and Taylor and is mentioned here as it does not fit either of those two principles [94].

2.5.2 Electromagnetic Transduction

Electromagnetic generators use an arrangement of a permanent magnet and a coil to convert the mechanical energy into electrical energy. One problem with these kind of devices is that the smaller the size, the larger the relative velocity between the two parts needs to be in order to generate high voltages. Otherwise, the voltage needs to be converted to a usable level which is always combined with losses. For larger scale applications however, the principle works well and is commercially available [86]. Examples of such devices have been introduced by Saha et al. [95] and Williams et al. [96] and an interesting concept with a levitating magnet by Wang et al. [97]. Further designs will be discussed in section 2.6. Prabha et al. discuss strategies for increasing electrical damping [98].

2.5.3 Electrostatic Transduction

Moving Electrode Principle

The basic concept behind moving electrode electrostatic transduction is a variable gap or overlap between two parallel capacitor plates. The advantage is that these designs are very suitable for integration in MEMS devices and due to well known processing steps, miniaturisation is relatively easy. The downside is that a high priming voltage is needed in order to achieve the necessary transducer forces while having a gap size between the plates that can still be fabricated. Miao et al. present a device in [92, 99]. Further examples include a multi-dimensional harvester by Galchev [100] and a rolling rod device by Kiziroglou and He et al. [67, 101, 102].

The use of electret materials can eliminate the need for priming voltages and has been investigated by Suzuki and Tsutsumino et al. [103, 104] as well as Boland [9].

In general, there is a distinction between three types of moving electrode devices [86, 62]: in-plane overlap varying, in-plane gap closing and out-of-plane gap closing. The differences between these types are presented in table 2.1 according to Roundy [86]. This table highlights some additional problems arising from the need for small gap sizes such as sticking of the the plates, mechanical stability and parasitic squeeze film damping.

Table 2.1: Comparison of the three types of moving electrode transduction [86]

Out-of-plane Gap Closing	**In-plane Overlap Varying**	**In-plane Gap Closing**
mechanical stops needed due to surface interaction which could cause sticking	no mechanical stops needed	mechanical stops needed due to surface interaction which could cause sticking
largest maximum capacity	lowest maximum capacity, causes high voltage	larger maximum capacity
good stability	stability issues for large deflection	
largest mechanical damping due to squeeze film damping	high Q factor	

Table 2.2 shows the electrostatic force F_{ES} in relation to the gap d_{cap} between the capacitor plates for the three different geometries and the cases of charge constrained and voltage constrained operation, according to Beeby [81]. This is of interest in relation to the earlier discussion about the difficulty in achieving sufficient transducer forces in moving electrode designs.

Piezoelectric Principle

Piezoelectric materials respond to an applied mechanical stress with an accumulation of charge. This effect can be used for the conversion from me-

Table 2.2: Electrostatic force variation for moving electrode devices [81]

Structure	**Charge Constrained**	**Voltage Constrained**
In-plane overlap varying	$F_{ES} \propto 1/d_{cap}^2$	$F_{ES} \quad constant$
In-plane gap closing	$F_{ES} \propto d_{cap}$	$F_{ES} \propto 1/d_{cap}^2$
Out-of-plane gap closing	$F_{ES} \quad constant$	$F_{ES} \propto 1/d_{cap}$

chanical to electrical energy in energy harvesting applications. The IEEE Standard on Piezoelectricity provides a theoretical background [105]. The principle has recently become more and more popular with a number of presented devices such as the sensor module with RF transmission of measurements by Ferrari et al. [106]. There are interesting novel ideas as well, such as piezoelectric grass for turbulence induced vibration by Hobeck et al. [107] and virus-based piezoelectric generation by Lee et al. [108]. The most common piezoelectric ceramic is lead zirconate titanate (PZT), but polymeric transducers have been presented by Pasquale et al. [109] and aluminium nitride is a candidate as well as shown by van Schaijk et al. [110]. Rahman et al. have presented the use of PVDF-graphene nanocomposites [111] and Tiwari and Kim introduced ionic polymer-metal composites [112]. Thin film processes are described for a device by Reilly and Wright [113], thick film methods by Lin and Wu [114] and screen printing by Zhu et al. [115]. Electronics manufacturers are providing integrated circuits specific to the piezoelectric approach [116]. One advantage is that the generated voltages are generally in a usable range and higher transducer forces are easier to achieve. Downscaling in size is slightly more difficult. Integration of piezoelectric thin films in MEMS can result in a reduced coupling coefficient [86, 117].

Figure 2.3 shows the perovskite crystal structure of PZT. Below the Curie temperature, this material exhibits an electric dipole due to distortion of the ideal perovskite structure. After the sintering process of the PZT ceramic,

these dipoles are all in random orientation and the material does not have any piezoelectric behavior yet. During the polarisation process, they are aligned by applying a large electric field and heating the material just below the Curie temperature. This alignment persists after cooling down.

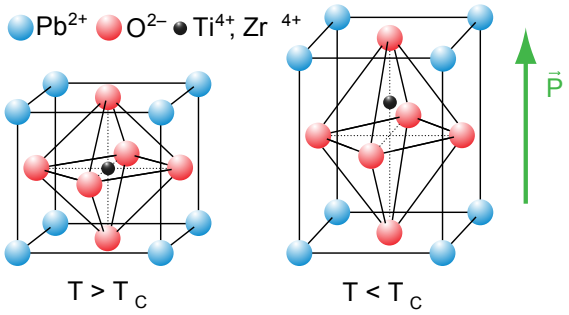

Figure 2.3: Perovskite strucuture of PZT [118]

The linear constitutive equations (the parameters are assumed to be constant regardless of mechanical or electrical load) for the unbounded piezoelectric continuum can be given as follows [105, 119]:

$$\begin{aligned} S_{ij} &= s^E_{ijkl} T_{kl} + d_{kij} E_k \\ D_i &= d_{ikl} T_{kl} + \varepsilon^T_{ik} E_k \end{aligned} \tag{2.4}$$

where T_{kl} are the stress components, S_{ij} the strain components, E_k, the electric field component, D_i the electric displacement component, d_{kij} and d_{ikl}, piezoelectric constants, ε_{ij}, permittivity constants and s^E_{ijkl}, elastic compliance constants. These two equations show the interaction between the electrical and the mechanical properties of piezoelectric materials and are at the basis of the modelling of a bimorph piezoelectric beam that will be presented in chapter 5.

2.6 Strategies for Harvesting Low-Frequency and Random Motion

2.6.1 Resonant Frequency Tuning

One of the problems faced by resonant vibration energy harvesting is that real world systems exhibit changes in frequency over time. This causes a mismatch between the excitation frequency and the narrow optimal operation frequency of many of these devices as investigated by Miller et al. [120, 121, 122]. Various tunable designs offer potential solutions [123], but most of the proposed tuning mechanisms require some form of energy to operate. This means that in order for tuning to be viable, the system needs to improve the power output sufficiently to compensate for the energy that goes into the tuning itself. Tuning mechanisms include the use of magnetic potential wells as presented by Mukherjee et al. [124], the use of permanent magnets introduced by Ayala et al. [125] and systems taking an electronics approach as shown by Mitcheson et al. [126] or Hu et al. [127]. In [128], Roundy explains the difference between active tuning that has to continuously supply power to the mechanism and passive actuators that are able to turn off after an initial tuning.

However, a different interpretation of passive self-tuning can also be justified. Examples exist of devices that are able to tune into resonance without the need to supply energy to the actual tuning, e.g. using spring-stiffening effects on a microelectromechanical device as shown by Marzencki [129]. A system, first presented in [130] by Miller et al., allows passive self-tuning of the device by incorporating a proof mass that can slide along a double-clamped beam. The principle is similar to work presented in [131] by Boudaoud et al., where the resonance of a set-up with a freely sliding bead on a string was investigated. In [132], Miranda and Thomson present a spring-suspended slider that was used with a simple cantilevered beam and Kozinsky [133] investigated a number of systems, one based on a sphere moving inside a cylinder. Gu and Livermore are researching passively self-tuning systems for rotational applications [134, 135].

Possible shortcomings of this strategy include the tunable range that can be achieved and the response time of the tuning mechanism. If the host excitation frequency changes very rapidly and randomly, the system might

not be able to follow.

2.6.2 Broadband Generators

An alternative to tuning the resonant frequency of a harvesting device is to design a system that has a broadband frequency response in the first place and can thus cope with changes in excitation within a certain range. A good topical review is given by Zhu et al. [123]. Within this category there are two approaches that can be considered. The one approach is to combine a multitude of resonant harvesters with different frequency responses on one platform, for instance by using multiple proof masses as described by Petropoulos et al. [136], or by using different geometries of piezoelectric bending beams as discussed by Ferrari et al. [137], by Castagnetti, using fractal methods to determine the beam shapes [138] or by Marin et al. in an electromagnetic implementation [139].

The second approach is to introduce a non-linearity into the system to alter the frequency response. Harne and Wang give a review on recent bistable systems [140] and Beeby et al. compare the power output from linear and non-linear systems [141]. Le et al. introduce power harvesting end stops in an electrostatic device [142]. Abdelkefi et al. designed a structure that undergoes coupled bending-torsion vibrations [143], and the use of permanent magnets to introduce non-linearity has been investigated by Zhu et al. [144], Yang et al. [145], Jones et al. [146], Hadas et al. [147] and Ferrari et al. [148, 149]. Other methods focus on pre-stressing or buckling beams such as the device by Marinkovic and Koser [150], the work presented by Hajati et al. [151, 152, 153] or the piezoelectric buckled beam by Cottone et al. [154]. A general introduction to the nonlinear behavior of buckled beams can be found in [155], by Emam and Nayfeh. Blackburn and Cain discuss the inherent non-linearity of piezoelectric resonance at high power [156].

Broadband systems can work well in many situations, but one of the drawbacks is that they can not match the power output of a tuned resonant device with a high Q-factor at that operation frequency. The achievable bandwidth is another consideration.

2.6.3 Frequency Up-Conversion

The strategies of frequency tuning and broadband harvesting are attractive to cope with varying frequencies. For very low excitation frequencies, in the order of a few Hertz, the frequency up-conversion principle has recently seen a lot of interest for harvesting motion energy. The proof mass is put in motion by a low frequency external acceleration, the transduction mechanism however, is actuated at its natural frequency through a catch-and-release or plucking mechanism. This requires a low stiffness, low Q-factor suspension of the proof mass so that the actual proof mass motion exhibits a large range of operation frequencies. The main advantage of this strategy is that the actual energy conversion always happens at an optimal frequency, regardless of the excitation frequency. This favours an increase in conversion effectiveness - crucial when dealing with low kinetic energy available for instance in human applications.

One such device based on piezoelectric beams actuated by teeth with an attached roller can be found in [157] by Zhang et al. Galchev et al. have presented two different devices relying on this principle, the first one with two electromagnetic generators that are plucked by a magnet that is suspended in the middle between them [158] and the second one operating in a similar way with piezoelectric transducers [159, 160]. Zorlu and Rahimi et al. introduced an electromagnetic harvester that plucks a beam carrying a coil [161, 162] similar to a device presented by Kulah and Sari et al. [163, 164, 165]. Another electromagnetic device is shown by a different group around Ashraf et al. [166].

Plucking or flicking piezoelectric beams to then let them ring down naturally has been especially popular. For instance, Pozzi et al. presented a direct force knee joint harvester with plectra actuating a number of piezoelectric beams in [167, 60, 168, 169]. A similar set-up is used by Janphuang and Isarakorn to harvest energy through a gear wheel, plucking a piezoelectric beam [170]. Impact driven piezoelectric devices have been presented by Gu et al. [171, 172], Jacquelin at al. [173] and Renaud at al. [174, 175]. Further strategies for harvesting energy from low frequencies with up-conversion techniques on piezoelectric beams were described by Rastegar and Murray [176, 177] and examples on the MEMS scale are given by Fu et al. [178], Liu et al. [179] and Lee et al. using a micro-fabricated ridge shape to actuate a

probe [180]. All these methods cause an impact on the brittle piezoceramic and can lead to chipping and damage to the material.

To avoid physical contact between the piezoelectric beam and the actuator, a number of people have investigated magnetic actuation systems such as the linear systems by Yang and Tang et al. [181, 182, 183] or the piezoelectric windmill presented by Luong et al. in [184]. These systems work by opposing permanent magnets. Wickenheiser et al. take an approach of opposing wells in a patterned magnetic material to a permanent magnet in [185, 186].

This strategy appears to be the most promising for human motion applications and will therefore be the basis for the two prototypes that will be presented in chapters 3 and 4.

2.7 Rotational Devices for Human Motion

So far this literature review has presented many examples of harvesters with linear proof mass motion. Such devices are arguably easier to achieve with MEMS fabrication processes, which might explain why they are such a popular topic of research. However, rotational systems do exist, e.g. the micro-fabricated permanent magnet generators by Arnold and Das et al. [187, 188, 189], Herrault et al. [190, 191, 192] or Fralick et al. [193]. Hergert shows the design of micro-ball bearings that can be used for such MEMS devices [194]. On a larger scale, the continuously rotating harvester by Toh et al. [93, 195] has been mentioned before.

Based on experience with the first prototype linear device presented in chapter 3, the author believes that rotational structures do have advantages for human motion. That device uses a rolling rod as a proof mass and actuator, plucking piezoelectric beams. While the results were promising, this system can only work well in environments where the device orientation is known, for example for bridge monitoring. In the human body this is not the case and if the device is tilted too far, the rolling rod will simply remain at the lowest point and no energy will be harvested at all.

Figure 2.4 shows a basic model of the operating principle of the follow-up device from chapter 4. An eccentric proof mass is free to rotate around its axis and carries a permanent magnet. A piezoelectric beam is fixed on the outer casing (not shown in this figure) such that its tip, with a

second permanent magnet, is facing the magnet on the rotor. Under external excitation the rotor will move and swing its magnet past the tip magnet on the beam, which causes an initial deflection of the beam tip. After release, the beam rings down at its natural frequency and electrical energy can be extracted. The idea of an eccentric proof mass itself is not new. It has been discussed earlier in the context of the Seiko Kinetic wristwatch [7] and has also been successfully used by Romero et al in an electromagnetic harvester [196]. The introduction of magnetic piezoelectric beam plucking into such a device is novel however.

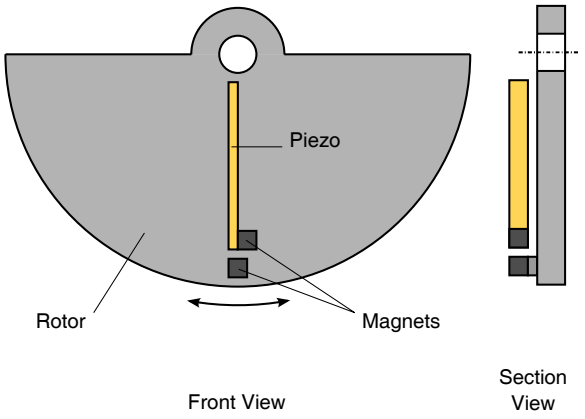

Figure 2.4: Principle of operation of the rotational beam-plucking energy harvester

An advantage of this rotational set-up is that the proof mass has no inherent motion limit, it can continuously rotate depending on the excitation. An investigation on rotational and gyroscopic proof masses for energy harvesting was introduced by Yeatman [8] and the absolute maximum power for such a device, based on the kinetic energy stored in the proof mass, was found to be:

$$P_{max} = \frac{\omega^3 \Omega_0^2}{4} I \tag{2.5}$$

with ω the angular excitation frequency, Ω_0 the excitation amplitude and I the mass moment of inertia of the rotor. For a semi-circular proof mass of constant thickness and density, $I = mR_m^2/4$, with m being the total mass and R_m the radius. As discussed for the very similar linear case in [3], this

equation assumes that the rotational acceleration is constant and maximal over the whole travelled angle. This is why equation (2.5) represents an absolute maximum and the achievable power in practical terms will be lower.

To further the understanding of the dynamic behaviour of this system, the configuration depicted in figure 2.5 was studied. Essentially, a point mass at a distance r from its axis of rotation (the z-axis in this figure) is considered under gravity and external excitation. The distances r_x and r_y describe the proof mass position and F_x and F_y are the corresponding inertial reaction forces caused by linear external excitation. Gravity g acts in the negative y-direction. The angle γ is the angular deflection of the proof mass in relation to the y-axis. The angle α represents rotational base excitation, i.e. rotation of the device enclosure, and β is the resulting angle between the mass and the inertial frame, i.e. the one that determines the capability of harvesting energy from the relative motion, with $\gamma = \alpha + \beta$.

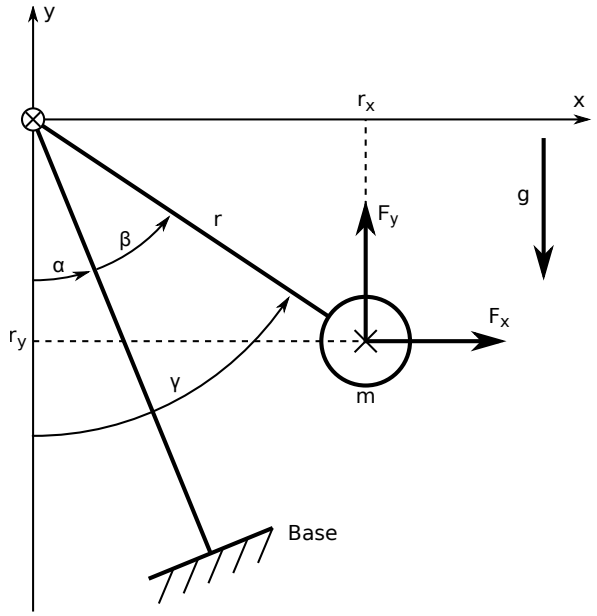

Figure 2.5: Schematic view of an eccentric proof mass under external excitation

In a first analysis, ignoring the effects of damping and the transduction mechanism, the basic equation of motion for rotation states that the angular acceleration $\ddot{\gamma}$ multiplied by the mass moment of inertia I equals the sum of all n_{ext} external moments M_i acting on the the mass:

$$\ddot{\gamma} I = \sum_{i=1}^{n_{ext}} M_i \tag{2.6}$$

In the case of a simple point mass at a distance r from the rotational axis, the moment of inertia around this axis is given as $I = mr^2$. Application to the system of figure 2.5 gives:

$$\ddot{\gamma} I = F_x r_y + (F_y - mg) r_x \tag{2.7}$$

Including the identities $r_x = r\sin(\gamma)$ and $r_y = r\cos(\gamma)$ and the fact that $\gamma = \alpha + \beta$ we can finally write:

$$(\ddot{\alpha} + \ddot{\beta}) I = F_x r \cos(\alpha + \beta) + (F_y - mg) r \sin(\alpha + \beta) \tag{2.8}$$

Examining the above equation makes it clear that the rotational design can accept linear excitation in x and y-directions and rotational excitation, which makes it more versatile in situations where the orientation of the device is variable and where the host motion is random in multiple degrees of freedom, as is usually the case in the human body.

Under gravity and rotational excitation, the rotor behaves like a pendulum. If the base is rotated, the rotor simply stays in its position, resulting in γ being zero. The excitation being given as α, the relative motion between the base and the rotor becomes $\beta(t) = -\alpha(t)$.

Figure 2.6 shows the solution of equation (2.8) without rotational excitation ($\alpha(t) = 0$). The rotor is only subject to sinusoidal excitation in the x-direction at 2 Hz and 10 m/s^2 (zero-to-peak) in figure 2.6 (a), and the frequency is increased to 4 Hz in (b). The result is that now $\beta(t) = \gamma(t)$ and there is still a relative motion between the rotor and the base, although it is chaotic. In this scenario the device is behaving purely inertially. In most real applications there will be a mixture of these extreme cases of pendulum and inertial motion and, as can be seen in part (b), depending on the excitation, the rotor can go into continuous rotation. It is important to stress that these figures represent calculation results based on a simplified rotor shape corresponding to the prototype in section 4.3 and do not include any damping or the effects of the magnetic coupling. The calculated pendulum natural frequency of the rotor is 5.6 Hz, and figure 2.6 (b) shows that it can flip over and go into continuous rotation even at excitation frequencies

below this value.

The mechanical modelling in this section is in many ways similar to work presented by Toh in [195] for an electromagnetic rotational harvester with continuous power point tracking. The difference is that in his system, the eccentric proof mass ideally remains stationary at a certain angle, such that the gravitational torque opposes the transducer forces. Furthermore, with the focus being on continuous rotation, Toh does not discuss the cases of random or linear excitation.

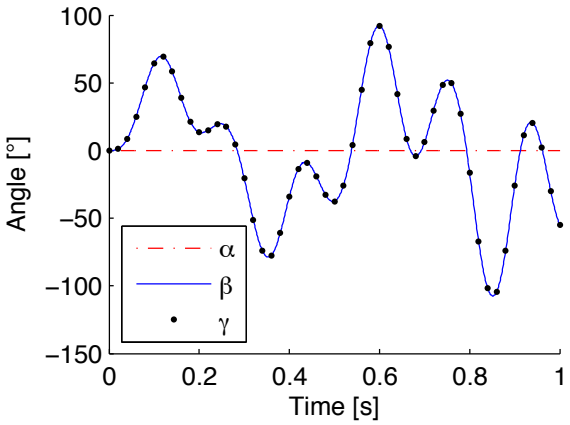

(a)

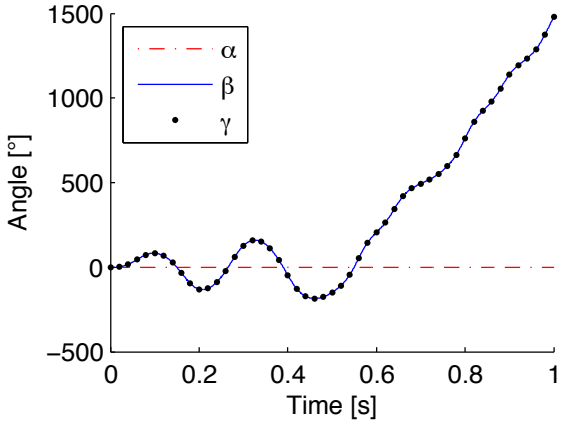

(b)

Figure 2.6: Rotor motion under linear excitation in x-direction with 10 m/s^2 and 2 Hz, (a), and 4 Hz, (b)

3 Frequency Up-Converting Piezoelectric Rolling Rod Harvester

This chapter introduces a large scale model of a piezoelectric energy harvester with linear proof mass motion. The transduction mechanism relies on a series of piezoelectric bimorph beams that are magnetically plucked by a rolling cylinder. The reasoning behind the design and the set-up will be explained and measurement results shown and evaluated. Additionally, a commercially available integrated circuit, specific to harvesting applications and offering voltage regulation, is tested. The majority of the chapter is based on an article published in the Institute of Physics (IOP) Journal of Smart Materials and Structures [197].

3.1 Introduction

In order to improve a technology it is necessary to have a look at the key limitations first. For human motion, these have been discussed in section 2.4.3 and, as a reminder, equation (2.2) for the maximally achievable power output can be written as:

$$P_{max} = \pi f a_0 Z_L m \tag{3.1}$$

where $f = \omega/2\pi$ is the excitation frequency expressed in Hz, a_0 is the external acceleration amplitude, Z_L is the internal displacement limit and m the mass of the inertial mass. This equation assumes a sinusoidal excitation with acceleration $a(t) = a_0 \sin(\omega t)$. Alternatively, a_0 can be expressed in terms of the external motion amplitude Y_0 and the angular excitation frequency ω as $a_0 = Y_0\omega^2$. Equation (3.1) gives an upper boundary regardless of the actual transduction mechanism as it calculates the mechanical

kinetic energy that could in an ideal case be extracted from the proof mass and converted. Furthermore, since the displacement limit Z_L is included, this equation holds true for resonant designs where Y_0 is smaller than Z_L, just as well as for non resonant devices in the case where Y_0 is much larger than Z_L, as is the case for human motion.

As mentioned previously, the theoretic expression in (3.1) only takes the kinetic energy stored in the proof mass into account. In actual devices the conversion mechanism itself is a significant bottleneck. The available energy is small, so the effectiveness of the transducer needs to be as high as possible. The effectiveness describes the percentage of the available inertial energy that is actually converted into electrical energy. This is where frequency up-conversion with its two step approach is advantageous. The proof mass periodically transmits an impulse to the actual transducer which then vibrates at a higher frequency. The electromechanical coupling is improved.

A common misconception is that the ultimate power limit increases due to the higher operation frequency of the transducer. This is not the case. Such a device is still limited by the kinetic energy of the large proof mass. The achieved improvements are a matter of operating the transducer under its ideal conditions. For example, increasing the frequency of the relative motion between the magnets and coils of an electromagnetic mechanism helps reaching higher output voltages.

A key characteristic of frequency up-converting harvesters is their broad bandwidth. Each time the transducer is actuated, a fixed amount of energy, defined by the properties of the mechanism, is converted. If the excitation frequency increases, the number of transducer actuations increases as well and with it the achieved power output. This relationship is illustrated in figure 3.1 for a device with parameters $Z_L = 2.5\,\text{mm}$, $m = 6.1\,\text{g}$ and $Y_0 = 100\,\text{mm}$. At the resonance frequency, the power output of a device with continuously optimised damping and spring constant increases according to equation (3.1). In practical terms however, a tuning mechanism capable of achieving this indefinitely is impossible.

The power output of the frequency up-converting design will follow the line in the graph throughout the entire range as the relationship between power output and frequency is now linear. In theory, the only limit to the working frequency range occurs at the lower end. If the excitation is too small, the proof mass fails to actuate the transducer at all, which is indicated

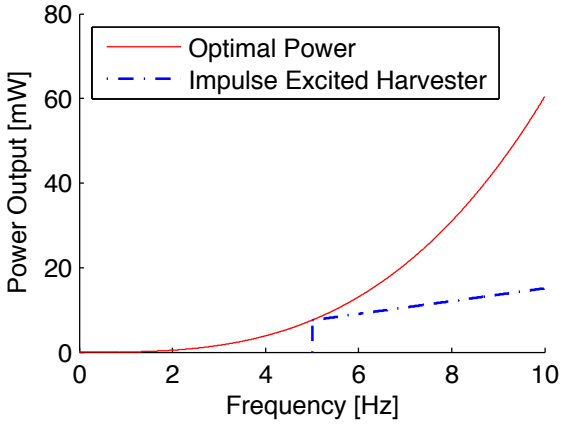

Figure 3.1: Comparison of the impulse-excited harvester to the optimal power output

by the drop in the curve at 5 Hz. As will be discussed later, this is the case for the presented prototype when the proof mass cylinder gets stuck on the magnetic coupling and its travel is thus impeded. The cylinder will only be released once the external acceleration passes a certain threshold that allows it to overcome the coupling force.

It is also important to note that the broadband operation of frequency up-converting harvesters can only be achieved if the proof mass motion itself displays a broadband frequency response. Due to the lack of suspension in the rolling cylinder device and the rotational design in chapter 4, this is true in both cases.

3.2 Rolling Rod Harvester Design

Figure 3.2 shows the proof-of-concept model. It addresses a number of the previously mentioned challenges for human body energy harvesting. An external steel cylinder is used as a proof mass because of its higher density. An electrostatic device with a rolling rod was developed in our group before [67], but the coupling over the given travel range was low. Consequently, a piezoelectric approach was used for the energy conversion. A series of bimorph piezoelectric beams acts as a distributed transduction mechanism. The tip of each beam holds a permanent magnet. When the proof mass rolls over one element, the magnet snaps on to the steel cylinder and the

beam bends, illustrated in the section view of figure 3.3. As the proof mass continues its travel, the beam is released and oscillates freely at its damped natural frequency.

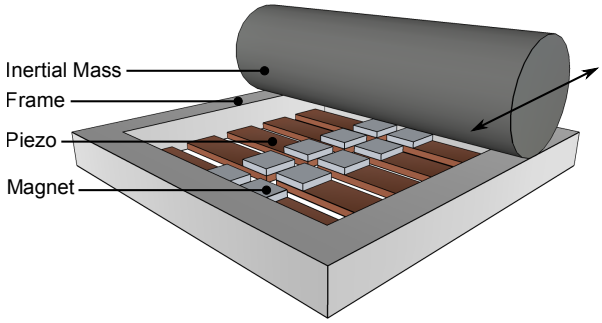

Figure 3.2: Frequency up-converting piezoelectric harvester prototype

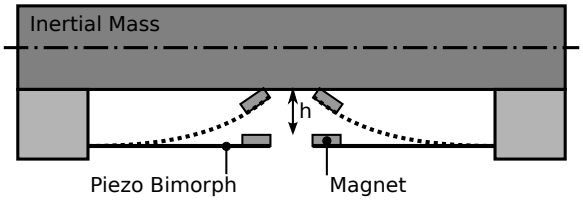

Figure 3.3: Section view of the prototype, showing the bending of the beams

Other novelties of the device are perpendicular directions of proof mass motion and transducer actuation. In other designs, the travel range of the proof mass was often limited by the actuation range of the transducer. This drawback was encountered in parallel plate electrostatic devices, e.g. [3], where a trade-off between a small initial gap, necessary to achieve high transducer forces, and the resulting reduction in overall travel had to be made. With the new approach, the actuation forces can be spread over a larger number of individual transducers and adjusted by changing their geometry. This is illustrated in figure 3.4, based on the theoretic device described in the introduction (section 3.1), and assuming an initial gap between magnet and cylinder $h = 1\,\mathrm{mm}$. The figure shows the required transducer force that each single beam needs to provide for optimal operation as a function of excitation frequency. It can be seen that, for any given frequency, the individual transducer force becomes smaller when the number of transducers is increased, as one would expect. Piezoelectric beams can be made in

various thicknesses and the added ability to adjust the device is of interest. This segmented transduction also plays a role in extending the bandwidth, as will be discussed in the results section.

However, there is one drawback to the distributed transducer that places a limit on the number that is ultimately going to be used. Due to the way the beams are actuated, they will all oscillate out of phase and so the outputs can not simply be put together for power processing. Each beam needs individual circuitry at least to a certain extent. Section 3.5 will further elaborate this topic.

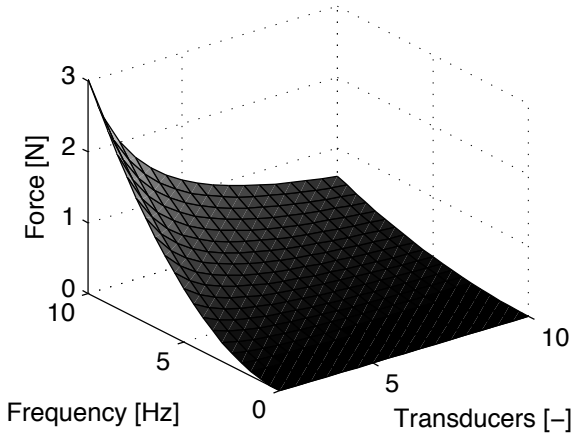

Figure 3.4: Transducer force for each individual beam in relation to number of transducers and frequency

3.3 Measurement Set-Up

The macro scale functional model depicted in figure 3.5 has been built for proof-of-concept. Two different cylinders were machined from mild steel, one with a mass $m_1 = 285$ g and one with half the mass $m_2 = 143$ g, in order to compare their influence on the power output. Two rails, adjustable in height, constrain the travel to linear motion with two blocks acting as variable end stops. On each side, a clamping mechanism holds a total of eight piezoelectric beams. The latter were cut to a size of $74 \times 5 \times 0.5$ mm out of a series connected bimorph plate by Morgan Electroceramics. The top and bottom layers are made of their PZT 507 material and are 0.2 mm in thickness. The center shim consists of a 0.11 mm FeNi alloy layer. These

beams were clamped to a free beam length of 60 mm which, together with the added tip mass of the $5 \times 5 \times 1$ mm N52 type neodymium magnets, ultimately resulted in a damped natural frequency $\omega_1 = 46.3$ Hz in this configuration.

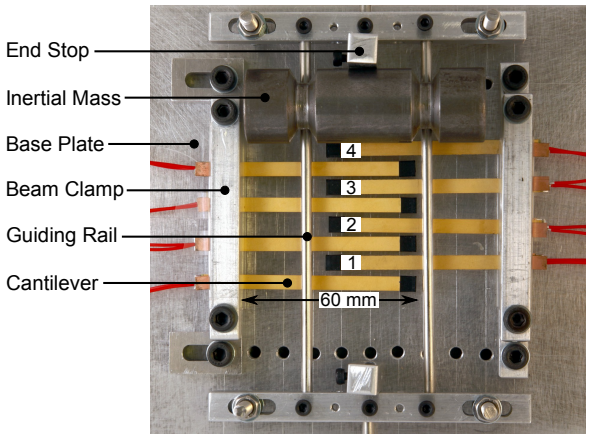

Figure 3.5: Functional model of the impulse-excited harvester

A component analyser measurement showed a capacitance $C_{\tilde{p}}^{eq,s} = 30$ nF for each single beam. In accordance with the output impedance magnitude of the beam, i.e. $1/\omega_1 C_{\tilde{p}}^{eq,s}$, the matched resistive load for maximal power output was determined as $R_l = 120\,\mathrm{k}\Omega$. The corresponding values in the results section were calculated as the measured root-mean-squared (RMS) voltage squared divided by this load resistance.

The mechanical schematics of the functional model mounted on a rocking table that was used for reproducible excitations can be seen in figure 3.6. The angular velocity ω of the driving wheel is adjustable between 20 and 120 rpm, 0.33 and 2 Hz respectively. This motion is transferred to the platform through a connection rod giving a sinusoidal excitation:

$$a(t) = g\frac{r_{RT}}{L_{RT}}\sin(\omega t) = a_0 \sin(\omega t) \tag{3.2}$$

where L_{RT} is the distance between the rotational axis of the platform and the mounting point of the connection rod and g is the gravitational acceleration. The radius r_{RT} stands for the eccentric position of the connection rod on the driving wheel. By changing r_{RT} the tilt angle of the table can be set. At angles of 16.1° and 5.1°, a high acceleration $a_1 = 2.7\ \mathrm{m/s^2} \approx 0.28$ g

and a low acceleration $a_2 = 0.87\ \mathrm{m/s^2} \approx 0.089\ \mathrm{g}$ were confirmed with an accelerometer measurement. In the results section the four possible configurations between masses m_1, m_2 and accelerations a_1, a_2 will be compared and discussed.

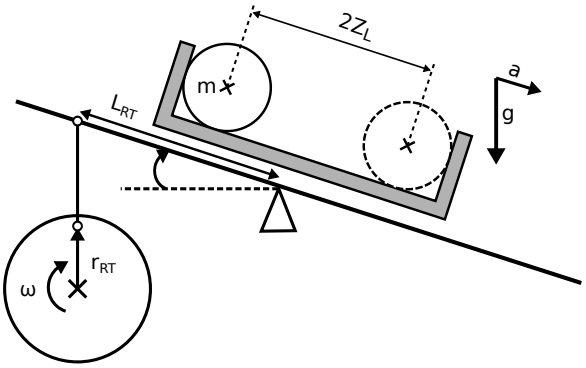

Figure 3.6: Mechanical schematics of the measurement set-up

The last component of the measurement set-up is the Linear Technology LTC3588-1 piezoelectric energy harvesting power supply [116]. A number of electronics companies have released specific chips for energy harvesting. The LTC3588-1 contains a full wave bridge rectifier and a DC-DC converter with selectable regulated output and an input voltage range between 2.7 V and 20 V. With a 3×3 mm package its footprint is very small. The internal block diagram as well as the external components that were used are shown in figure 3.7. The values were chosen according to recommendations in [116] and are summarised in table 3.1. The operation and performance of this chip will be evaluated.

Table 3.1: External components for Linear Technology LTC3588-1 energy harvesting power supply

Symbol	**Value**
$C1$	1 µF
$C2$	4.7 µF
$C3$	47 µF
$C4$	10 µF
$L1$	10 µH

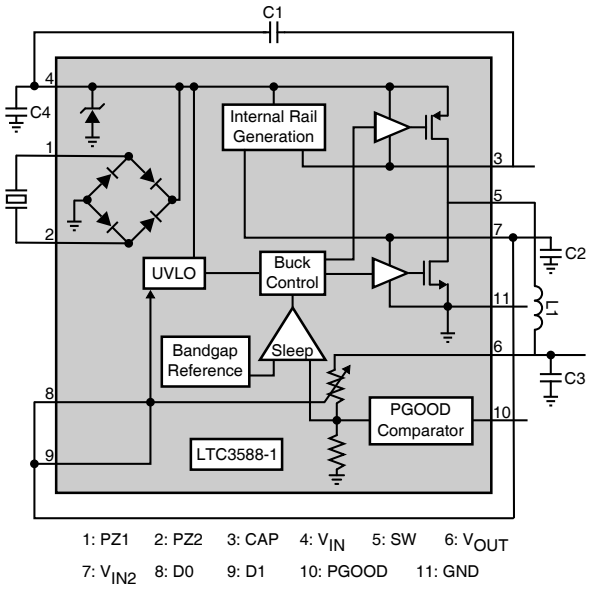

Figure 3.7: LTC3588-1 voltage regulator, internal diagram (shaded) and external components, after [116]

3.4 Results

3.4.1 Device Operation

The open circuit voltage measured on a single beam for one actuation is shown in figure 3.8. This result can be interpreted by reference to figure 3.9. When the proof mass approaches the beam, the magnet latches onto it, pulling the tip of the beam up (point 1 in both figures). Initially, the beam stays in this deflected position as the cylinder continues its travel. In a second phase the corner of the magnet holds on to the proof mass and the beam is pulled up further due to the curvature of the cylinder, before finally being released and vibrating freely (point 2). This is in fact an ideal scenario, since the release happens exactly after the equilibrium where the beam force and magnetic attraction match. The higher frequency vibration observed between point 1 and point 2 is likely due to the initial shock caused by the magnet snapping to the proof mass.

Figure 3.10 shows continuous operation at 0.33 Hz. The oscilloscope used had four input channels, with measurements performed only on one side on beams 1 to 4 (cf. figure 3.5). The symmetry of the device makes it

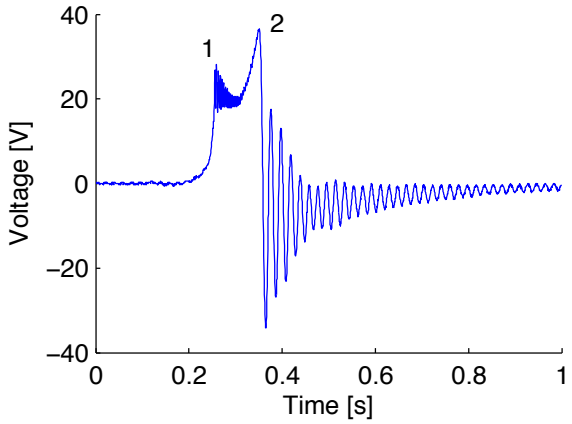

Figure 3.8: Single beam actuation at 0.33 Hz

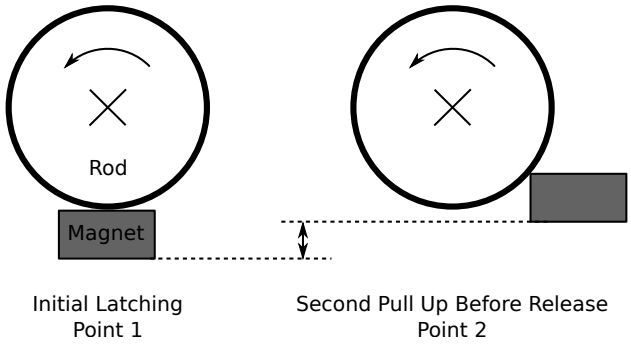

Figure 3.9: Magnet position during one pass of the proof mass

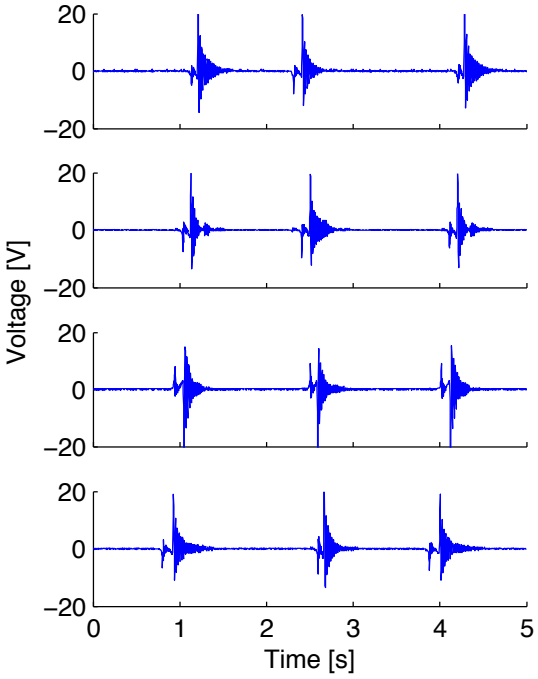

Figure 3.10: Voltage output at 0.33 Hz with impedance-matched resistive load (beam 1 at the bottom to beam 4 at the top)

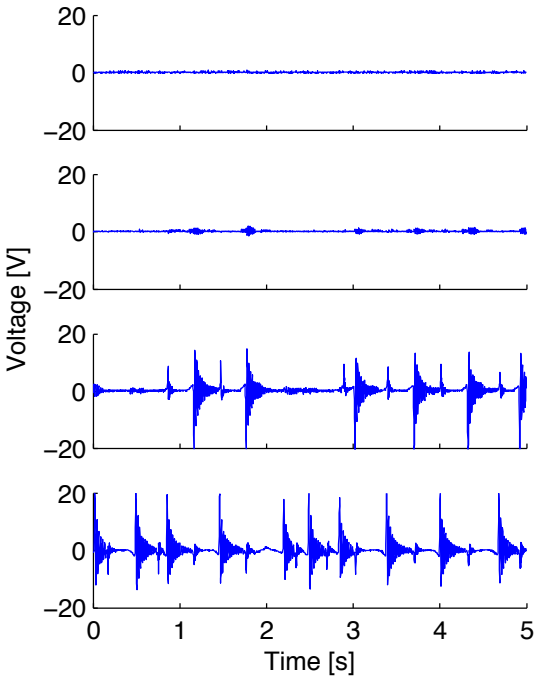

Figure 3.11: Voltage output at 1.66 Hz with impedance-matched resistive load (beam 1 at the bottom to beam 4 at the top)

possible to simply double the obtained power output to get the total value. The proof mass was released at the end stop on the side of beam 4 and the time difference between the peaks in figure 3.10 for the different beams accordingly shows that beam 4 is actuated first, followed by beam 3, etc. After passing beam 1, the cylinder hits the other end stop and reverses its travel, this time consequently actuating beam 1 first. It can be seen that the oscillation of the individual beams has completely died off before the next actuation.

Continuous operation at a higher frequency of 1.66 Hz is shown in figure 3.11. Here, the previously mentioned advantage of the segmented transduction becomes visible. The proof mass does not travel the full range at this setting, nevertheless it keeps "hovering" between beams 3 and 4. Despite the rather random movement of the rod indicated by the time differences between excitations, and despite beams 1 and 2 not getting actuated at all, it is still possible to extract power at this higher frequency. Thus the band-

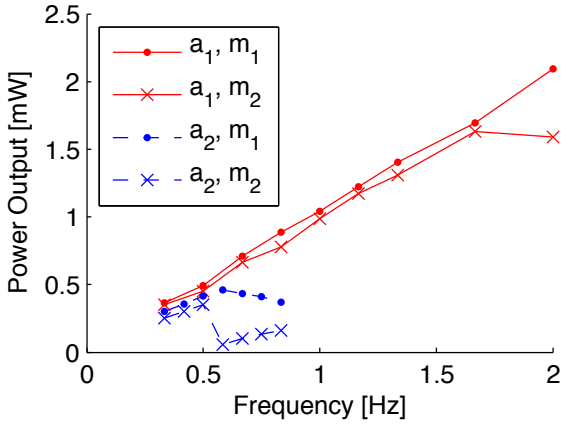

Figure 3.12: Measured total power output for the four configurations

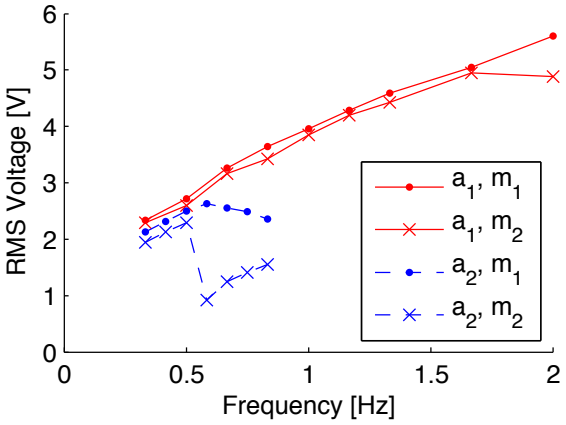

Figure 3.13: Measured RMS voltage for the four configurations for a single beam

width has effectively been increased by the multiple beam arrangement.

In figures 3.12 and 3.13 the measured power output for the whole device and the corresponding RMS voltage on a single beam can be seen for the four described measurement configurations with different proof masses and external accelerations. The first thing to notice is that the power output curves, especially for the large accelerations in solid red, do follow the expected linear behaviour, i.e. the power output doubles with doubled frequency. The obtained RMS voltages on each beam mainly stay within a quite usable range between 2 and 6 V, never dropping far below 1 V.

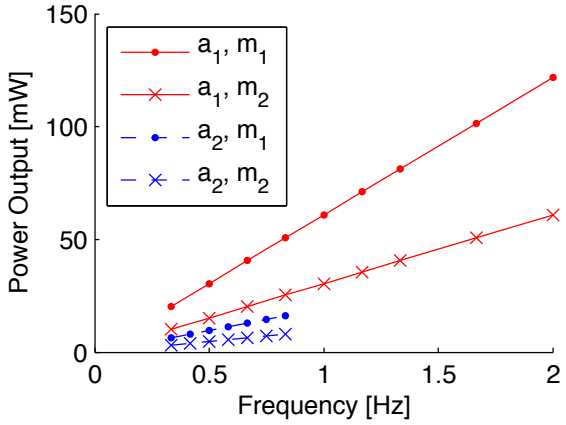

Figure 3.14: Theoretic maximally achievable power output for the four configurations

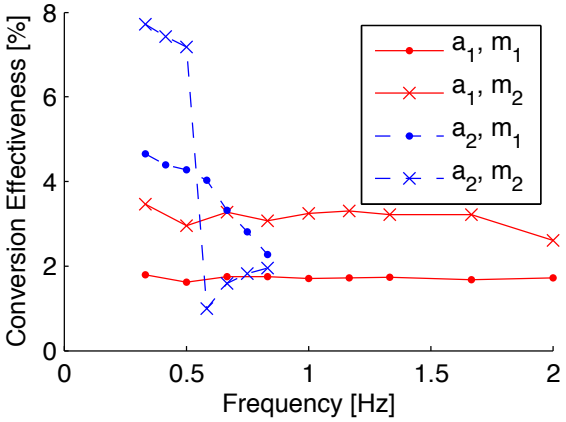

Figure 3.15: Effectiveness of power conversion

In contrast, figure 3.14 depicts the theoretic maximum power output according to equation (3.1). This graph helps to explain some of the effects that were noticed in the experimental procedure. In theory, doubling the proof mass or doubling the acceleration should double the power output; this was not the case in the experiments for the reasons described below.

In order to best describe the different cases of operation of the device, the lower acceleration a_2 was deliberately chosen so that the lighter proof mass m_2 just manages to travel the full range. It barely touches the end stops, whereas at acceleration a_1 heavy end stop collisions occur, which essentially

indicate a dissipation of excess energy that could not be converted. Ideally, the device should be operated at the lower acceleration with light proof mass, because this is the case with the best match between the available kinetic energy and the energy the transducers can extract during each cycle.

The measured power output reflects this quite well. Up to about 0.5 Hz all four curves are very close to each other. The two solid red lines for high acceleration show that, despite the fact that there is a higher energy stored in the heavier proof mass m_1, the transducers are not able to extract it and there is virtually no gain compared to the lighter proof mass m_2 up to a frequency of about 1.7 Hz. At this frequency the experiment showed that m_2 did not travel the full range any longer and the power dropped consequently.

The findings for lower acceleration a_2 (blue, dashed lines) are very similar, with the major difference being that the break-down point occurs at a lower frequency around 0.5 Hz for m_2 and around 0.7 Hz for m_1. This is to be expected as the kinetic energy of the proof masses is smaller under lower acceleration. It is also noticeable that the break-down is not quite as steep for m_1, since, although it does not travel the full range, it does still actuate some of the beams. Overall, an absolute maximum of 2.1 mW was achieved at 2 Hz.

The effectiveness of the power conversion, i.e. the percentage of available inertial energy that was actually converted into electrical energy, depicted in figure 3.15 is in line with the previous discussion. The theoretic power output was calculated using (3.1) for each of the configurations, and the graph shows which percentage of this value was achieved in each case. The effectiveness reaches its best result of almost 8% in the case where the proof mass just about touches the end stops and very little energy goes lost in collisions, as was to be expected. This confirms that a proper match of the transducers for the predominant excitations and the intended proof mass is necessary. However, this is a choice that can be made while designing a device and needs to be done only once, eliminating the need for active frequency tuning. For example, an adaptation towards higher proof masses could be done by choosing thicker beams; this makes it possible to extract more energy due to the stronger piezoelectric coupling.

In fact, figure 3.15 also shows that the effectiveness stays level across the entire operation range, which proves the large bandwidth capabilities

of frequency up-conversion. In the case of large excitations this results in a six fold frequency range, limited here by the constraints of the rocking table rather than by the device.

Finally, the experiments result in a power density of 3.8 to 13 $\mu W/cm^3$ with proof mass m_2 at high acceleration $a_1 = 2.7\ m/s^2 \approx 0.28$ g and under excitation frequencies between 0.33 and 2 Hz. In comparison, in [171] by Gu, a power density of 25 $\mu W/cm^3$ is stated, but this was achieved at a four times higher frequency of 8.2 Hz and higher acceleration of 0.4 g. From the figures shown in [171] the best bandwidth seems to lie between 5 and 11 Hz, which is a 2.2 fold frequency range, compared to the six fold range shown in this proof of concept. Galchev and his colleagues have chosen an acceleration of 1 g at a frequency of 10 Hz to test three of their impulse-excited devices in [160]. The power densities at these excitation parameters are between 2.7 and 10.7 $\mu W/cm^3$. The particular device shown in [160] operates at frequencies between approximately 10 and 35 Hz, a 3.5 fold range.

The rotational beam plucking device presented by Pozzi in [168] can not be directly compared to this work as it is not an inertial device and the values shown by Renaud in [175] are only theoretic. Unfortunately, Yang does not provide enough data about the device to allow calculation of the power density [183]. Especially considering the low operation frequency, this work thus compares very favourably to similar devices for human body applications, both in terms of power density and frequency range.

3.4.2 Voltage Regulator

The LTC3588-1 voltage regulator was tested on a single beam under high acceleration a_1 and with the lighter proof mass m_1 between 0.33 and 2 Hz. Figure 3.16 shows the start-up at 0.87 Hz with no load. The first graph shows the voltage as obtained by a differential measurement on the two terminals of the piezoelectric beam. The second graph shows the voltage at the V_{in} pin (cf. figure 3.7) and the third one is the regulated voltage output. First, the voltage from the piezoelectric beam is rectified to charge the input capacitor connected to V_{in}. As soon as a threshold of 5 V is reached, an amount of charge gets transferred to the output capacitor. This explains why the output voltage rises in steps until it reaches the predefined level, which was in this case set to 3.6 V.

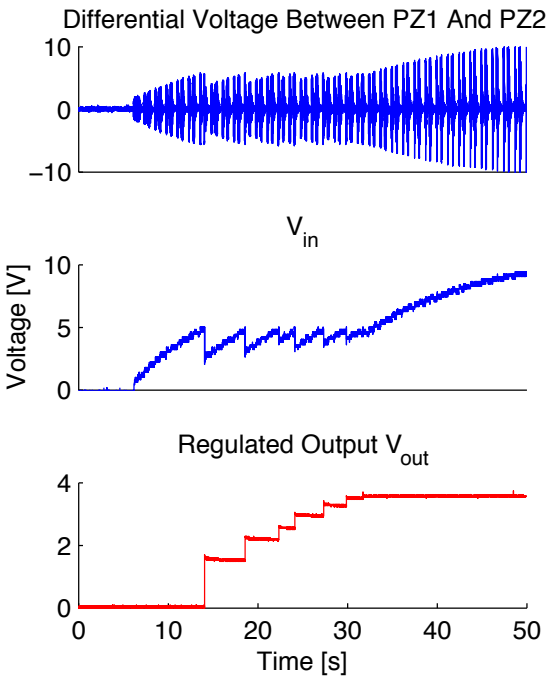

Figure 3.16: Voltage regulator start-up with no load

The power output after voltage regulation was determined with a variable resistor initially set to 1050 kΩ. After the target level was reached, this resistance was decreased, thus increasing the load current, until the voltage at the output terminals collapsed. The power can then be calculated as the chosen output voltage squared divided by the resistance. The results of this measurement can be seen in figure 3.17 where they are compared to the power output into an impedance matched resistive load of the same beam. The efficiency of the chip is presented in the same graph and is generally below 40%.

For excitation frequencies of 0.33 Hz and 0.66 Hz the start-up of the regulated output with attached load is shown in figure 3.18. The discharging of the output capacitor between voltage rises can be observed. Furthermore, at 0.33 Hz, the demand by the load is too high and the target level of 3.6 V is never reached; an equilibrium at a lower level is attained instead with a drop after each transfer of charge coming from the input capacitor. To conclude, it is important to take the losses of power processing into account

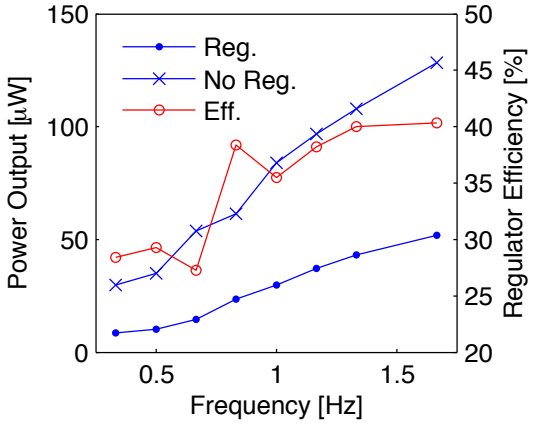

Figure 3.17: Efficiency and power output of the voltage regulator

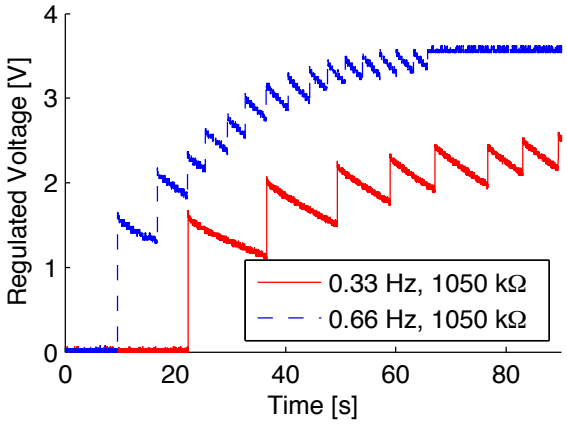

Figure 3.18: Voltage regulator start-up and equilibrium under load

during the layout of a harvester, and the circuitry can make a substantial difference to the usable power level.

3.5 Conclusions and Discussion

This chapter introduces an energy harvester with piezoelectric transducers based on the frequency up-conversion principle. The method is explained in detail with references to other implementations. The measurement set-up showed that the expected behaviour, namely the linear relationship between frequency and power output and the large bandwidth of operation, can

indeed be achieved. These capabilities are particularly well suited for body sensor applications due to the low, random excitation frequencies and the large amplitudes that dominate these conditions.

Four different configurations with regards to external acceleration and proof mass were compared and discussed. The importance of carefully matching the design to the targeted application in terms of transducer and proof mass selection was demonstrated. This is however, at the same time, a significant advantage of the presented device. Once the predominant excitation is known, the adjustments can be made during the layout process and there is no need for tuning the frequency, as would be the case for a resonant device. The achieved maximum conversion effectiveness of 8% is already quite promising, but given that the device is not fully optimised yet and in a prototype stage, further improvements are expected. The ideal relationship between initial gap and attraction force of the permanent magnets still needs further investigation. Other areas for potential performance increases are the shape of the beams as presented by Goldschmidtboeing and Woias [198] or Matova et al. [199] and the number of piezoelectric layers, as discussed by Zhu et al. [200, 201] or Xu et al. [202].

With regards to miniaturisation, a power density of 3.8 to 13 $\mu W/cm^3$ was achieved with the lighter proof mass m_2 at high acceleration a_1. This is based on an overall functional volume of 125 cm^3, keeping in mind that the prototype does not make ideal use of the available space. The free length of the beams, for example, is 60 mm whereas the proof mass length is only 45 mm. Nevertheless, downscaling to an overall volume of about 1 cm^3 should be achievable with standard components, based on the availability of ready made piezoelectric beams with dimensions of $10 \times 10 \times 1$ mm^3, as discussed with a manufacturer. Using MEMS fabrication techniques, even smaller device sizes seem possible. However, as will be seen in chapter 4, a further constraint on device size is the increase in stiffness of the piezoelectric elements as the device becomes smaller. This might prevent the beam from experiencing a sufficient initial deflection and there will be only a gradual release rather then a free oscillation as a consequence. It is also important to keep the physical limitations of achievable power density in mind. Assuming an excitation of 1 Hz and 0.5 g and assuming a steel proof mass occupying exactly half of the device volume, a maximal power density of 150 $\mu W/cm^3$ can be reached in theory, based on equation (3.1). The intended purpose

plays a key role. For example, in order to power the implantable blood pressure monitor presented in [21] around 200 to 300 μW are required. This is only possible with either a larger harvester or by significantly duty cycling the operation.

The use of an external steel proof mass was successfully implemented in this prototype. This has the advantage of a higher material density compared to the silicon proof masses common in MEMS devices and is favourable for an increased power density in accordance with equation (2.2). This approach was already taken in the electrostatic device presented in [102]. The problem in this earlier design was the difficulty to achieve sufficient electrical damping through electrostatic forces. The device suffered from low capacitance values and the transducer forces could not match the high inertial forces of the heavy proof mass. Using piezoelectric bending beams and distributed transduction alleviates this problem.

Furthermore, one of the first commercially available voltage regulators specifically designed for energy harvesting purposes was evaluated. A maximum efficiency of only 40% showed that the losses in power processing can not be neglected and that there is significant scope for further improvement in this area. Some steps in this direction have been made by Toh et al. [93], where maximum power point tracking for a rotating harvester is investigated. Approaches to increase the power output from piezoelectric transduction have been presented by Dicken et al. [203, 204, 205], based on pre-biasing of the piezoelectric beams and by Xu and Ortmanns [206]. The main scope of strategies aiming to maximise the extracted energy is to increase the electric damping of the transducers as discussed by Prabha et al. for the three main types of transducers [98]. A further consideration is the use of multiple piezoelectric beams in this prototype, which might require more complex circuitry. This is a topic that has been discussed by Romani et al. [207] and Shi et al. [208].

Ultimately, while this prototype is promising and could be very useful for certain low frequency applications, e.g. structural monitoring for bridges, there is one major drawback that complicates the use for human motion. The design with a freely rolling cylinder relies entirely on gravity and tilt angles relative to it. This works well as long as the orientation of the device is always the same relative to the ground. If the orientation changes for example such that the direction of cylinder travel is parallel to the direction

of gravity, the cylinder will roll to one end stop and be stuck there. This is impractical for human motion because the orientation is constantly changing based on the motion. For instance, if such a device were mounted on the wrist, it could well be that it can not generate electricity most of the time. This is the main reason for investigating rotational systems as introduced in section 2.7, and chapter 4 will present a piezoelectric frequency up-converting harvester with rotating proof mass.

4 Frequency Up-Converting Piezoelectric Harvester with Rotating Proof Mass

As was concluded in chapter 3, a rolling rod approach is impractical for human motion harvesting and the potential benefits of rotational devices have been discussed in section 2.7. The purpose of this chapter is to take the successful implementation of piezoelectric beam plucking from the earlier linear prototype into a rotational set-up. The development of this device took place in three iterations, starting with a proof of concept, followed by a first miniaturised prototype and then a finalised device. All of these will be explained with intermediate conclusions that led to improvements. The final device is subjected to a series of experiments, both in a real world environment and in a laboratory set-up and the results are included in this chapter. The majority of the presented findings have been published in peer reviewed conference proceedings [209, 210, 211] and the results from section 4.3 have been published in the Journal of Sensors and Actuators A – Physical [212].

4.1 Initial Design of a Rotational Harvester

4.1.1 Operation Principle and Concept

The first design of the rotational harvester will be presented in this section and figure 4.1 shows the main parts. The transduction still relies on plucking of piezoelectric beams for frequency up-conversion. Another novelty is that, with the new arrangement, the magnetic coupling is completely contactless. The front and section views in figure 4.2 show the arrangement in more detail. A permanent magnet is attached to the tip of the piezoelectric beam. A second magnet is mounted inside the rotor. When the rotor swings

under external excitation the two magnets will attract each other at each pass. The tip of the beam is dragged along until the bending force exceeds the magnetic attraction force at which point it is released. Another point is that the proof mass has no inherent displacement limit since it can rotate freely in any direction around its axis.

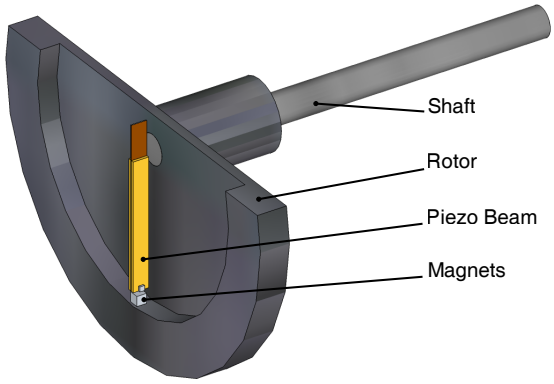

Figure 4.1: Piezoelectric rotational harvester

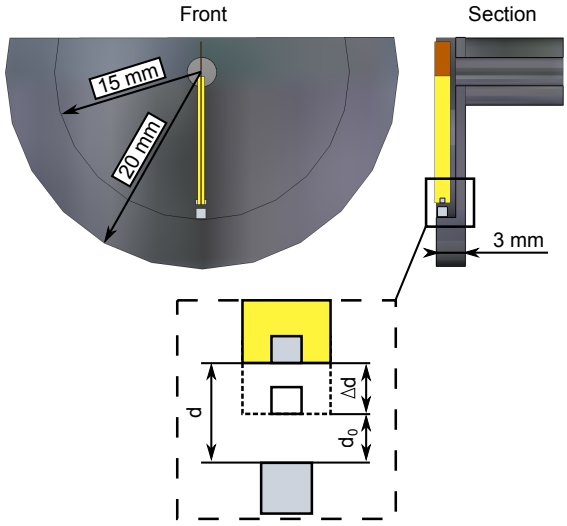

Figure 4.2: Front and section view of the rotational harvester showing the arrangement of the magnets

4.1.2 Experimental Set-Up

Figure 4.3 shows the experimental set-up built as a proof of principle. The rotor is machined from mild steel and a 4 mm shaft is press fitted into a center hole. This assembly is held by two ball bearings. The total mass, measured including the shaft, is 15 g and the effective rotor mass was calculated to be 9 g. The swept volume of the rotor is 3.7 cm^3.

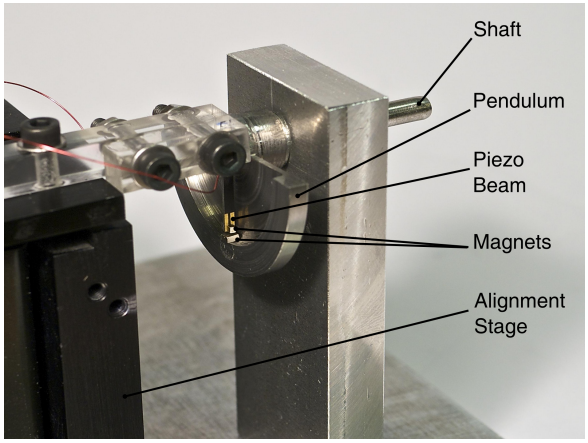

Figure 4.3: Experimental set-up of the rotational harvester

A 3-axis alignment stage was used to mount a clamp that holds the piezoelectric beam. The advantage is that the position, especially the vertical gap between the two magnets, can be adjusted very precisely. This was used to evaluate the influence of the gap on the power output. It is worth noting that it was difficult to measure the absolute value of the initial gap d_0, which was adjusted such that the two magnets barely did not touch each other. For this reason, the measurements were performed in 0.05 mm increments relative to this initial gap. The magnification in figure 4.2 illustrates the relative gap Δd. It is estimated that d_0 is indeed quite small, around 0.1 mm, but it is important to keep in mind that the total gap is $d = d_0 + \Delta d$, especially when graphs are shown in relation to Δd, which can be zero.

The piezoelectric beam was provided by Johnson Matthey Catalysts (Germany) GmbH. It uses their H42 ceramic mixture and is configured as a series bimorph. The copper center shim is 0.1 mm thick and extends by 3.5 mm at the end for convenient clamping. The dimensions of the active area are

$13 \times 1.6 \times 0.7$ mm. The capacitance $C_{\tilde{p}}^{eq,s}$ of the beam was measured as 520 pF and the natural (angular) resonance frequency of the first mode ω_1 is 380 Hz. To match the output impedance magnitude of the beam, i.e. $1/\omega_1 C_{\tilde{p}}^{eq,s}$, a load resistance of 800 kΩ was necessary. Similar to the procedure in chapter 3, the power output was calculated as the RMS voltage squared divided by the load resistance.

The magnet at the tip of the beam is $1 \times 1 \times 1$ mm in dimension and the one mounted inside the rotor is $2 \times 2 \times 1$ mm. Both are NdFeB magnets of N50 strength and are oriented such that they attract each other.

The same rocking table as in chapter 3 was used (see figure 4.4 for the mechanical schematics) with a frequency range between 0.33 Hz and 2 Hz (corresponds to settings between 20 rpm and 120 rpm). The maximal platform tilt angle was set to $\Omega_0 = 16.1°$, thus providing an oscillation:

$$\Omega(t) = \Omega_0 \sin(\omega t) \tag{4.1}$$

where ω describes the rotation of the driving wheel shaking the platform through a connection rod (figure 4.4).

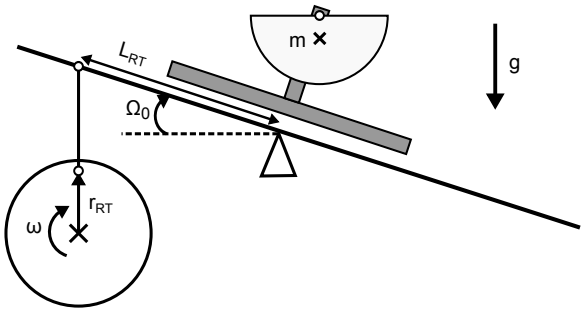

Figure 4.4: Mechanical schematics of the rocking table

4.1.3 Measurement Results

Figure 4.5 shows the voltage measured across the piezoelectric beam without load during a single excitation. The rocking table was set to 2 Hz and the gap between the magnets was at its minimal value d_0. At first, the tip of the beam "snaps" towards the approaching magnet on the rotor. After that, the two parts travel synchronously until the beam bending force exceeds the attraction force and the beam is released to vibrate at its natural frequency.

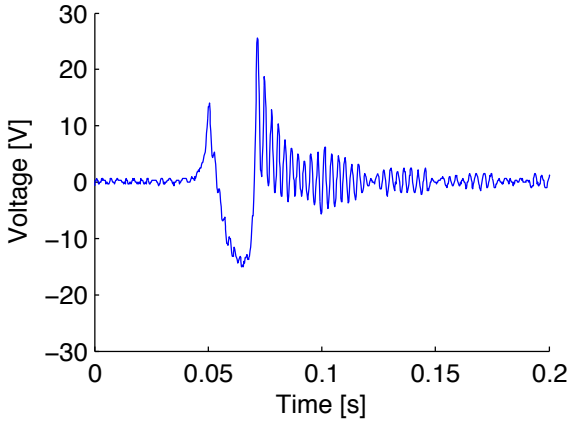

Figure 4.5: Single actuation of the beam at 2 Hz and minimal gap d_0

In figure 4.6, continuous operation over 2 s is represented for the same settings. The oscillation has more or less completely died off between actuations. It can also be seen that the beam is plucked twice during a cycle, once in each direction, which explains the alternating positive and negative peak voltages.

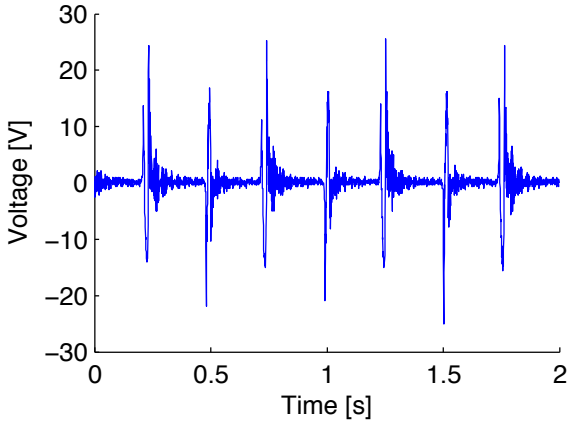

Figure 4.6: Continuous actuation of the beam at 2 Hz and minimal gap d_0

The magnetic coupling from the rotor to the beam is largely influenced by the air gap between the two. This is demonstrated in figure 4.7 where the relative gap is increased to $\Delta d = 0.5$ mm. In order to facilitate comparison all other settings as well as the scaling of the axes were kept the same as in figure 4.6. Although the beam still experiences the same pattern

of actuations, the peak voltage drops significantly and there is almost no oscillation present due to a very gradual release of the beam.

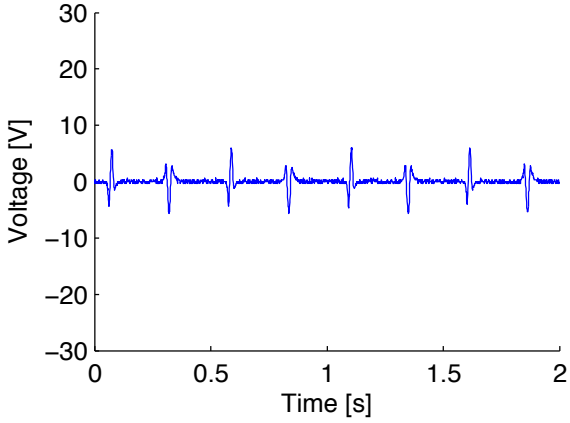

Figure 4.7: Continuous actuation at a relative gap $\Delta d = 0.5$ mm and 2 Hz

To further illustrate this, figure 4.8 shows the variation of power output with relative gap size Δd. At the initial gap a power output of 2.6 µW was achieved at an RMS voltage of 1.45 V. With an increase in gap size this value drops very rapidly. Due to the attraction force between the magnets, the rotor tends to get stuck in the equilibrium position, held by the magnet on the beam. This behaviour occurs when the external excitation is not sufficient to overcome the attraction and sets a lower boundary for the operation frequency of the device. The way to adjust this limit is by changing the coupling between the magnets. This can be done by two different approaches, either by increasing the gap or by choosing weaker, smaller magnets. The latter option has to be investigated in the future, but figure 4.8 shows that increasing the gap will not lead to optimal results. This was already experienced in the case of figure 4.7 where a more gradual release of the beam prevents vibration.

At the minimal gap, an excitation of 2 Hz constitutes exactly this lower boundary, which in turn gives the best effectiveness of conversion. At anything below this frequency the rotor gets stuck and no power is generated. Due to the rocking table being limited to a maximum frequency of 2 Hz it was necessary to perform the measurements for figure 4.9 at a relative gap of $\Delta d = 0.5$ mm. This measurement is purely meant to illustrate the linear relationship between power output and frequency, inherent to fre-

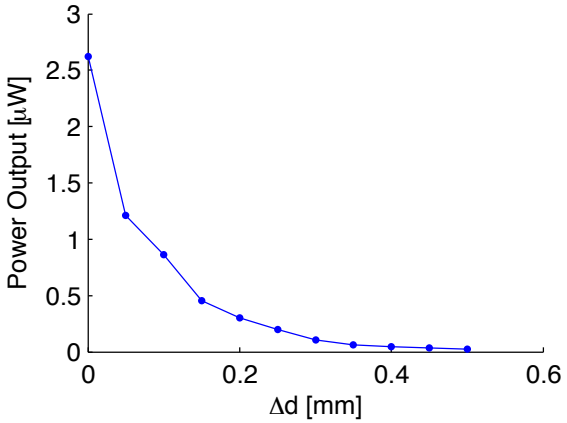

Figure 4.8: Power output in relation to the relative gap Δd, measured at 2 Hz

quency up-converting devices and the absolute values of achieved power are by no means representative of the actual capabilities of the device. The graph shows the power output compared to the frequency. The lower limit comes to lie at 1.33 Hz from where the increase in power output is fairly linear all the way up to 2 Hz with one exception at around 1.66 Hz. Possible explanations for this will be discussed together with figure 4.11.

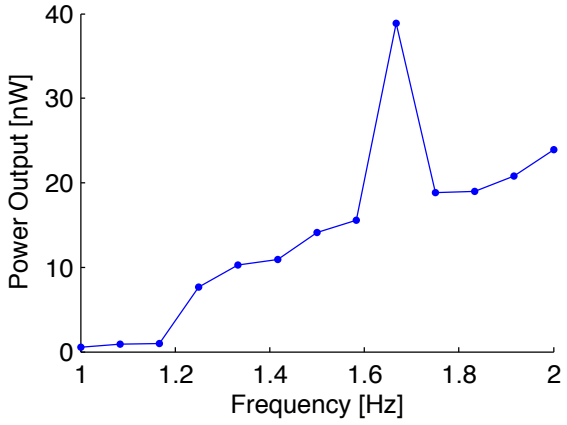

Figure 4.9: Power output in relation to excitation frequency for a relative gap $\Delta d = 0.5$ mm

Figure 4.10 shows a similar measurement performed at $\Delta d = 0.25$ mm. The number of measurement points is smaller because the lower limit is as

high as 1.6 Hz. However, an increase of power output with frequency is still present. Furthermore, around 1.75 Hz a similar behaviour to figure 4.9 can be observed, although not quite as pronounced. Overall, the smaller gap leads to better results as was to be expected according to the graph in figure 4.8.

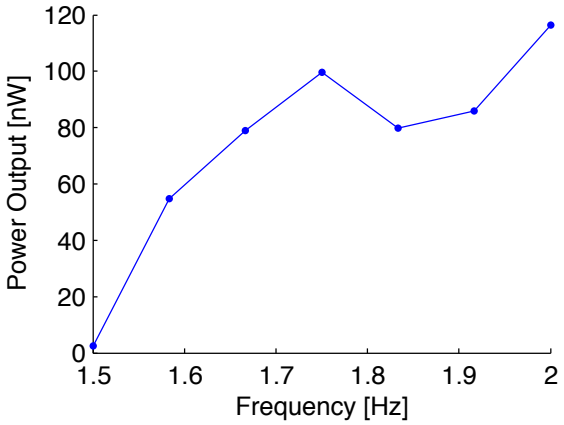

Figure 4.10: Power output in relation to excitation frequency for a relative gap $\Delta d = 0.25$ mm

Figure 4.11 depicts the measured voltage output with attached load at 1.66 Hz corresponding to the previously discussed measurement at $\Delta d = 0.5$ mm. At 0.3 s, it seems as if the beam is not fully released at first, with the rotor hovering around the equilibrium point but still acting on the beam. At 0.5 s the expected peak similar to figure 4.5 reappears. The pendulum resonant frequency without including damping effects was calculated to be 4.95 Hz. A single release of the rotor with the base of the device set up on a level surface and measuring the time between beam actuations shows a pendulum frequency of 2.8 Hz. This lower value is, at least in part, due to the interaction with the beam slowing the rotor down when it passes at the bottom. It is believed that the ultimate reason for the sudden increase in power output achieved at 1.66 Hz is caused by the non linear nature of pendulum motion under the influence of gravity combined with the moment exerted by the magnetic coupling. The last assumption is supported by the slightly higher frequency at which the phenomenon occurred under smaller relative gap size in figure 4.10.

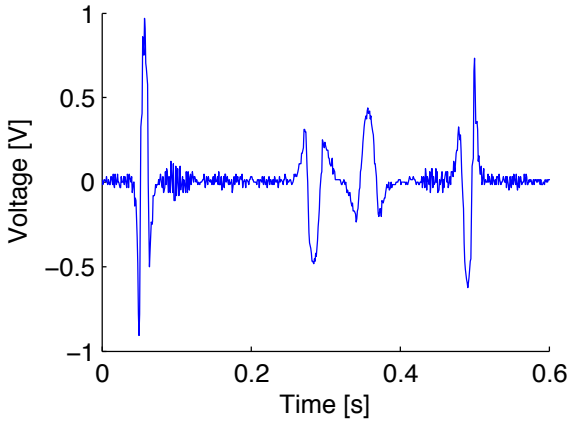

Figure 4.11: Actuation at 1.66 Hz and relative gap $\Delta d = 0.5$ mm with attached load

4.1.4 Conclusions

This section presents an inertial rotary energy harvester with a transduction mechanism based on the piezoelectric impulse-excitation principle. The advantages and limitations of this design were discussed. A proof of concept was shown and the first results are promising.

The device can operate over a large range of frequencies which is suitable for the random excitations imposed by the human body. Furthermore, the magnetic coupling between the rotor and the beam allows for a completely contact-less actuation. This will be beneficial for the longevity and reliability of the design.

The maximal power output reached was 2.6 µW. This result is lower than the estimated output from the Seiko Kinetic discussed in section 2.1 but would still suffice to power the movement. Furthermore, it can partly be explained by the small excitation amplitude ($\Omega_0 = 16.1°$) of the rocking table. At this limited angle, the achieved acceleration corresponds to 2.7 m/s^2 (about 0.28 g), whereas values up to 0.5 g can be expected from the wrist [91]. When compared to the theoretical maximum as calculated by (2.5), the effectiveness of energy conversion reaches 5.8 % . Under the assumption for (2.5) that the excitation is maximal throughout the travel range, which is not true under sinusoidal input, higher effectiveness values seem feasible once the design has been fully optimised.

First steps towards the determination of the ideal gap size and magnetic coupling were also made. The experimental data already show that increasing the gap size might not be a viable option for best results. Chapter 5 goes into the details of modelling and optimising the magnetic interaction and some of the findings in that chapter have been implemented in the following designs of the harvester.

4.2 Miniaturised Prototype Rotational Harvester

4.2.1 Updated Device

The initial results from the proof of concept were promising and thus the next step was to make the design smaller and contained in a standalone casing without the alignment stage for adjusting the gap between magnets. Figure 4.12 shows a drawing of the miniaturised prototype and figure 4.13 gives the corresponding section view. The centre piece is a piezoelectric transducer in the form of a parallel connected bimorph beam provided by Johnson Matthey. The length and width are 10 mm and 1 mm respectively with a 240 µm carbon fibre center shim. Each piezoelectric layer has a thickness of 130 µm, giving an overall thickness of 0.5 mm. The beam is bonded into a pocket milled into a perspex lid with epoxy glue. The reason for using perspex is purely to allow observation of the internal motion at the cost of adding an additional 2 mm of thickness to the overall dimensions. Due to the bonding, the free length of the beam ends up at 7.5 mm, resulting in an open circuit natural frequency of 2800 Hz, a capacitance of 3.85 nF and an impedance of 15 kΩ. The magnets are $1 \times 1 \times 1$ mm N35 NdFeB permanent magnets and have been arranged such that they repel each other; it will be shown in chapter 5 that this is advantageous. The flanged bearings for the 1 mm diameter shaft have an outer diameter of 3 mm. The rotor is a half disc made from steel to increase the proof mass density and weighs 2 g. The outer casing is machined from aluminium.

The outer diameter and thickness of the assembly are 29.4 mm and 8 mm respectively, giving a total device volume of 5.4 cm^3 and a weight of 8.2 g. However, the swept volume of the rotor with magnet is the actual functional volume and is only 1.3 cm^3. The outer dimensions are similar to a normal wristwatch and could be greatly reduced by machining the casing and lid

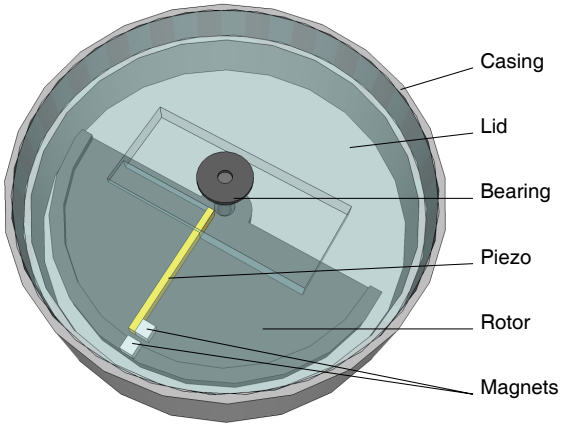

Figure 4.12: Drawing of the miniaturised rotational prototype

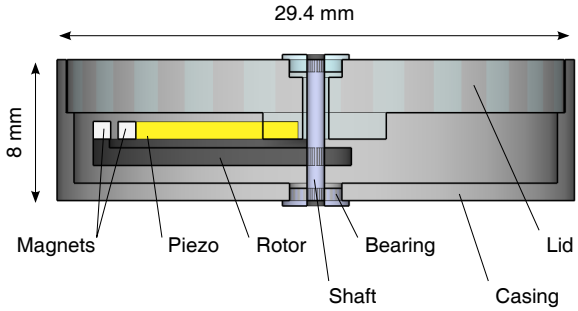

Figure 4.13: Section view of the miniaturised rotational prototype

from steel and making it thinner, and by reducing the clearances. Integration of the harvester into an existing wristwatch would also be imaginable.

Figure 4.14 shows a photograph of the actual device parts and demonstrates the simplicity of the design compared to other devices such as the Seiko Kinetic wristwatch that uses a gear train to operate an electromagnetic transducer [7]. Figure 4.15 depicts the final assembly with the three connection wires – one to the center layer of the piezoelectric beam and the two others to make a parallel connection via the outer contacts. Furthermore, two additional holes were drilled into the lid; the top one allows disassembly of the device with a steel hook and the bottom one gives a view of the air gap between the two magnets.

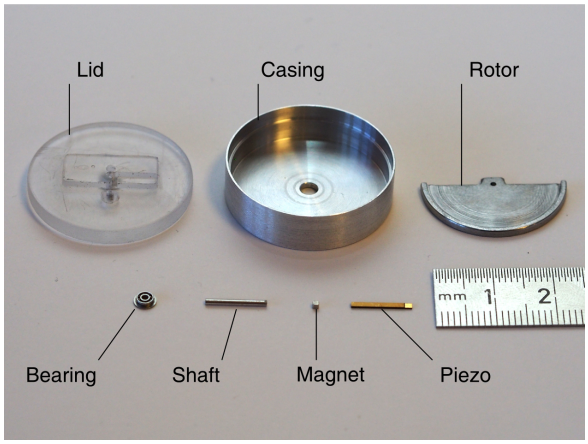

Figure 4.14: Prototype parts

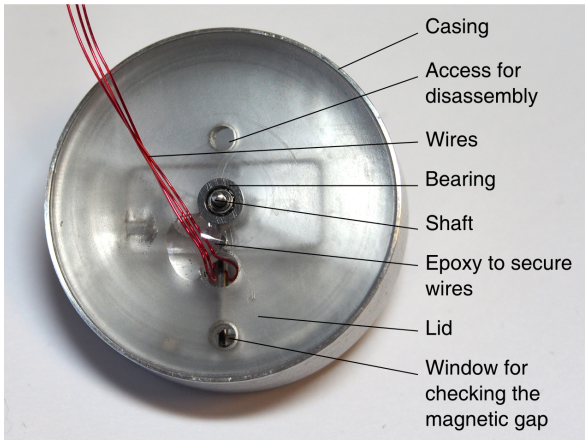

Figure 4.15: Prototype assembly

4.2.2 Measurement Results

Figure 4.16 gives the voltage output measured on an oscilloscope when plucking the piezoelectric beam manually with a fine needle. This measurement was used to determine the oscillation frequency of the beam (2800 Hz) and a Q-factor, without any load attached, of approximately 30. The graph also shows a significant improvement of the beam attachment to the base. In the proof of concept of section 4.1, the beam was clamped via its centre layer only, which caused a weakness at the base that led to free oscillations with different frequency components and ultimately even to chipping of the piezoelectric material in the contact area. In contrast, gluing the beam into

the lid with epoxy resin leads to a clean decaying oscillation.

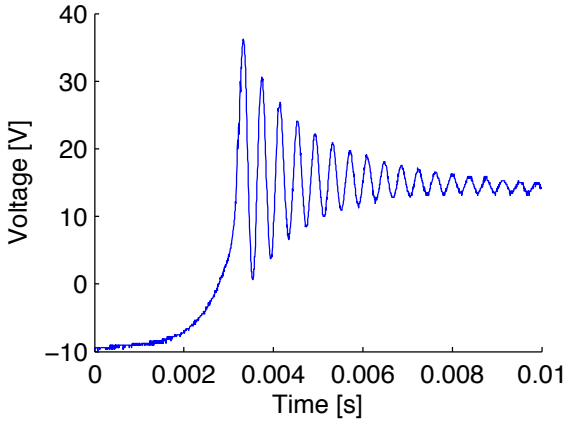

Figure 4.16: Experimental manual plucking of the beam with a fine needle

The disadvantage of using a shorter beam is the increased stiffness. This requires higher initial actuation forces, i.e. a harder plucking, to achieve free oscillation after release. The consequences can be seen in figure 4.17, which demonstrates operation of the device. In this case the harvester was manually shaken while connected to the oscilloscope. Each peak in the voltage diagram marks one actuation of the beam. The rotor fails to actuate the beam, that is so stiff that the external excitation can not provide a sufficient initial deflection. Under these conditions the power output into an impedance-matched resistive load was in the order of a few nanowatts.

A similar experiment was conducted on the previously introduced rocking table with a controlled external excitation of 2 Hz and 2.7 m/s^2. The result can be seen in figure 4.18. Similar to the earlier graph, the voltage output exhibits peaks when the piezoelectric beam is actuated. However, at approximately 0.2 s and 0.8 s, lower and wider peaks occur. In those instances, the rotor does not manage to push past the magnetic repulsion from the beam. Instead of passing the beam, the rotor only bends it and is reversed back into the direction it came from. This behaviour demonstrates the lower excitation limit for this device and indicates a good match between the magnetic force and the actuation force the eccentric rotor can provide at this low excitation.

It was clear from these experiments that the stiffness of the beam needed to be lowered to allow free oscillation as intended. After discussion with

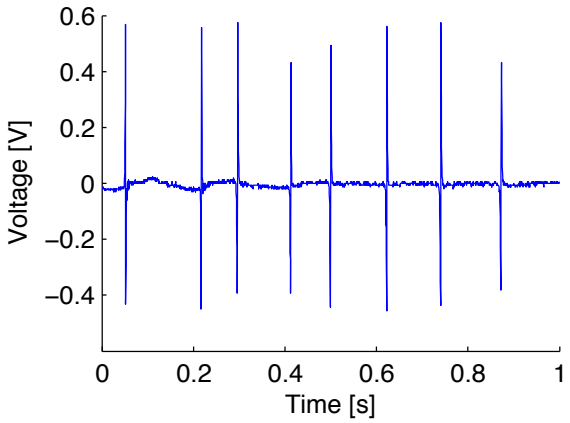

Figure 4.17: Experimental device operation when shaken by hand, without load

Johnson Matthey, the supplier of the piezoelectric material, one side of the bimorph was sanded down to the carbon fibre centre layer. As the thickness of a beam affects the stiffness by a cubic factor, it was thus possible to dramatically reduce the resonance frequency of the beam down to 1600 Hz. The beam was effectively transformed into an asymmetric monomorph with just one carbon fibre base layer and one piezoceramic layer on top. The capacitance drops to half the initial value (both layers were previously connected in parallel) and the resulting impedance matched resistive load is now 50 kΩ. Similarly to figure 4.16, figure 4.19 shows a single actuation of the beam without load for comparison. The differences in peak voltage are partly due to the lack of one layer and partly due to differences in initial deflection when manually plucking the beam.

Additionally, both magnets were replaced by stronger N45 versions of the same dimensions. As a result, the excitation provided by the rocking table was not sufficient for the device to operate, as was to be expected from the earlier findings. For this reason, the experiment in figure 4.20, showing the voltage measured under operation without any load, was conducted by vigorously shaking the device by hand as this provides a strong enough excitation. Counting the number of beam actuations yields an average frequency of $4 - 5$ Hz with an approximate motion amplitude around $30 - 100$ mm. The RMS voltage lies around $500 - 900$ mV and the peak voltages are much higher in comparison to figure 4.17.

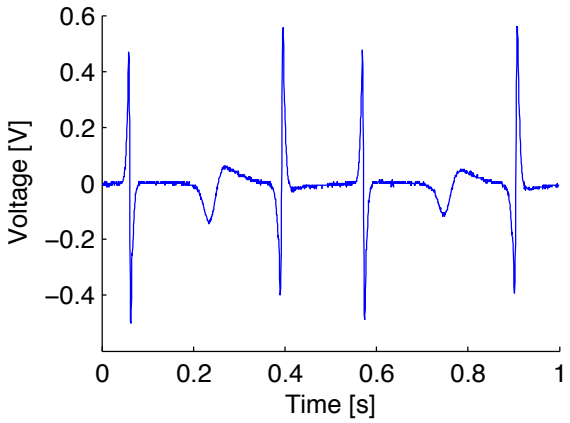

Figure 4.18: Experimental device operation at 2 Hz and 2.7 m/s^2 on a rocking table, without load

Figures 4.21 and 4.22 show single beam actuations in operation for the open circuit case and the case with impedance matched resistive load respectively. These figures demonstrate that the modifications, i.e. thinning one side of the beam and introducing stronger coupling through better magnets, were successful and the device operates as intended with magnetic plucking of the piezoelectric beam and following free oscillation. Furthermore, power output into an impedance matched load ranged between 50 nW and 2 μW at RMS voltages in the region of $50 - 300$ mV. The distortions in the voltage curves could be due to the sanding process that cannot guarantee a completely even thickness along the beam. Also, the beam was initially designed as a bimorph without the effects of the asymmetry of a monomorph in mind. Nevertheless, reducing the thickness, and thus the stiffness, of the beam vastly improved the prototype.

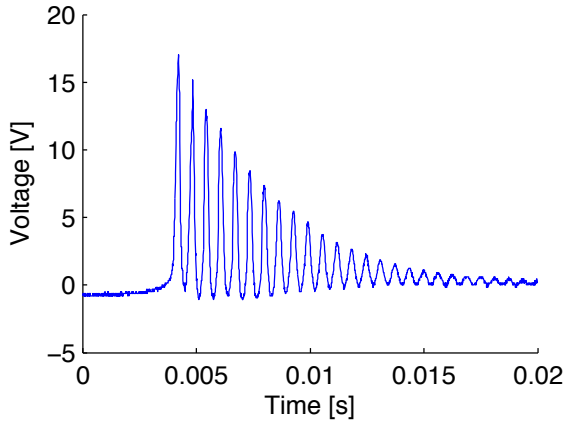

Figure 4.19: Experimental manual plucking of the beam with a fine needle for the monomorph beam

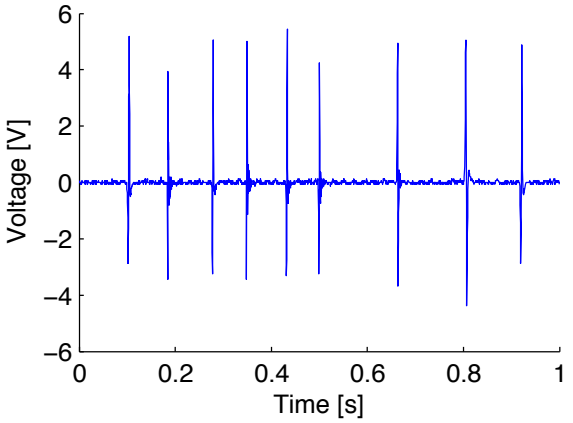

Figure 4.20: Experimental device operation with stronger magnets and monomorph piezoelectric beam, continuously shaken by hand and without load

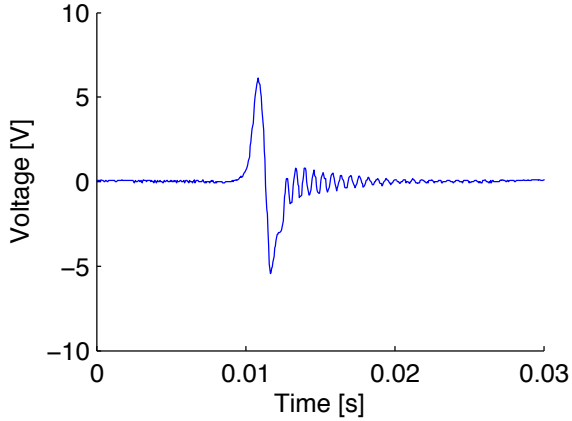

Figure 4.21: Experimental single actuation with stronger magnets and monomorph piezo beam, shaken by hand and without load

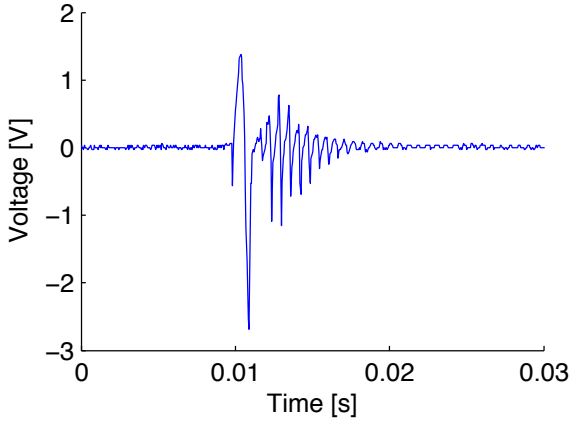

Figure 4.22: Experimental single actuation with stronger magnets and monomorph piezo beam, shaken by hand and with impedance-matched resistive load

4.2.3 Conclusions

The continuation of the previously introduced proof of concept is shown in this section. The design has moved on from a large set-up to a small, wearable device the size of a wristwatch. The mechanical assembly of a harvester with a functional volume of 1.3 cm^3 was successful and a good match between the proof mass and the magnetic forces was experimentally demonstrated. Previous shortcomings in the attachment of the beam were vastly improved facilitating a clean, sinusoidal ring-down of the beam oscillation.

On the other hand, the experiments proved that there are limits to the frequency up-conversion harvesting strategy. In this case the piezoelectric beam was initially too stiff to allow good plucking and did not show any oscillation after actuation, which resulted in a power output well below the capabilities of the technique. Two modifications to the prototype were undertaken. Stronger magnets were introduced to enhance the actuation of the beam at the expense of shifting the operation range to higher excitations. Furthermore, one side of the piezoelectric bimorph was sanded down, transforming the beam into a monomorph with lower stiffness. This strategy led to major improvements since it made oscillation after initial actuation possible. Ultimately, the use of a heavier proof mass to match the stronger magnetic forces and different ways to lower the stiffness of the beam, e.g. accommodating a longer beam, will be incorporated in the finalised device in the following section 4.3.

4.3 Finalised Rotational Harvester

4.3.1 Device Description

The final iteration of the rotational harvester incorporates all of the findings gathered from the previous experiments and the calculations that will be discussed in chapter 5 in terms of magnetic coupling and beam stiffness. A rendering is provided in figure 4.23 in an isometric and a section view. The transducer is a bimorph piezoelectric beam custom made by Johnson Matthey in their M1100 ceramic. The arrangement is now made such that the beam is fixed in the lid on one side of the device and the bearings holding the rotor are both on the casing side of the prototype. This way, the beam can occupy the full diameter rather than only the radius, and

with the increased length, the stiffness drops significantly. Furthermore, the layers were chosen as thin as possible – 130 µm for each of the piezo layers and 110 µm for the carbon fibre center shim. The layers are electrically connected in series. The free length is now 19.5 mm and the width is 1 mm. Again, the beam is glued inside a slot milled into the perspex lid with epoxy resin as this worked well in the previous iteration. In addition, the slot is now designed such that it provides end stops for accurate positioning of the beam. The piezoelectric beam in this configuration has a resonance frequency of approximately 400 Hz, a capacitance of 3.1 nF and consequently a load of 150 kΩ was chosen as an impedance match.

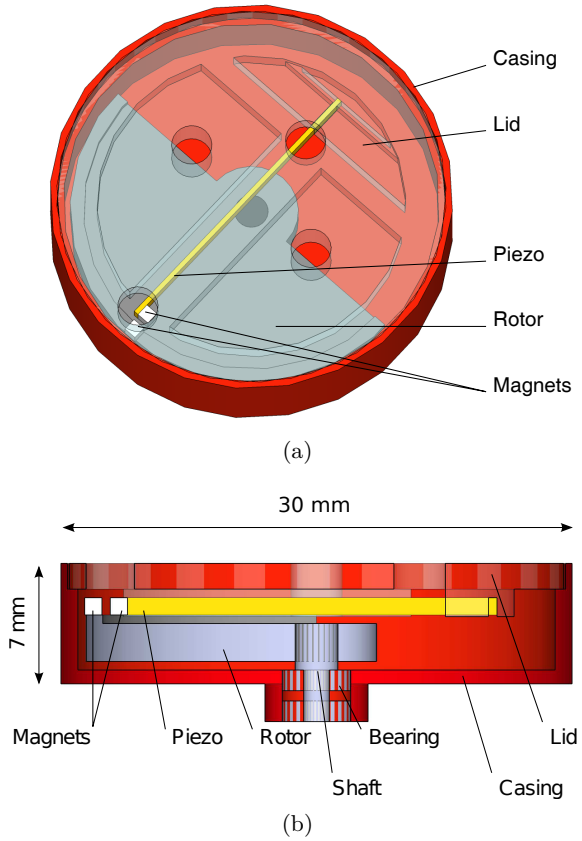

Figure 4.23: Rendering of the rotational harvester in isometric view (a) and corresponding section view (b)

The permanent magnets are the same $1 \times 1 \times 1$ mm N45 NdFeB permanent magnets as used previously, again in a repelling arrangement. The

outer casing was machined from aluminium (diameter 30 mm, thickness 7 mm) and anodised in red. The bearings are a 681X-2Z-MB type of $4 \times 2 \times 1.5$ mm to take a 1.5 mm shaft. The rotor itself is machined from steel with an outer diameter of 27 mm and a thickness of 2.2 mm to give a weight of 4.8 g, matching the rotor inside a Seiko 5M62A/5M63A caliber [7] in dimensions and weight. This allows a comparison between the two mechanisms purely based on the performance of the transduction system, as the harvested energy is ultimately limited by the kinetic energy stored in the proof mass.

The total device volume is 5 cm^3, weighing 10.5 g. The swept volume of the rotor with magnet, i.e. the functional part, is only 1.85 cm^3; this is the volume that matters most when thinking about integrating the device into an entire system.

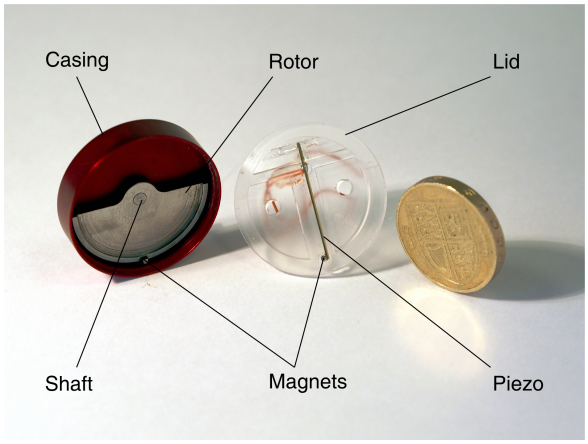

Figure 4.24: Photograph of the energy harvester with size comparison to a British one pound coin

Finally, a photo of the actual prototype is given in figure 4.24. The casing assembly with the rotor is on the left and the lid assembly with the piezoelectric beam is in the middle. The simplicity and limited number of parts for this design is clearly illustrated.

4.3.2 Real World Testing

The real world test was performed during a half marathon running race. This presents a challenging environment and gives the opportunity to investigate device performance over a longer period of time.

Portable Measurement System

Testing a device like this in the field requires a small enough capturing system to record the data and still be worn comfortably. Two additional requirements were incorporated that made the set-up more complex. It was decided that the entire voltage waveform of the piezoelectric beam should be recorded, not only the power output. At an oscillation frequency of about 400 Hz a fast sampling rate is needed. Furthermore, the accelerations were recorded with a three axis accelerometer. A Sparkfun Logomatic V2 data logger, writing onto micro SD card offers a convenient solution as it can reliably log data from its internal 10 bit ADC at 2000 Hz sampling rate if recording in binary mode. However, this rate can only be achieved on a single channel – for four channels, the rate drops to 500 Hz, which is not enough to capture the waveform. The solution was to use a programmable ArduLog board, a special version of an Arduino chipset with integrated micro SD card slot, as a second data logger to record the three outputs of an ADXL 335 accelerometer at a lower sampling rate and to write the output into files containing five minutes of data each.

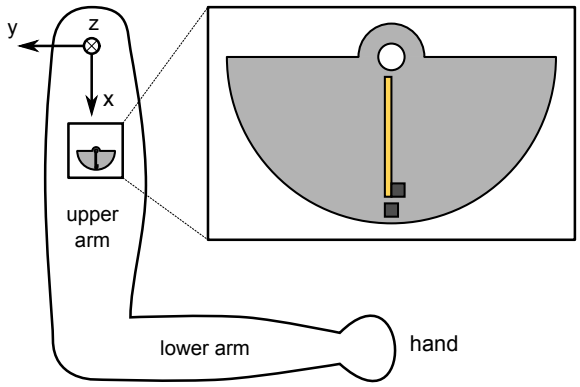

Figure 4.25: Orientation of the harvester and accelerometer coordinate system when mounted on the upper arm during the half marathon test

Furthermore, the program on the ArduLog board switches the Logomatic on and off as required to create matching data files. The system was packaged inside a standard cell phone arm strap and positioned on the upper right arm with orientations as shown in figure 4.25. In addition, since the

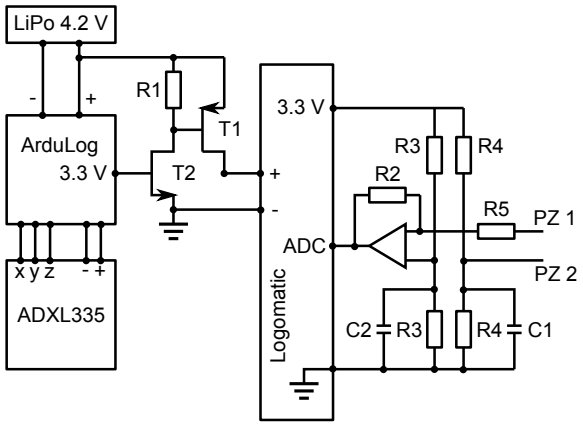

Figure 4.26: Electronic schematic of the data logging system

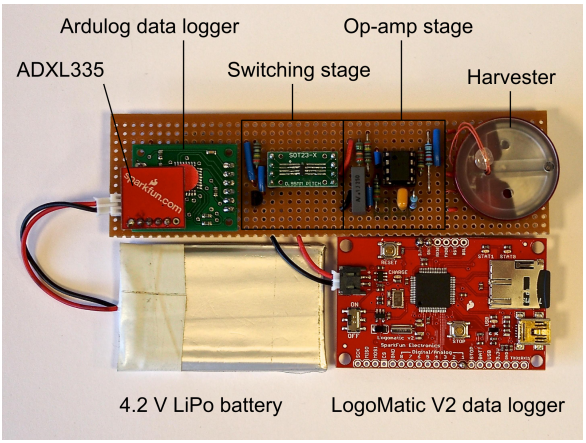

Figure 4.27: Photograph of the data logging system

ADC of the Logomatic V2 operates between $0 - 3.3$ V, an op-amp circuit was built to shift the AC signal from the piezoelectric beam and bring it into a recordable range. The entire circuit is shown in figure 4.26 and the values of the components are given in table 4.1. Finally, a photograph of the system before packaging can be seen in figure 4.27.

Measurement Results

Before the actual start of the race, a twenty minute test run was performed to verify proper operation of the system. The first five minute interval recorded during that test is shown in figure 4.28. This graph spans too much

Table 4.1: Components used in the portable measurement system depicted in figure 4.26

Component	**Description**
R1	1 MΩ
R2	30 kΩ
R3	1 MΩ
R4	10 kΩ
R5	150 kΩ
C1	1 µF
C2	100 nF
T1	P-channel MOSFET SI2305
T2	N-channel MOSFET BS170
Op-Amp	TLV2761

data to see the actual waveform, but there is another interesting detail. One can see that for most of the time the generated voltages reach up to 10 V where they are very slightly truncated due to the ADC saturating. However, there is a major gap after about 100 s and again a smaller gap a bit later on. These gaps do not represent a malfunction of the device, but merely stopping at red lights to cross streets. When standing still, a motion energy harvester can not harvest any energy from the body, which stresses the importance of intermediate energy storage as outlined in section 2.3.

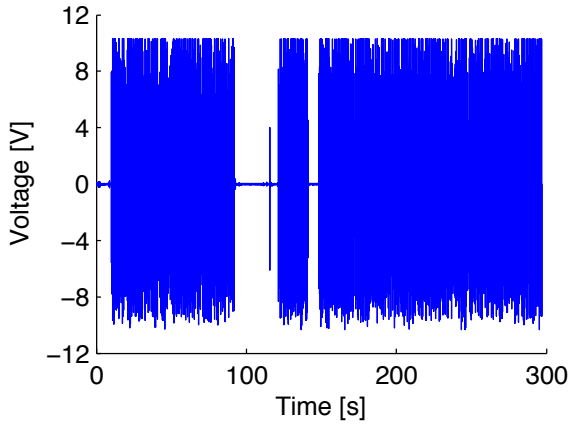

Figure 4.28: Sample of an entire five minute data set for the voltage output of the piezoelectric beam while running

A detailed view of the voltage output is given in figure 4.29 for one of the datasets. Three actuations and the following ring down of the free oscillation can clearly be seen, confirming that the plucking mechanism performs as intended. Furthermore, the FFT taken over the middle one of those three actuations is shown in figure 4.30.

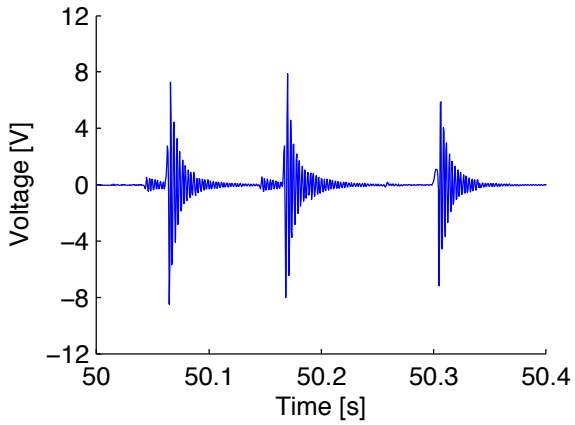

Figure 4.29: Detailed view of the the voltage output of the piezoelectric beam while running

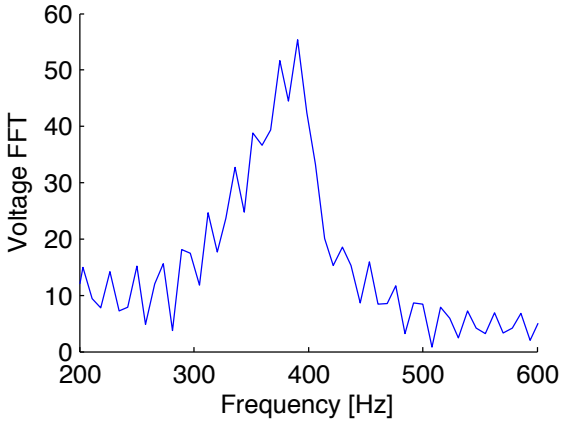

Figure 4.30: FFT taken over a single actuation corresponding to figure 4.29

Figure 4.31 shows the output from the accelerometer in each axis and, again, the corresponding FFT is shown in figure 4.32. First, the strong negative trend of the x-axis is hardly surprising, given that it is subject to 1 g gravitational acceleration. The lower excitation in the z-direction

is also understandable due to the orientation of this axis perpendicular to the running direction and the strong excitation in y comes from arm swing and running motion. A look at the FFT reveals that the majority of the excitation happens below 2.5 Hz. In comparison with the FFT from the voltage output in figure 4.30, this confirms that the low excitation frequency has indeed been up-converted through the magnetic plucking mechanism.

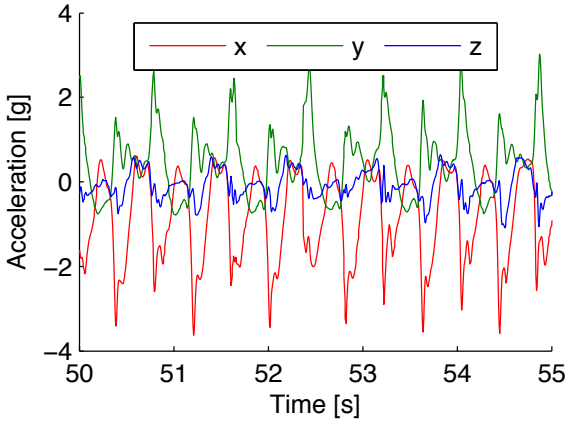

Figure 4.31: Sample output of the three axis accelerometer while running

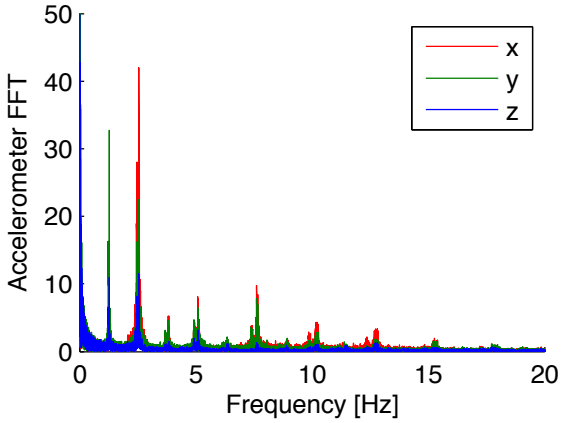

Figure 4.32: FFT of the accelerometer data shown in figure 4.31

Figure 4.33 reveals a strong degradation of the piezoelectric beam in the first thirty minutes from an initial 7 µW power output to a plateau at about 0.5 µW. This is a result of initially over-stressing the piezoelectric beam with the magnetic coupling being too strong. However, in the following

section, it will be shown that much improved results were achievable by simply increasing the gap between the permanent magnets and thus lowering the coupling force and consequently the initial deflection of the beams. This might seem contradictory to conclusions drawn in section 4.1 that increasing the magnetic gap is not a viable option as it decreases the power output. However, the case here is different in that the beam still exhibits a clean release and free oscillation after increasing the gap. This is possible due to the much lower stiffness of the beam.

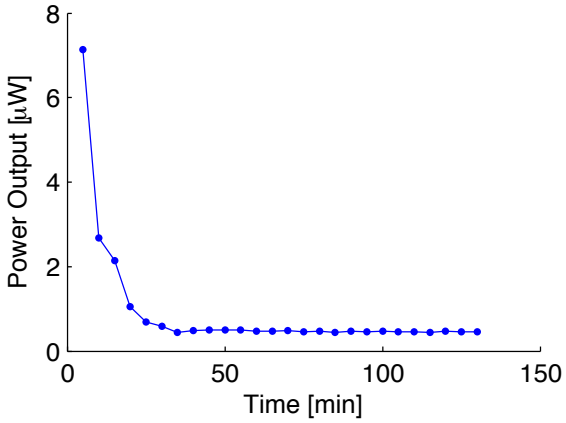

Figure 4.33: Degradation of power output over the pre-race test and actual race

4.3.3 Laboratory Measurements

Experimental set-up

Human motion is characterised by large displacement amplitudes and low frequencies. For the purpose of recreating these excitations reliably, a linear shaking system was designed and built. The core of the set-up is a Thomson Linear M55 ball guided belt drive system with 650 mm maximum usable displacement. The reason for choosing a belt drive rather than a lead screw unit is that the higher positioning accuracy of the latter is not strictly necessary for this application and the belt drive can achieve higher maximum accelerations of up to 40 m/s^2, which makes it more versatile. The motor is a Kollmorgen AKM33E-ANCNR-00 brushless servo drive with rotary encoder, rated up to a current of 2.58 A, torque of 2.79 Nm, power

of 1.19 kW at 5000 rpm and 640 Vdc. This motor is capable of providing enough torque to carry a 1 kg load on the slider at 2 Hz recurring motion with an acceleration of 20 m/s^2 over the entire travel range as per the basic parameters chosen for the layout. The matching drive controller is a Kollmorgen AKD-P00306 rated for a maximum drive current of 3 A and operated through 240 V mains power supply. The entire control system is given in the photograph of figure 4.34.

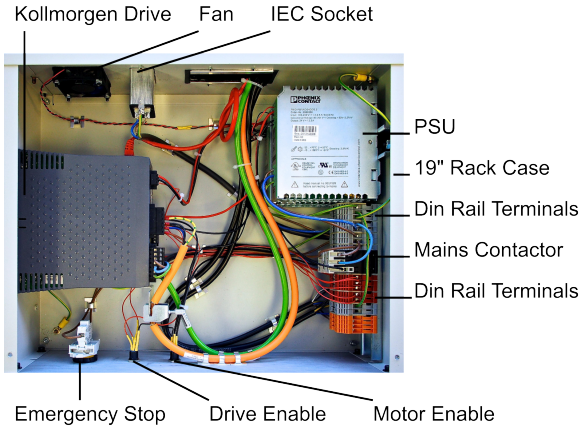

Figure 4.34: Photograph of the control system of the linear shaking set-up

The drive system is connected via Ethernet to a personal computer and the motion is controlled through the supplied Kollmorgen Workbench software. This basic software allows trapezoidal velocity profiles v_{LT} in a recurring motion as shown in figure 4.35 together with the matching acceleration a_{LT} and position x_{LT}. The motion is defined by giving time, maximum acceleration and target velocity for the constant travel part of the profile. These values were set for the experiment such that the acceleration, deceleration and constant travel times were the same, i.e. $T_{LT}/6$ in figure 4.35.

Given that the two parameters of highest interest were the acceleration (see table 4.2) and the frequencies, the corresponding maximum velocities and displacement amplitudes are shown in figure 4.36 and figure 4.37 respectively. At higher accelerations and lower frequencies the maximum displacements become very large and would exceed the travel range of the system that is determined by two ZCM-D21 limit switches for safety reasons.

For all these values the device was tested in four different orientations

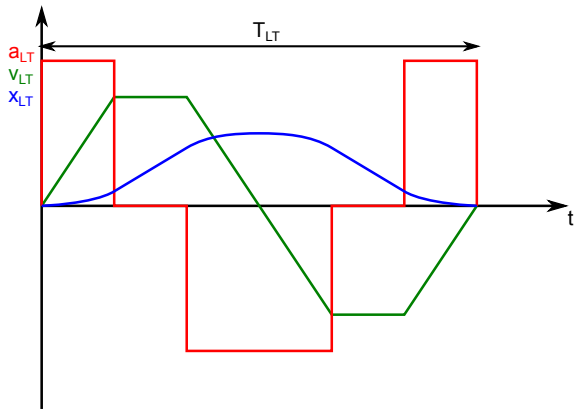

Figure 4.35: Trapezoidal velocity profile of the shaking system and corresponding acceleration and displacement profiles

Table 4.2: Accelerations used for the laboratory measurements

Symbol	**Acceleration**
a_1	1 m/s^2
a_2	2.5 m/s^2
a_3	5 m/s^2
a_4	10 m/s^2
a_5	20 m/s^2

relative to the travel direction as depicted in figure 4.38 in order to study the gravitational and inertial operation modes of a rotational harvester with eccentric proof mass as previously discussed in section 2.7. Two of the orientations are horizontal so that gravity has no effect at all. For the vertical orientations, the tests were performed once with the piezoelectric beam pointing down and once with it pointing up.

Figure 4.39 shows a photograph of the harvester in vertical orientation mounted on the linear slider on top of the belt drive. The entire system is mounted onto an optics table. The connection wires to the piezoelectric beam can be seen as well.

Finally, the voltages across a 150 kΩ load resistor were recorded using an oscilloscope and the RMS values taken over an interval of 10 s three times in a row and then averaged again to calculate the power output as the voltage squared divided by the load resistance.

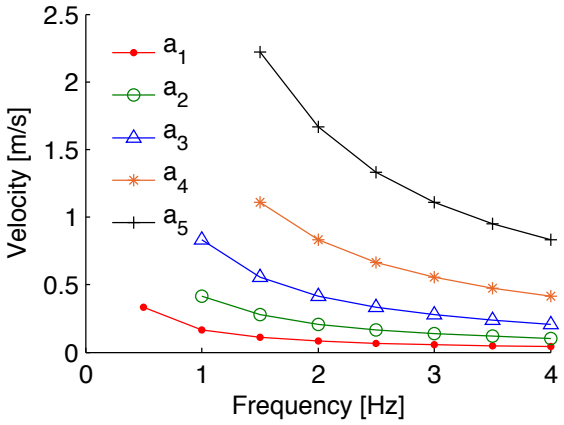

Figure 4.36: Maximum velocities at the chosen frequencies and accelerations for the device testing on the shaker system

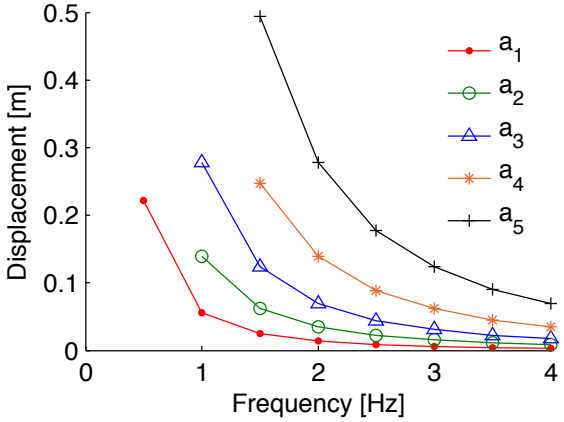

Figure 4.37: Maximum displacement amplitudes at the chosen frequencies and accelerations for the device testing on the shaker system

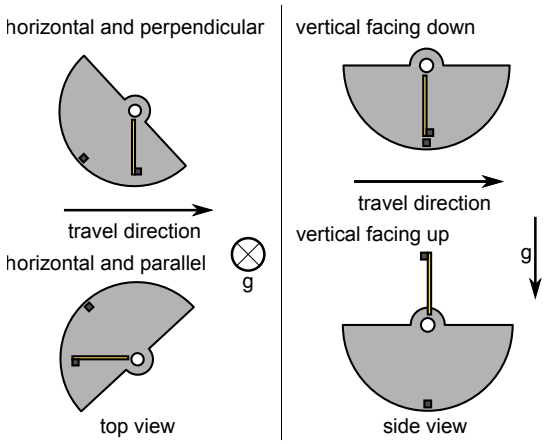

Figure 4.38: Device orientations as tested on the shaker system

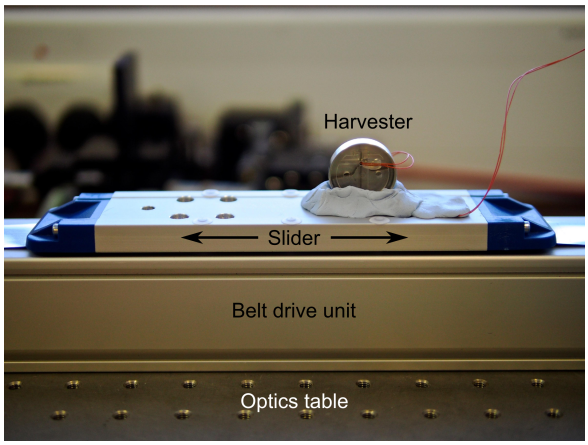

Figure 4.39: Photograph of the energy harvester in vertical orientation on top of the linear slider

Experimental results

A new device was assembled to perform these measurements after realising the quick degradation of performance in the previous real world test. The only difference is a slight increase in the gap between the permanent magnets on the beam tip and the rotor. This lowers the magnetic force significantly, leading to a smaller initial deflection of the beam before it is released to oscillate, and thus a much lower stress in the piezoelectric layers. The key here is not to overly increase the gap to prevent negative effects on the power output as discussed in section 4.1 for the proof of concept.

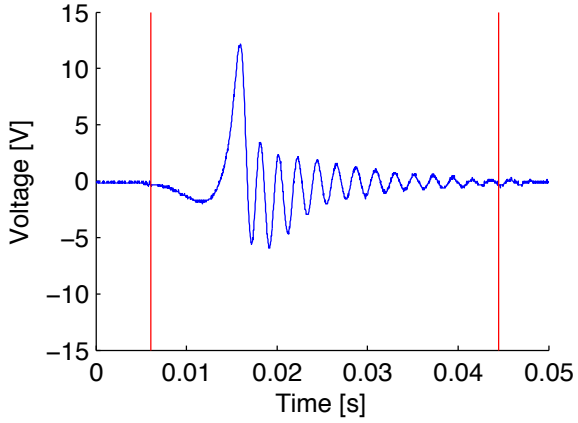

Figure 4.40: Single actuation of the piezoelectric beam taken out of a measurement at 2 Hz and acceleration 5 m/s^2, attached to a 150 kΩ load

A single actuation of the beam with a 150 kΩ load attached can be seen in figure 4.40 and without a load in figure 4.41. One observation is that the achieved voltage under load is higher than it was the case in figure 4.29, despite the weaker magnetic coupling. This leads to the assumption that the piezoelectric beam in the first device had already suffered some degradation, most likely during assembly, initial testing and handling, before the tests were started. Also, during the testing done on the new device, no significant drop in performance was seen and the overall power output is vastly improved. The repelling magnet arrangement shows up in the voltage waveform with an initial "bump" where the beam tip is pushed away by the approaching magnet before snapping through and oscillating on its own.

The vertical red lines in figures 4.40 and 4.41 indicate the boundaries

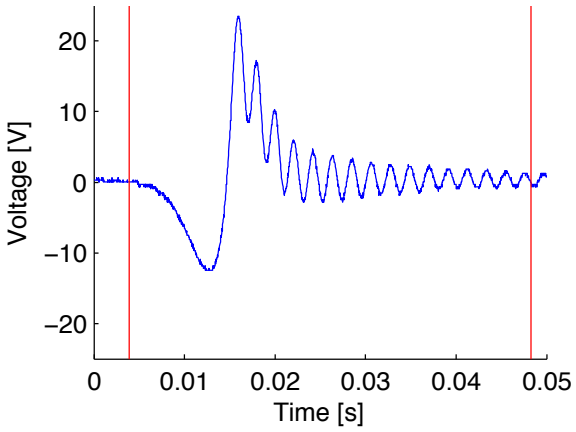

Figure 4.41: Single actuation of the piezoelectric beam taken out of a measurement at 2 Hz and acceleration 5 m/s^2, open circuit

that were used to calculate the corresponding FFTs in figures 4.42 and 4.43 respectively. These are of interest to confirm the electrical damping introduced by the load resistor indicated by the lower and wider shape of part (a) compared to part (b). Furthermore the RMS voltage over this range was calculated with a result of 5.95 V in the open circuit case and 2.49 V across the load resistor. For the latter case it is also possible to calculate the energy converted in this single actuation as 1.59 µJ and the power dissipated in the resistor as 41.2 µW over a time of 38.5 ms.

The power output for the first full series of experiments is shown in figure 4.44 for the vertical arrangement with the beam pointing down, including the standard deviation of the measurements. This is an orientation where the device is largely influenced by gravity as the tip magnet on the beam sits exactly above the stable equilibrium position of the rotor if it were on its own. Compared to an attractive magnet arrangement, the rotor can however never achieve this position as the repelling magnet pushes it away into one direction or the other and makes the equilibrium unstable. This is advantageous, since the rotor will not get stuck.

The results show that at low accelerations and frequencies, the excitation is not sufficient to make the rotor overcome the magnetic coupling force. The beam does not experience an actuation and no power is generated. In the middle range, at 5 m/s^2 the behaviour is as expected. If each actuation of the piezoelectric beam can convert a certain amount of energy, the power

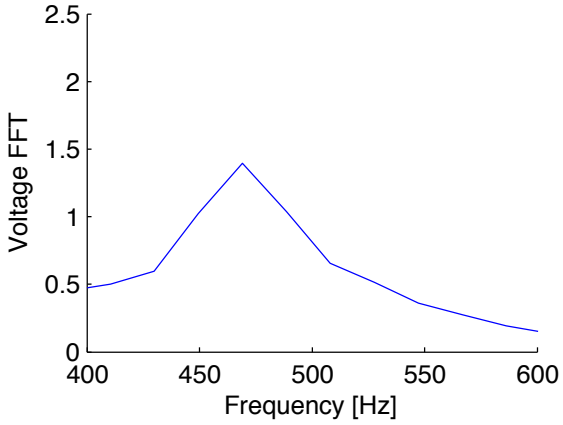

Figure 4.42: FFT graph corresponding to figure 4.40

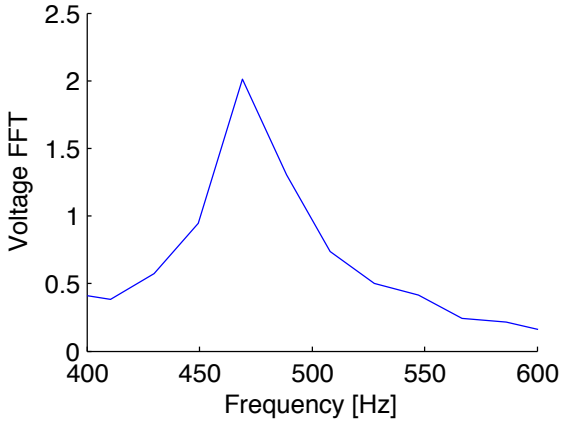

Figure 4.43: FFT graph corresponding to figure 4.41

output increases fairly linearly with the number of actuations, i.e. the frequency. Beyond that, at the two largest accelerations, different effects of the rotor dynamics start playing a role and especially around $2 - 2.5$ Hz a large jump in power output reaching up to 28 µW can be observed as well as a larger standard deviation of the measurements. In this region, the rotor starts going into a continuous rotation. Due to the complex and chaotic behaviour of an eccentric proof mass under linear excitation, the results are slightly scattered. However, a general trend for increased power output at increased frequencies and accelerations can be observed.

In direct comparison to figure 4.44, figure 4.45 shows the measurements

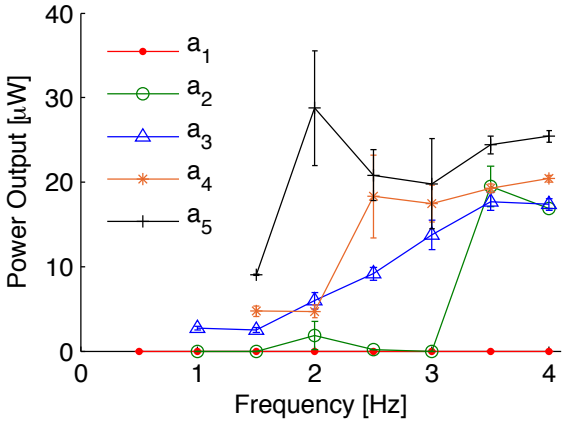

Figure 4.44: Power output measurements for the vertical orientation with the beam pointing down, including error bars for sample standard deviation

with the harvester in vertical orientation, but such that the beam points upwards. This configuration is of interest because it reaffirms some of the findings as there can only be a power output if the rotor actually rotates more than 180°, i.e. it flips over at the top. One can see that now, the largest power output is achieved at 2.5 Hz at an acceleration of 20 m/s^2 and that there is no power at any of the other accelerations up to a frequency of 3.5 Hz. It is also interesting that after hitting the peak power, there is no power output at all at the following frequency setting. Again, this is due to the dynamics at play, where one frequency might be exactly right to induce continuous rotation and a slightly higher frequency attenuates the rotor motion.

The results in figure 4.46 represent the horizontal orientation with the beam aligned with the direction of travel. The graphs support one of the key points of this work - despite the fact that gravity has no influence on the rotor in such an orientation, the device operates due to the inertial reaction forces on the eccentric proof mass. It was observed during the experiment that the result can depend on initial conditions. In the vertical case, the rotor always assumes a certain position at rest due to gravity. Even in the case where the magnet on the beam pushes the rotor away it will find a position "hovering" to either side of the beam. In the horizontal case on the other hand, the starting position is more or less random.

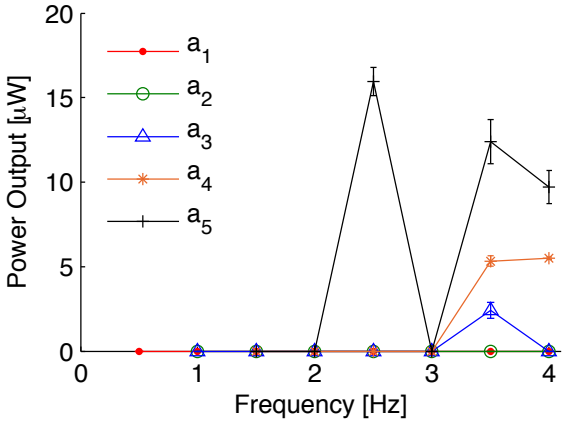

Figure 4.45: Power output measurements for the vertical orientation with the beam pointing up, including error bars for sample standard deviation

Nevertheless, the graphs show a decent power output of at least several microwatts across the range. One interesting effect is that even at the lower accelerations and frequencies, energy was successfully harvested up to a certain point, where the generation stopped. Furthermore, the absolute best result of 43 μW was achieved at an acceleration of 20 m/s^2 when a very fast continuous rotation was observed. Generally, an increase of power output with frequency and acceleration can be seen just as was the case in vertical orientation.

The final set of measurements was carried out in a horizontal arrangement with the beam perpendicular to the direction of motion and the results are shown in figure 4.47. At low frequencies, the power output and voltages are very scattered, which is probably due to initial conditions. Despite not exhibiting quite such high power at 2 Hz, the other results from the parallel configuration are reproduced beyond this frequency. The power output increases with the frequency and acceleration level and for the lower accelerations, no power is generated at higher frequencies. This last effect can actually be explained by looking at figure 4.37 - at low accelerations and high frequencies the displacement amplitudes are very small, in the range of several millimetres only.

Finally, it is interesting that frequencies around 2 Hz exhibit a special behaviour, despite a higher pendulum natural frequency calculated as ap-

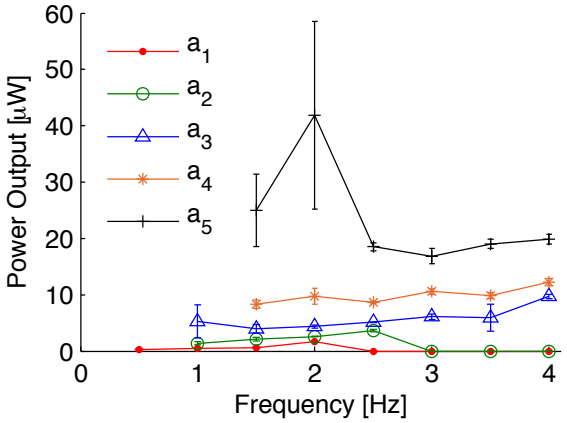

Figure 4.46: Power output measurements for the horizontal orientation with the beam parallel to the travel direction, including error bars for sample standard deviation

proximately 5.6 Hz, as discussed earlier. The measurements around this frequency are also less consistent as can be seen from the error bars. Measurements up to higher frequencies could provide further detail, but are unfortunately not possible on the described set-up. However, the phenomenon of one frequency showing much higher power output is consistent with results from the very first proof of concept presented earlier in section 4.1.

4.3.4 Conclusions

After introducing the finalised device, this section presents a real world test. The portable measurement system is described and the results discussed. The FFT diagrams of the generated voltage and the corresponding accelerometer data confirm frequency up-conversion from the low source frequency to the higher transducer frequency. While this version of the prototype displayed a maximum power output of 7 µW during running, a quick degradation of the performance was also noticed. The explanation is an over-stressing of the piezoelectric bending beam, caused by an excessive magnetic coupling force. The mechanics of the design, i.e. the bearing system with attached rotor and the entire assembly with lid and casing survived the tests without any signs of wear. The problem of degradation was addressed by increasing the gap between the permanent magnets that make up the coupling between rotor and beam tip, and thus lowering the inter-

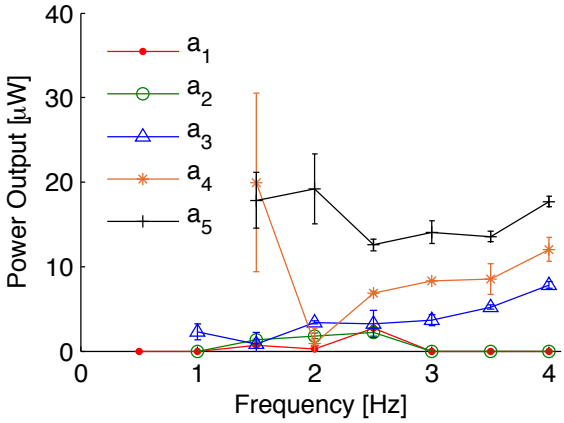

Figure 4.47: Power output measurements for the horizontal orientation with the beam perpendicular to the travel direction, including error bars for sample standard deviation

action force and the initial deflection of the beam. Nonetheless, the topic of degradation of piezoelectric materials for energy harvesting is highly interesting. A lot of research has been done on fatigue of PZT [213, 214, 215] and the life time of multilayer stack actuators [216, 217, 218, 219]. However, most of these articles look at the problem from the electrical side rather than investigating the effects of mechanical loading. Even if this is the case, as in [220, 221], the focus is not on energy harvesting from bending beams where it is the goal to extract the maximum possible power and thus to place a large stress on the beams.

The benefit of the alteration to the magnetic coupling was confirmed in a laboratory based series of tests carried out on a custom made linear excitation system. Four different device orientations in the gravitational and the inertial operation modes of the device were tested. The ability of the harvester to work regardless of orientation was demonstrated by the results, and the power output was improved over the previous tests. It was shown that the rotor dynamics play a major part in the characteristics of the harvester and that it can be affected by initial conditions. At certain frequencies, mainly around 2 Hz, this particular device has a tendency for the rotor to go into a continuous rotation and when this happens a peak power output of 43 μW was achieved. For a functional volume of 1.85 cm^3 this equates to a power density of 23.2 $\mu W/cm^3$ at a frequency of 2 Hz and an accelera-

tion of 20 m/s^2. Even besides this peak value, power outputs in the range of tens of microwatts were achieved in most experiments. This compares favourably to the estimated power output from the Seiko Kinetic wristwatch, although further studies on the actual performance of the Seiko Kinetic and an experiment of this device when worn on the wrist during a normal day would be beneficial and will be subject to further work. Ultimately, the main advantages of this new piezoelectric transduction mechanism over the electromagnetic Seiko harvester are the simplicity of the design, avoiding physical contact between parts, reducing wear and the limited number of components.

5 Magnetic Plucking of Piezoelectric Beams

The purpose of this chapter is to introduce an experimentally validated simulation model for magnetic actuation of piezoelectric beams. The model is based on the distributed parameter solutions for bimorph beams given by Erturk and Inman [119]. The difference is that in the case of beam plucking, there is no base excitation but rather an initial deflection of the tip or a force acting on the tip. Modelling of both these scenarios will be introduced and two different methods to incorporate magnetic actuation and the corresponding results will be discussed. The majority of the findings are published in the IOP Journal Smart Materials and Structures [222].

5.1 Model of the Piezoelectric Bimorph Beam

5.1.1 Modelling Approaches

Generally there are two approaches that have been considered to solve the constitutive piezoelectric equations for thin bimorph beams under harmonic base excitation and there are many literature resources discussing these. The first one is a lumped parameter approach described by Roundy and Wright [117], Priya for his piezoelectric windmill [223], Ajitsaria et al. [224] and Kim et al. [225].

The second method is an exact distributed parameter approach described by Dalzell and Bonello [226], Lu et al. [227] or Ballas [228]. Buchberger and Schoeftner compare analytical results with three dimensional finite element calculations [229] and Liao and Sodano discuss the optimal placement of piezoelectric patches on cantilevers [230].

The most comprehensive work on the topic has been presented by Erturk and Inman [231, 119]. For this reason, the analysis in this chapter is based around their distributed parameter model and will be introduced for the

case of a bimorph piezoelectric beam with the two layers connected in series (see figures 5.1 and 5.2). The model needs to be adjusted for plucking actuation. The equations need to be solved with an initial condition given by the deflection, caused by the tip force on the beam before release. For easier reference, the nomenclature throughout this chapter was kept the same as in [119] wherever possible.

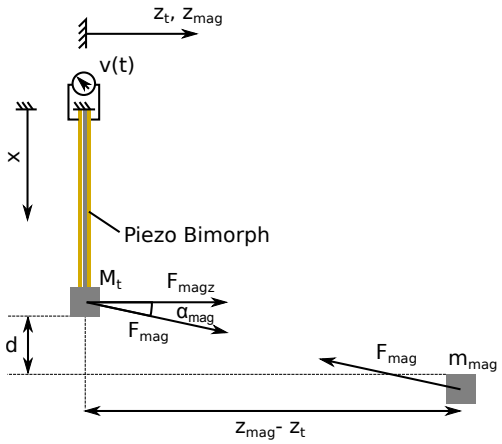

Figure 5.1: Magnetic plucking of a piezoelectric beam

5.1.2 Coupled Mechanical Equations and Modal Analysis

In this section, unless otherwise stated, only the case of the series connected bimorph beam will be considered. Figure 5.2 introduces the structure and geometry of such a beam, while figure 5.3 depicts an electrical equivalent circuit.

The parameters used in these figures are L, the length of the beam, b, the width, $h_{\tilde{p}}$, the thickness of a single piezoelectric layer, $h_{\tilde{s}}$, the thickness of the substructure layer, M_t an added tip mass, R_l the attached load resistance, $v_s(t)$ the voltage measured for the series connection, $i^s_{\tilde{p}}(t)$ is the current source for a single layer and $C_{\tilde{p}}$ is the capacitance for a single layer.

The governing equation for the piezoelectric cantilever beam is given by Erturk and Inman [119] as:

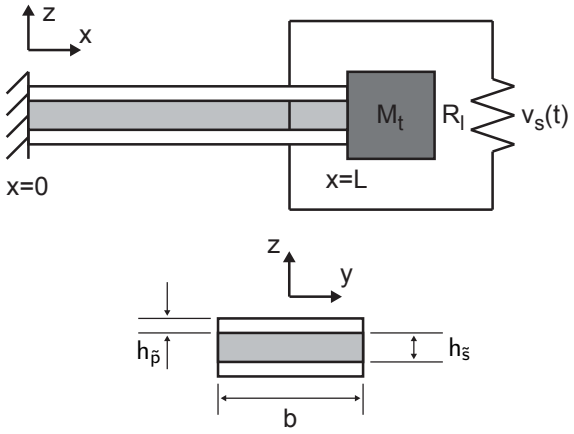

Figure 5.2: Series connected bimorph piezoelectric beam, adapted from [119]

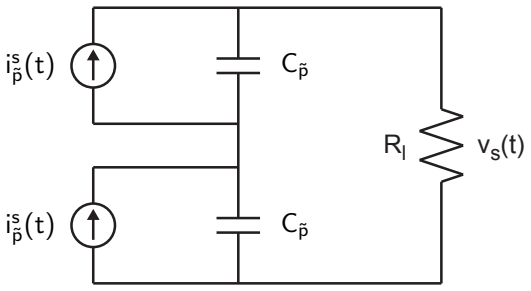

Figure 5.3: Equivalent circuit for series connected bimorph piezoelectric beams, reproduced from [119]

$$-\frac{\partial^2 M(x,t)}{\partial x^2} + c_s I \frac{\partial^5 w_{rel}(x,t)}{\partial x^4 \partial t} + c_a \frac{\partial w_{rel}(x,t)}{\partial t} + m_p \frac{\partial^2 w_{rel}(x,t)}{\partial t^2} = -[m_p + M_t \delta(x-L)] \frac{\partial^2 w_b(x,t)}{\partial t^2} \quad (5.1)$$

where $M(x,t)$ is the internal bending moment term, $c_s I$ is the strain rate damping coefficient, c_a, the air damping, m_p is the mass per unit length of the beam and δ is the dirac delta function. This equation can be simplified for the case without base excitation by setting $w_b(x,t) = 0$, and throughout this text the notation is shortened by introducing that the displacement relative to the now fixed base $w_{rel}(x,t) = w(x,t)$ which gives:

$$-\frac{\partial^2 M(x,t)}{\partial x^2} + c_s I \frac{\partial^5 w(x,t)}{\partial x^4 \partial t} + c_a \frac{\partial w(x,t)}{\partial t} + m_p \frac{\partial^2 w(x,t)}{\partial t^2} = 0 \qquad (5.2)$$

Despite the right hand term disappearing, this expression is still valid for beams with an added tip mass, e.g. a permanent magnet. It will be accounted for in the calculation of natural frequencies before transforming into modal coordinates later on. After the evaluation of the internal bending moment the following relationship is found:

$$YI\frac{\partial^4 w(x,t)}{\partial x^4} + c_s I \frac{\partial^5 w(x,t)}{\partial x^4 \partial t} + c_a \frac{\partial w(x,t)}{\partial t} + m_p \frac{\partial^2 w(x,t)}{\partial t^2} - \theta_s v_s(t)\left[\frac{d\delta(x)}{dx} - \frac{d\delta(x-L)}{dx}\right] = 0 \qquad (5.3)$$

In this equation the derivative of the Dirac δ function is a result of previously introducing the Heaviside step function necessary due to the fact that the piezoelectric coupling term is only a function of time and would otherwise not survive the spatial differentiation. The backward coupling term θ_s is determined by the piezoelectric stress constant $\bar{e}_{31}$ and the geometry of the beam:

$$\theta_s = \frac{\bar{e}_{31} b}{2h_{\tilde{p}}}\left[\left(h_{\tilde{p}} + \frac{h_{\tilde{s}}}{2}\right)^2 - \frac{h_{\tilde{s}}^2}{2}\right] \qquad (5.4)$$

The overall bending stiffness term is a function of the elastic stiffness $\bar{c}_{11}^E$, the Young's modulus of the substructure layer $Y_{\tilde{s}}$ and geometric properties:

$$YI = \frac{2b}{3}\left(Y_{\tilde{s}}\frac{h_{\tilde{s}}^3}{8} + \bar{c}_{11}^E\left[\left(h_{\tilde{p}} + \frac{h_{\tilde{s}}}{2}\right)^3 - \frac{h_{\tilde{s}}^3}{8}\right]\right) \qquad (5.5)$$

The mass per unit length m_p is easily calculated based on the geometry and the respective densities of the piezoelectric and substructure layers $\rho_{\tilde{p}}$ and $\rho_{\tilde{s}}$:

$$m_p = b(\rho_{\tilde{s}} h_{\tilde{s}} + 2\rho_{\tilde{p}} h_{\tilde{p}}) \qquad (5.6)$$

Assuming modal damping, the motion of the beam can be represented as the following convergent sum of eigenfunctions:

$$w(x,t) = \sum_{r=1}^{\infty} \phi_r(x)\eta_r(t) \tag{5.7}$$

where $\eta_r(t)$ is the modal mechanical coordinate of the r^{th} mode and $\phi_r(x)$ is the mass-normalized eigenfunction of the r^{th} mode of the corresponding undamped free vibration problem (this can be justified by using modal damping only, as is common practice):

$$\phi_r(x) = A_r \left[\cos\frac{\lambda_r}{L}x - \cosh\frac{\lambda_r}{L}x + \varsigma_r \left(\sin\frac{\lambda_r}{L}x - \sinh\frac{\lambda_r}{L}x \right) \right] \tag{5.8}$$

with ς_r as follows:

$$\varsigma_r = \frac{\sin\lambda_r - \sinh\lambda_r + \lambda_r \frac{M_t}{m_p L}(\cos\lambda_r - \cosh\lambda_r)}{\cos\lambda_r + \cosh\lambda_r - \lambda_r \frac{M_t}{m_p L}(\sin\lambda_r - \sinh\lambda_r)} \tag{5.9}$$

A_r is a modal amplitude constant that needs to be determined by normalizing the eigenfunction according to the following orthogonality condition, where the indices s and r indicate the considered modes:

$$\int_0^L \phi_s(x) m_p \phi_r(x) dx + \phi_s(L) M_t \phi_r(L) + \left[\frac{d\phi_s(x)}{dx} I_t \frac{d\phi_r(x)}{dx} \right]_{x=L} = \delta_{rs} \tag{5.10}$$

For the sake of simplification, it is possible to consider only a single mode, i.e. $r = s$. The Kronecker delta becomes $\delta_{rs} = 1$ and the result is:

$$m_p \int_0^L \phi_r^2(x) dx + M_t \phi_r^2(L) + I_t \left(\left[\frac{d\phi_r(x)}{dx} \right]_{x=L} \right)^2 = 1 \tag{5.11}$$

Furthermore, in [232] Rao arrives at an additional form of orthogonality relation:

$$\int_0^L \phi_s(x) Y I \frac{d^4\phi_r(x)}{dx^4} = \omega_r^2 \delta_{rs} \tag{5.12}$$

I_t in these equations is the mass moment of inertia of the tip mass around the beam tip and to complete the model, the undamped natural frequency of the r^{th} vibration mode in short-circuit conditions can be found as:

$$\omega_r = \lambda_r^2 \sqrt{\frac{YI}{m_p L^4}} \tag{5.13}$$

where the eigenvalues λ_r are the solutions to the general equation:

$$\begin{aligned} &1 + \cos\lambda\cosh\lambda + \lambda\frac{M_t}{m_p L}(\cos\lambda\sinh\lambda - \sin\lambda\cosh\lambda) \\ &- \frac{\lambda^3 I_t}{m_p L^4}(\cosh\lambda\sin\lambda + \sinh\lambda\cos\lambda) + \frac{\lambda M_t I_t}{m_p^2 L^4}(1 - \cos\lambda\cosh\lambda) = 0 \end{aligned} \tag{5.14}$$

The next step is to insert equation (5.7) in equation (5.3), which yields the following for each mode of vibration:

$$\begin{aligned} YI\frac{d^4\phi_r(x)}{dx^4}\eta_r(t) + c_s I\frac{d^4\phi_r(x)}{dx^4}\frac{d\eta_r(t)}{dt} + c_a\phi_r(x)\frac{d\eta_r(t)}{dt} \\ + m_p\phi_r(x)\frac{d^2\eta_r(t)}{dt^2} - \theta_s v_s(t)\left[\frac{d\delta(x)}{dx} - \frac{d\delta(x-L)}{dx}\right] = 0 \end{aligned} \tag{5.15}$$

Multiplying equation (5.15) with $\phi_r(x)$ and integrating over the entire length of the beam leads to:

$$\begin{aligned} &\int_0^L \phi_r(x) YI\frac{d^4\phi_r(x)}{dx^4}\eta_r(t)dx + \int_0^L \phi_r(x) c_s I\frac{d^4\phi_r(x)}{dx^4}\frac{d\eta_r(t)}{dt}dx \\ &\quad + \int_0^L \phi_r(x) c_a\phi_r(x)\frac{d\eta_r(t)}{dt}dx + \int_0^L \phi_r(x) m_p\phi_r(x)\frac{d^2\eta_r(t)}{dt^2}dx \\ &\quad - \int_0^L \theta_s v_s(t)\left[\phi_r(x)\frac{d\delta(x)}{dx} - \phi_r(x)\frac{d\delta(x-L)}{dx}\right]dx = 0 \end{aligned} \tag{5.16}$$

At this point it is helpful to recall the properties of the Dirac delta function, where the nth derivative satisfies:

$$\int_{-\infty}^{\infty} \frac{d^{(n)}\delta(x-L)}{dx^{(n)}}\phi_r(x)dx = (-1)^n \left.\frac{d^{(n)}\phi_r(x)}{dx^{(n)}}\right|_{x=L} \tag{5.17}$$

Using equation (5.17) together with the orthogonality conditions (5.11) and (5.12) for the case without a tip mass, equation (5.3) can ultimately be written in its modal form:

$$\frac{d^2\eta_r(t)}{dt^2} + 2\zeta_r\omega_r\frac{d\eta_r(t)}{dt} + \omega_r^2\eta_r(t) - \theta_s v_s(t)\left.\frac{d\phi_r(x)}{dx}\right|_{x=L} = 0 \tag{5.18}$$

For the case without a tip mass ($M_t = 0$), damping can be calculated as follows:

$$2\zeta_r\omega_r = \frac{c_s I\omega_r^2}{YI} + \frac{c_a}{m_p} \tag{5.19}$$

However, in most cases it is more practical to experimentally determine ζ_r and one method will be described in section 5.1.5.

5.1.3 Coupled Electrical Circuit Equation

Beam bending is in fact a one dimensional problem and thus the relevant piezoelectric constitutive equation simplifies to:

$$D_3 = \bar{e}_{31}S_1^{\tilde{p}} + \bar{\varepsilon}_{33}^S E_3 \tag{5.20}$$

where D_3 is the electric displacement compononent, $\bar{e}_{31}$ is the effective piezoelectric stress constant, $S_1^{\tilde{p}}$ is the strain component in x-direction, $\bar{\varepsilon}_{33}$ is the permittivity component at constant stress and E_3 the electric field in z-direction. From the integral form of Gauss's law, the electric current output can be found as:

$$\frac{d}{dt}\left(\int_{A_e}\mathbf{D}\cdot\mathbf{n}dA_e\right) = \frac{v(t)}{R_l} \tag{5.21}$$

In this case A_e describes the electrode area which is assumed to be continuous over the entire beam. $\mathbf{D}$ is the vector of electric displacement components and $\mathbf{n}$ is a unit outward normal vector. Note the use of $v(t)$ rather than $v_s(t)$ for the piezoelectric voltage in these equations as only a single layer is considered and the equations are thus valid for series and parallel connection at this stage.

The average bending strain can be expressed in terms of the curvature and the electric field can be written as:

$$E_3(t) = -\frac{v(t)}{h_{\tilde{p}}} \tag{5.22}$$

With this we can substitute (5.21) in (5.20) and use the modal expansion form of the transverse vibration response to find:

$$\frac{\bar{e}_{33}^{S} bL}{h_{\tilde{p}}} \frac{dv(t)}{dt} + \frac{v(t)}{R_l} + \sum_{r=1}^{\infty} \kappa_r \frac{d\eta_r(t)}{dt} = 0 \tag{5.23}$$

Where κ_r is the modal coupling term in the electrical circuit equation:

$$\kappa_r = \bar{e}_{31} h_{\tilde{p}c} b \left. \frac{d\phi_r(x)}{dx} \right|_{x=L} \tag{5.24}$$

Looking at the specific case of series connection and after applying Kirchhoff's laws to the equivalent circuit in 5.3 we can write:

$$\frac{C_{\tilde{p}}}{2} \frac{dv_s(t)}{dt} + \frac{v_s(t)}{R_l} - i_{\tilde{p}}^{s}(t) = 0 \tag{5.25}$$

and by matching this to equation (5.23) we can extract the following:

$$C_{\tilde{p}} = \frac{\bar{\varepsilon}_{33}^{S} bL}{h_{\tilde{p}}} \tag{5.26}$$

and

$$i_{\tilde{p}}^{s}(t) = -\sum_{r=1}^{\infty} \kappa_r \frac{d\eta_r(t)}{dt} \tag{5.27}$$

5.1.4 Initial Conditions and External Forcing in Modal Coordinates

There are two situations that are encountered when plucking a piezoelectric beam at the tip. One can either assume an initial tip deflection, i.e. due to a static force, which works well when actuating with a plectrum, or one can assume an external dynamic force on the tip, as is the case for magnetic actuation. In the first case, to determine the initial conditions, it is assumed that the beam is deflected by a certain amount $w(x,0)$ at the beginning and that the voltage is zero, $v_s(0) = 0$. The velocity will be zero as well, $\frac{d\eta_r}{dt}(0) = 0$. In order to deflect the tip, a static force Q in the positive z-direction is applied and the shape is then given as:

$$w_0 = w(x,0) = \frac{QL}{YI} \left(\frac{x^2}{2} - \frac{x^3}{6L} \right) \tag{5.28}$$

The orthogonality condition can then be used to find a solution for $\eta_r(0)$:

$$\eta_r(0) = \int_0^L w(x,0) m_p \phi_r(x) dx + w(L,0) M_t \phi_r(L) + \left[\frac{dw(x,0)}{dx} I_t \frac{d\phi_r(x)}{dx} \right]_{x=L} \quad (5.29)$$

In the second case, under the assumption of a distributed force per length $f(x,t)$ acting in the positive z-direction the modal force can be expressed as :

$$F_r(t) = \int_0^L \phi_r(x) f(x,t) dx \quad (5.30)$$

which, in the case of a tip force acting on a single point, simplifies to:

$$F_r(t) = f(L,t) \cdot \phi_r(L) \quad (5.31)$$

More detail on these relationships and further examples on different cases are given by Rao in [232]. In this regard, Roark's Formulas for Stress and Strain [233] are also a comprehensive reference.

5.1.5 Model Implementation

Equivalent Model and Assumptions

To calculate the voltages and displacements of the piezoelectric bimorph, the above equations were used in an equivalent form, that simplifies programming and determination of parameters. The modelling was then done in Matlab/Simulink.

The equivalent equation for the modal mechanical coordinate is:

$$\frac{d^2\eta_r(t)}{dt^2} + 2\zeta_r\omega_r \frac{d\eta_r(t)}{dt} + \omega_r^2 \eta_r(t) - \tilde{\theta}_r^s v_s(t) = F_r(t) \quad (5.32)$$

and the equivalent equation for the voltage response is:

$$C_{\tilde{p}}^{eq,s} \frac{dv_s(t)}{dt} + \frac{v_s(t)}{R_l} + \sum_{r=1}^{\infty} \tilde{\theta}_r^s \frac{d\eta_r(t)}{dt} = 0 \quad (5.33)$$

For the series connection case the necessary equivalent modal electromechanical coupling term $\tilde{\theta}_r^s$ and the equivalent piezoelectric capacitance $C_{\tilde{p}}^{eq,s}$

are:

$$\tilde{\theta}_r^s = \bar{e}_{31} b h_{\tilde{p}c} \left. \frac{d\phi_r(x)}{dx} \right|_{x=L} \tag{5.34}$$

and

$$C_{\tilde{p}}^{eq,s} = \frac{\bar{\varepsilon}_{33}^S b L}{2 h_{\tilde{p}}} \tag{5.35}$$

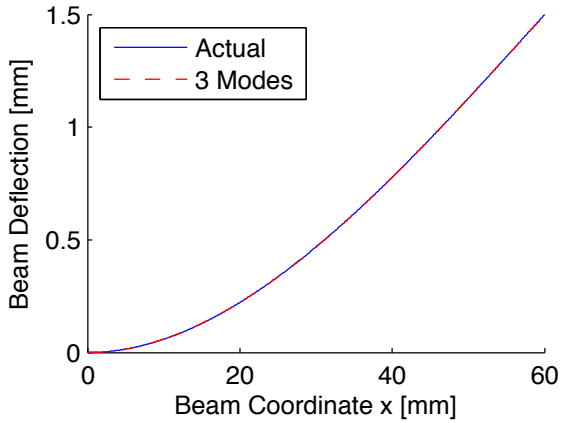

Figure 5.4: Third order approximation of initial beam deflection

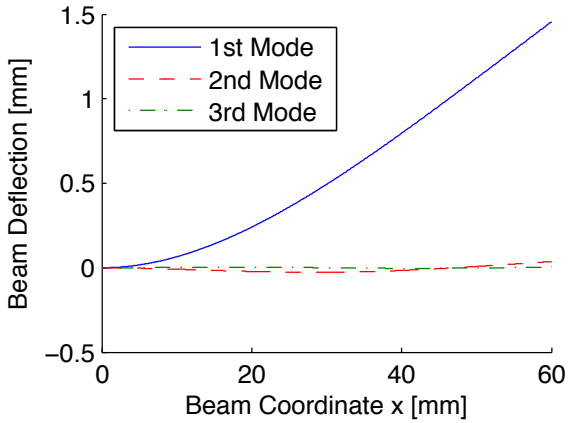

Figure 5.5: Contributions of the first three modes to the modal decomposition of the initial condition

Furthermore, the equations were solved up to the third vibration mode only. This is a reasonable assumption given that the device is to operate

under simple beam bending, i.e. close to the first mode, and higher modes are thus of little interest and their contributions are small. Figures 5.4 and 5.5 show the third order approximation of the initial deflection and the contribution of each of the three mode shapes to this initial deflection respectively and support the claim that the higher order modes have very little effect in this case.

Experimental Determination of Damping Factors

Making reliable assumptions for the mechanical damping values ζ_r is very involved and the best way to get reasonable values is through experiment. Under the assumption of modal damping, the coefficients for each mode can be calculated from only two damping values of different modes ω_j and ω_k via the relationship given in [119]:

$$\begin{bmatrix} c_s I \\ c_a \end{bmatrix} = \frac{2\omega_j\omega_k}{\omega_j^2 - \omega_k^2} \begin{bmatrix} \frac{YI}{\omega_k} & -\frac{YI}{\omega_j} \\ -m_p\omega_k & m_p\omega_j \end{bmatrix} \begin{bmatrix} \zeta_j \\ \zeta_k \end{bmatrix} \tag{5.36}$$

The method used to determine the damping factors of the first and second mode for the piezoelectric beams described in the experimental set-up was via the logarithmic decrement applied to the voltage output measured with an oscilloscope when letting the beam ring down after manually giving it an initial deflection:

$$\delta_r = \frac{1}{n} \log \frac{v(t)}{v(t + nT_r)} \tag{5.37}$$

and

$$\zeta_r = \frac{1}{\sqrt{1 + (\frac{2\pi}{\delta_r})^2}} \tag{5.38}$$

where T_r describes the period of one oscillation and n the number of oscillations taken into account.

Ideally, this measurement would be performed under short circuit conditions, as one is only interested in the mechanical damping. However, this is not feasible because it is impossible to measure the voltage in that case. As a consequence, the voltage drop across a 500 Ω resistor was measured as this gives a reasonable signal to noise ratio while at the same time keeping the

influence of electrical damping low (piezoelectric elements generally have a high impedance, in this particular case around 120 kΩ).

Furthermore, the method of the logarithmic decrement could only be used for the damping factor of the second mode by filtering out the contribution of the first mode with a Butterworth filter applied to the voltage signal in post processing.

For both modes, the voltage oscillation peaks were determined and an exponential decay was fitted through the data points before determining the damping values from the fitted data:

$$v_{peak}(t) = De^{Et} \tag{5.39}$$

with D and E being the fit parameters in Matlab (in this case E takes on a negative value). This procedure ensures a good approximation that is independent of individual erroneous data points and it is shown in figures 5.6 and 5.7. The resulting values for this particular beam are $\zeta_1 = 0.0175$ and $\zeta_2 = 0.02$.

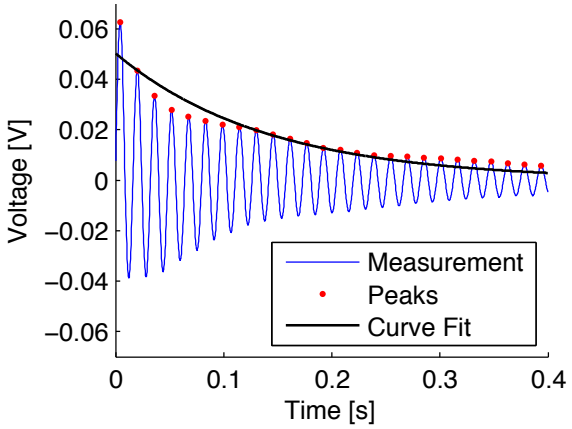

Figure 5.6: Experimental determination of modal damping parameters, showing measured voltage, peaks and corresponding exponential curve fit for the first mode

5.1.6 Model Validation Under Initial Tip Deflection

The piezoelectric modelling described above was first validated without including the magnetic coupling by releasing the beam after an initial tip

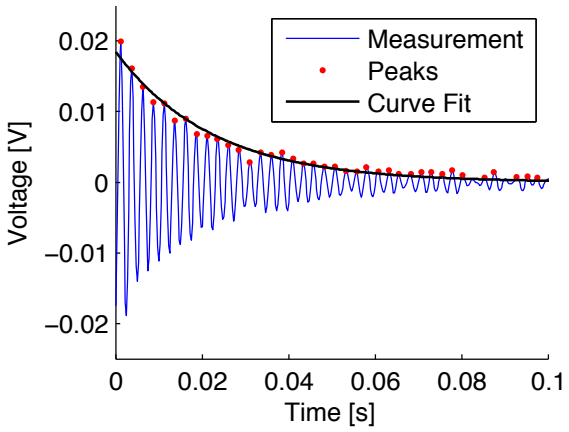

Figure 5.7: Experimental determination of modal damping parameters, showing measured voltage, peaks and corresponding exponential curve fit for the second mode, after filtering out the lower frequency components

deflection. This section describes the procedure and results.

Experimental Set-up

Figure 5.8 shows the experimental set-up used for the validation of the beam plucking simulation. A needle mounted on a micrometre alignment stage was used to first lightly contact the beam tip - this point can be made out by a slight voltage response on the oscilloscope. From that point, the alignment stage was lowered to give 1.5 mm tip deflection. In this position the beam was given enough time for the voltage to go back down to zero and then released by pulling the needle back with the x-axis of the alignment stage.

The Morgan PZT507 beam, previously used in chapter 3 was again used for these measurements and the complete list of simulation parameters for this beam and material are summarised in table 5.1. The beam with an original length of 74 mm was clamped to a free length of 60 mm. The electrodes on the top and bottom extend over the entire length of the beam however. This needs to be accounted for in the simulation model by calculating the equivalent capacitance $C_{\tilde{p}}^{eq,s}$ over the entire 74 mm according to equation (5.35). However, the best practice is to replace the calculated value by a measured value from the beam, which was done with a Wayne Kerr component analyser, resulting in 24.6 nF, measured at a frequency of 1 kHz and a

voltage of 0.5 V, the standard settings used by Morgan Piezoceramics.

Table 5.1: Simulation parameters for Morgan Piezoceramics PZT507 series connected bimorph beam

Parameter	**Value**
L	60 mm
b	5 mm
$h_{\tilde{p}}$	0.2 mm
$h_{\tilde{s}}$	0.11 mm
$\rho_{\tilde{s}}$	8200 kg/m^3
$\rho_{\tilde{p}}$	7800 kg/m^3
M_t	190 mg
I_t	1.71×10^{-9} kgm^2
Y_s	150×10^9 N/m^2
$\bar{c}_{11}^E$	62.5×10^9 N/m^2
d_{31}	-360×10^{-12} m/V
$\bar{e}_{31}$	-22.5 Vm/N
$C_{\tilde{p}}^{eq,s}$	24.6 nF
ε_{33}^S	30.9×10^{-9} F/m

The clamping of the beam itself turned out to be of major importance. The best results were achieved with two layers of thin perspex as isolators, when clamping the beam between two aluminium bars. The differences in natural frequency can be up to 15 % with inappropriate clamping. As was discussed in chapter 4, avoiding the clamping altogether by gluing the beam with epoxy resin is even more reliable. However, a glued connection can not be released without destruction of the beam and so a clamping mechanism is more practical for initial validation.

Three different resistor values were investigated for R_l. The first measurements were performed with a 500 Ω resistor, which is reasonably close to short circuit conditions given the high electrical impedance of piezoelectric materials. As an impedance matched resistive load a 120 kΩ resistor was used. This is the value used for the beam with tip mass in chapter 3 and was therefore used again here. The ideal impedance match might be slightly different when there is no tip mass, but for validation of the simulation model this does not have any negative effects. Finally, the open circuit measurements assume an impedance of 10 MΩ because this corresponds to the probe impedance of the oscilloscope.

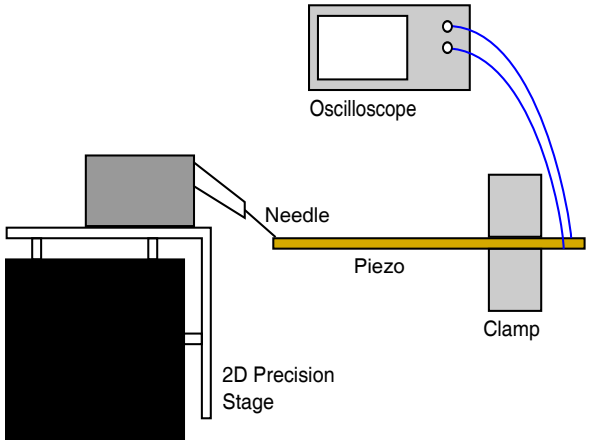

Figure 5.8: Experimental set-up for the validation of the piezoelectric Simulink model

Results

The damping values for the simulations were determined as described earlier in section 5.1.5 and the measurements were performed for a beam with and without a tip mass.

Beam without tip mass Figure 5.9 shows the open circuit, i.e. 10 MΩ resistive load, voltage measurement for the beam and figure 5.10 is the corresponding simulation. The general shape of the oscillation between the measurement and the simulation corresponds reasonably well, especially the effect, that under open circuit conditions the voltage does not oscillate around zero. The reason for this is to be found in the measurement procedure. The initial deflected state of the beam is held until the voltage has gone to zero, due to leakage currents. The probe impedance is very high and the resulting RC time constant delays the return to the initial neutral voltage. The simulated displacement at the tip in figure 5.11 reflects this as well, with a slight residual deflection remaining for a while before the beam finds back to its neutral position. The peak voltage is significantly higher in the simulation. It is believed that this is due to material degradation and will be discussed further on in the conclusions.

All of the measurement graphs are very similar, which is why only one further result of interest is shown in figure 5.12 for a magnified view of the simulated voltage waveform in close to short circuit condition (500 Ω).

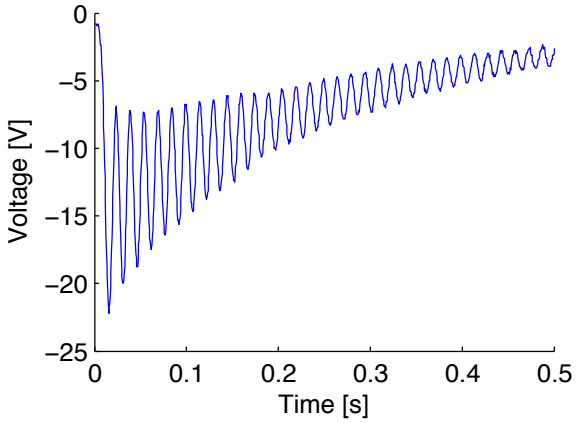

Figure 5.9: Beam plucking, measured voltage with 10 MΩ resistive load

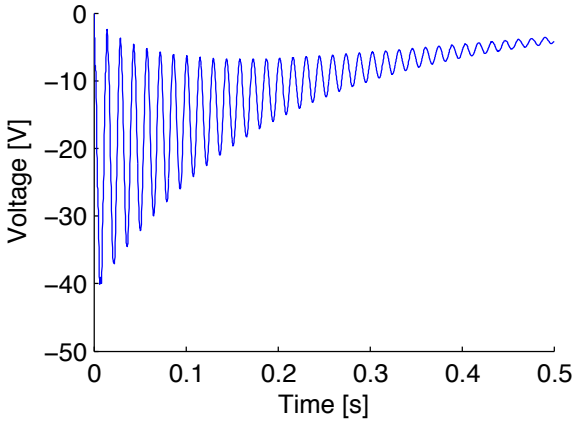

Figure 5.10: Beam plucking, simulated voltage with 10 MΩ resistive load

In good agreement with the measurement results, the influence of higher oscillation modes can clearly be seen in the first number of voltage peaks.

Table 5.2 sums up the comparison between measurement and simulation without a tip mass. The damping of the first mode ζ_1 and the corresponding natural frequency ω_1 is given together with the maximal voltage of the first peak of the decaying waveform V_{peak}. The simulated voltages are consistently higher but the natural frequencies are generally very close. The damping value for the 500 Ω measurement was used for the simulation so they are the same. At a higher load resistance of 120 kΩ, the damping in the simulation is much larger. It is expected that at this load, close to the

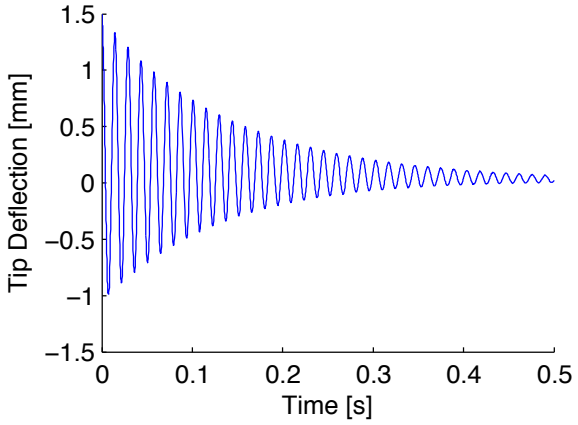

Figure 5.11: Beam plucking, simulated displacement with 10 MΩ resistive load

Table 5.2: Comparison between simulation and measurement for a beam without tip mass

R_l		ζ_1	ω_1	V_{peak}
10 MΩ	**sim**	0.0176	69.4 Hz	40.0 V
	meas	0.0149	66.4 Hz	23.0 V
120 kΩ	**sim**	0.0444	67.8 Hz	19.7 V
	meas	0.029	66.4 Hz	9.7 V
500 Ω	**sim**	id.	65.5 Hz	0.17 V
	meas	0.0175	64.5 Hz	0.075 V

impedance match, the electrical damping is largest and this discrepancy further supports the possibility of degradation problems with the piezoelectric beams as discussed earlier with regard to the maximum voltages.

Furthermore, when the beam was initially tested in chapter 3, a capacitance of 30 nF was measured and when calculated according to equation (5.35) over the entire 74 mm a capacitance of 28.5 nF results. Given the good general agreement, i.e. frequencies and shape of the waveforms, the assumption of degradation or general deviation of the real parameters from the data sheet seems a plausible cause for the discrepancies in the voltage.

Beam with tip magnet The same measurements as in the previous section were performed with a magnet attached to the tip of the beam

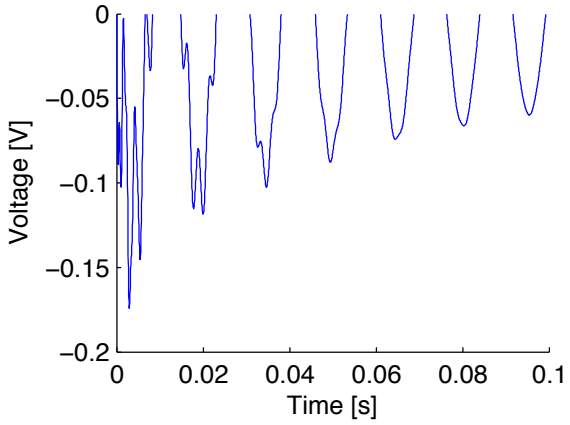

Figure 5.12: Beam plucking, simulated voltage with 500 Ω resistive load, detailed view

acting as tip mass. The size of the magnet is $5 \times 5 \times 1$ mm and it is an NdFeB type. Since the results are similar for the voltage waveforms, only table 5.3 is shown for comparison with table 5.2. The findings are very similar with regards to frequencies, damping factors and the overestimation of voltages. The important point is that the simulation model manages to replicate the changes in these values when a tip mass is added.

Table 5.3: Comparison between simulation and measurement for a beam with tip mass

R_l		ζ_1	ω_1	V_{peak}
10 MΩ	**sim**	0.0148	54.8 Hz	42.7 V
	meas	0.0155	53.4 Hz	25.0 V
120 kΩ	**sim**	0.0476	53.1 Hz	17.3 V
	meas	0.0334	52.5 Hz	8.5 V
500 Ω	**sim**	id.	51.3 Hz	0.15 V
	meas	0.0145	51.8 Hz	0.07 V

Conclusions

In general the simulation model tends to overestimate voltages quite dramatically. The match of frequencies and variation of these under different load resistors is quite good. The same is true for the damping factors, apart

from an overestimation at the impedance matched load of 120 kΩ. As explained, it seems reasonable to assume that the discrepancies come from material parameters rather than the model itself and these are the points where the model can provide helpful qualitative insights:

- Influence of load resistance on the voltage
- Natural frequency of the beam (as a result of beam dimensions and electrical load)
- Influence of the load resistance on the frequency
- Open circuit behaviour
- Frequency components from higher modes
- Influence of an added tip mass

5.2 Model of the Magnetic Interaction Force

Ideally, the actuation should provide a sudden release and an unimpeded free oscillation of the piezoelectric beam. This is more complicated to achieve when using a magnetic coupling instead of fingers or plectra. Akoun and Yonnet show how involved the analytical modelling of the forces between two cuboidal magnets is [234]. An approach for the calculation of forces based on Kelvin's formula is given by Choi et al. [235] and Vokoun et al. describe analytical solutions for cylindrical magnets [236]. However, the most reliable data will be obtained from finite element method simulation as will be shown in this section.

Nevertheless, to understand the interactions, the simple model depicted in figure 5.1 was used as a first approximation. In this diagram, M_t stands for a permanent magnet mounted on the tip of the beam and at the same time for the consequently added tip mass. A second magnet fixed on a proof mass, m_{mag} passes M_t at a constant velocity v_{rel} along the z-direction with a vertical gap d separating them. The variables z_t and z_{mag} describe the z-positions of M_t and m_{mag} respectively. The relevant force is the magnetic force F_{mag} and its component in z-direction, F_{magz}. The magnetic force in equation (5.40) is assumed to follow an inverse square relationship with the distance r_{mag}, separating the magnets. This is the simplest assumption

found in literature [237, 238], and used for example by Cammarano in [239]. The purpose here is to discuss the differences to finite element modelling and to show the discrepancies.

$$F_{mag} = \frac{F_0 d^2}{r_{mag}^2} \tag{5.40}$$

with:

$$r_{mag} = \sqrt{d^2 + (z_{mag} - z_t)^2} \tag{5.41}$$

where F_0 describes the initial magnetic force, when both magnets are horizontally aligned in their zero position, positive values are for an attractive force, negative values for a repulsive force, depending on the polarity of the magnets relative to each other. Trigonometric relationships deliver the following result for the angle of the magnetic force α_{mag}:

$$\begin{aligned} \cos\alpha_{mag} &= \cos\left(\arctan\left(\tfrac{d}{z_{mag}-z_t}\right)\right) && (5.42)\\ &= \frac{1}{\sqrt{1+\left(\frac{d}{z_{mag}-z_t}\right)^2}} && (5.43)\\ &= \frac{1}{\sqrt{\frac{(z_{mag}-z_t)^2+d^2}{(z_{mag}-z_t)^2}}} && (5.44) \end{aligned}$$

This can be used to determine F_{magz} as:

$$\begin{aligned} F_{magz} &= \tfrac{F_0 d^2}{(d^2+(z_{mag}-z_t)^2)} \cdot \tfrac{(z_{mag}-z_t)}{\sqrt{(z_{mag}-z_t)^2+d^2}} && (5.45)\\ &= F_0 d^2 \tfrac{z_{mag}-z_t}{(d^2+(z_{mag}-z_t)^2)^{3/2}} && (5.46) \end{aligned}$$

Although this is a very simple model, it will be shown later that it can at least predict the phenomenological behaviour of the system. Calculating the forces between two magnets is not a trivial problem and the best results are achieved using finite element software. For this purpose, the MagNet package by Infolytica was used to accurately simulate F_{magz} for the two magnets used in the experimental set-up described below. In this case M_t

was a $2 \times 2 \times 1$ mm N35 type magnet and for m_{mag} a $5 \times 5 \times 1$ mm N50 type magnet was used. At first two arrangements were investigated, one with an initial gap $d = 2$ mm and one with $d = 4$ mm.

Furthermore it was found, that these simulation results can be very well approximated by a curve fit with the first derivative of a Gaussian function of the form:

$$g_{fit}(z_{mag} - z_t) = -\frac{A}{C^2}(z_{mag} - z_t)e^{-\frac{(z_{mag}-z_t)^2}{2C^2}} \tag{5.47}$$

where A and C are the parameters of the fit.

Figure 5.13 shows the magnetic force in the z-direction with the inverse square assumption, and the simulation with the fitted curve. It becomes clear that, apart from the general shape of the curve, the basic assumption can not match the accuracy of the simulated results.

5.3 Experimental Set-up

The measurement set-up in figure 5.14 was used to provide a reproducible magnetic excitation of a piezoelectric beam. As mentioned earlier, a small magnet of $2 \times 2 \times 1$ mm was glued to the tip of the beam such that the direction of polarization is parallel to the beam. The secondary magnet ($5 \times 5 \times 1$ mm) was glued on a perspex bar, mounted on a stepper motor. This way, the velocity at which the driving magnet passes the beam tip can be set by changing the distance of the magnet to the axis of rotation and by varying the rotational speed of the stepper motor itself. The beam was clamped and mounted onto an alignment stage, which allowed adjusting the gap between the two magnets. Two different values $d = 2$ mm and $d = 4$ mm were tested for a repulsive and attractive magnet arrangement. The rotational speed of the stepper motor was set to two revolutions per second, i.e. 2 Hz. With the driving magnet mounted at 10 mm from the center of rotation, this results in an approximate passing velocity of the two magnets $v_{rel} = 120$ mm/s - this value was later on used for the simulations as well. The piezoelectric beam is again the same as in the previous section with the parameters listed in table 5.1. The same discussion about the accuracy of the parameters applies and for this set of measurements only a load resistance $R_l = 120$ kΩ was considered.

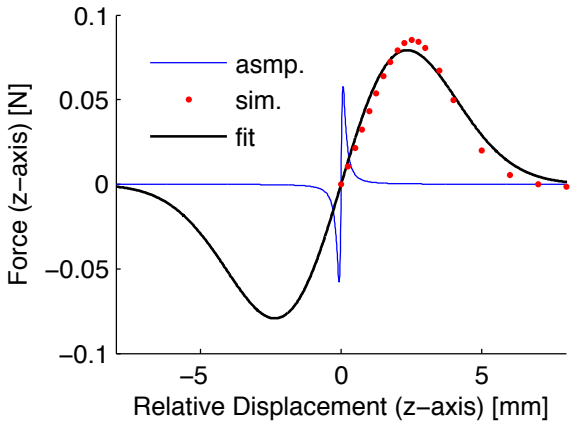

(a)

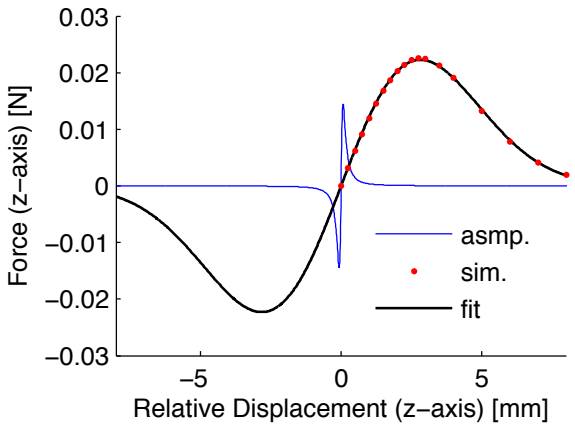

(b)

Figure 5.13: Inverse square assumption and simulated results for the magnetic force in z-direction together with curve fit for a 2 mm gap (a) and a 4 mm gap (b)

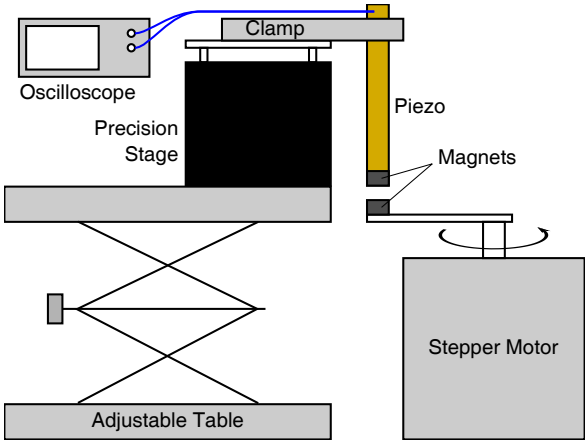

Figure 5.14: Experimental set-up for the validation of the magnetic piezoelectric beam plucking Simulink model

5.4 Model Validation

Figure 5.15 shows the voltage across the 120 kΩ resistor for attracting magnets at 2 Hz excitation and at a gap of 2 mm. Due to the attraction force, the tip of the beam with its magnet initially flicks towards the approaching magnet. After this initial catch, the two magnets stay together while the driving magnet continues its path. During this section, the beam tip oscillates about the driving magnet at an increased frequency, which can be explained by the higher effective stiffness introduced by the driving magnet. Once the beam bending force exceeds the magnetic attraction force, the beam is released and rings down at its natural frequency.

In comparison, figure 5.16 and 5.17 show the simulation results for the same configuration once with the previously introduced finite element simulated magnetic force and once with the inverse square assumption. In addition, plot (b) in each of these figures shows the simulated displacement of the beam tip together with the displacement of the driving magnet, which was defined as a recurring sequence in Matlab/Simulink to replicate the rotating motion of the stepper motor in the experiment. Beam tip position and driving magnet position are used during the simulations to determine the force between the magnets.

The agreement between the experiment and the simulation in figure 5.16 is very good. The absolute values of the voltage are again overestimated but

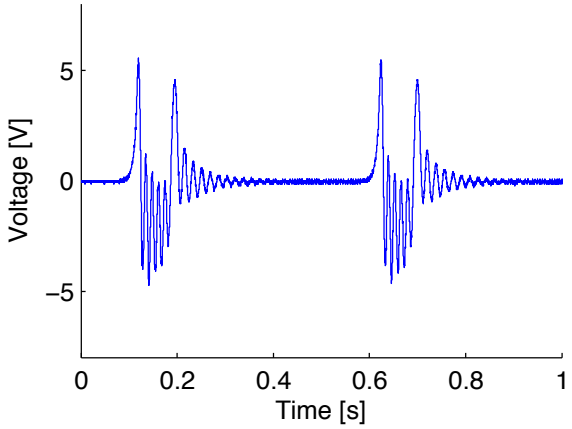

Figure 5.15: Experimental voltage output at 2 mm gap between magnets and 2 Hz actuation frequency for attracting magnets

the catch, combined travel and release phases are accurately represented. In the case with the inverse square assumption, the general phases can still be distinguished, but the number of peaks and the voltages vary slightly.

The next case to discuss is starting from the exact same parameters with the only difference being the orientation of one of the two magnets such that they now repel each other. The corresponding experimental result in figure 5.18 already paints a very different picture. There are no distinct catch and release phases any more, only a slight "bump" in the voltage is seen right at the beginning of an actuation. What happens here is that the approaching driving magnet first pushes the beam tip away until the beam force becomes too large and it snaps through into the opposite direction. The result is a much cleaner ring down of the oscillation and a significantly higher voltage output.

Again, the simulation result for both models of the magnetic force in figures 5.19 and 5.20 show good agreement, reproducing the initial "bump" in voltage and the ring-down well, despite overestimating the absolute voltage. In this case, the inverse square assumption is almost on par with the finite element simulation, which might seem surprising at first. However, the actual oscillation is in this case barely affected by the driving magnet (in contrast to the attractive case, where it introduces a higher frequency oscillation) and is only a result of a transferred impulse and so it makes sense that after the initial release, the voltage outputs differ very little.

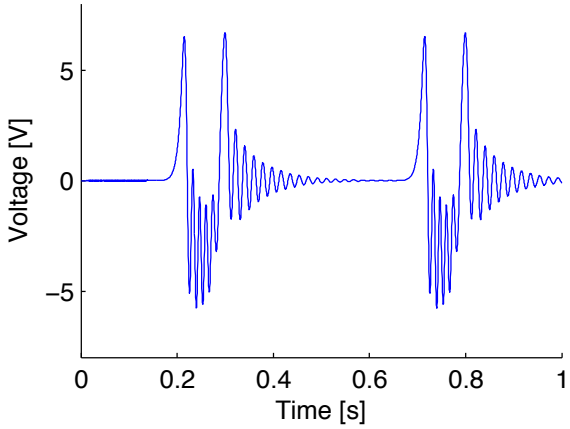

(a)

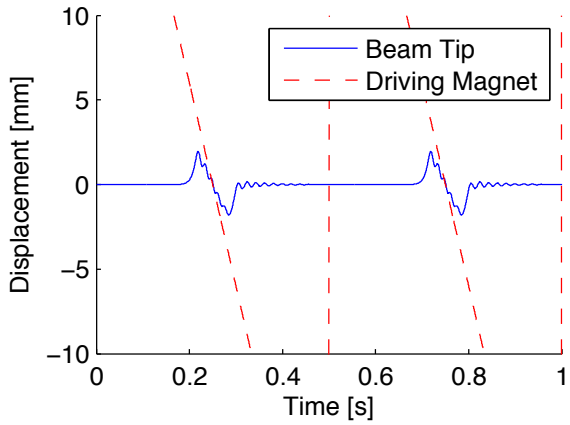

(b)

Figure 5.16: Simulated voltage output (a) and tip displacement (b) at 2 mm gap between magnets and 2 Hz actuation frequency for attracting magnets and with simulated magnetic force

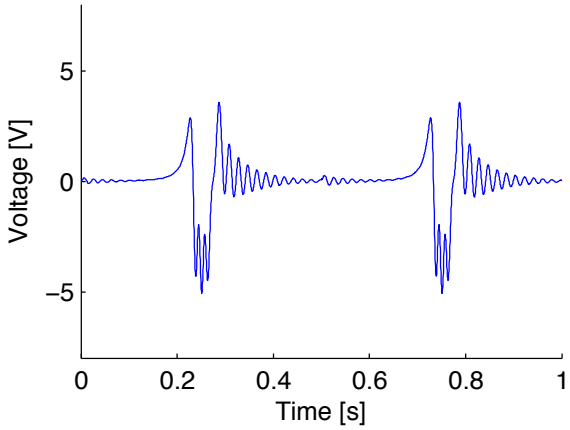

(a)

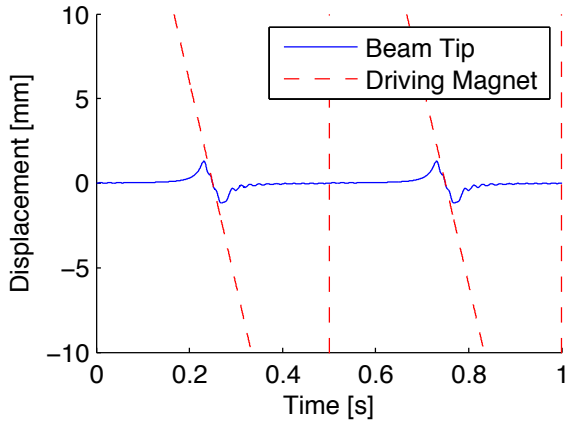

(b)

Figure 5.17: Simulated voltage output (a) and tip displacement (b) at 2 mm gap between magnets and 2 Hz actuation frequency for attracting magnets and with inverse square assumption for the magnetic force

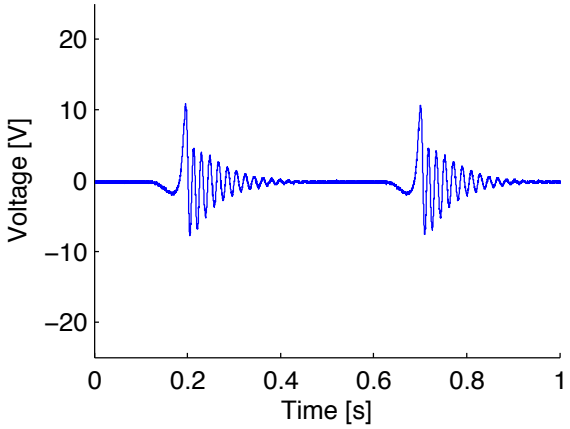

Figure 5.18: Experimental voltage output at 2 mm gap between magnets and 2 Hz actuation frequency for repelling magnets

It can be said that the inverse square assumption for the magnetic force, while only providing a rough estimate, yields reasonable phenomenological agreement with the overall behaviour of the system. This is however only valid because of the nature of this particular case where the results are mainly based on the initial deflection and in general, FEM simulation is preferable.

Finally, figure 5.21 depicts what happens in the experiment if the gap is increased to 4 mm with repelling magnets (again at 2 Hz excitation frequency). The magnetic coupling becomes very weak and the beam tip only experiences a gradual deflection, not exhibiting any oscillation at all and a big drop in voltage is observed. The magnetic force for this scenario was also simulated with MagNet and the curve fit was used for the calculation in figure 5.22. Again, the absolute voltage is overestimated, while the general form of the curve matches the experiment well.

In conclusion, the validity of this simulation model is supported by the comparison with experimental results. It is assumed that the discrepancies in voltage output could be due to either material degradation or combination of the errors of the large number of material parameters that go into the calculation as already discussed in section 5.1.6.

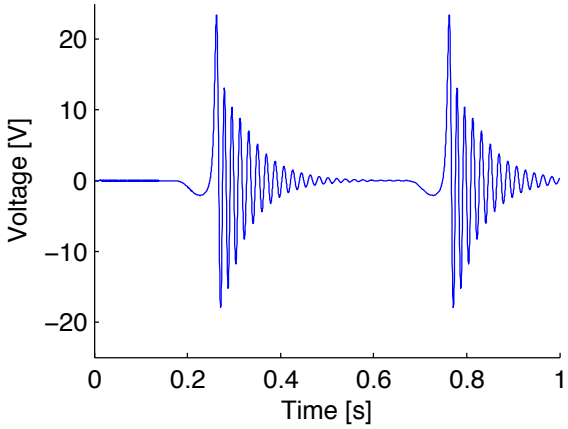

(a)

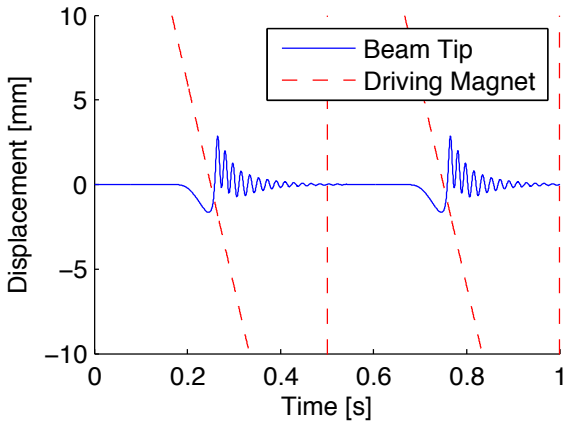

(b)

Figure 5.19: Simulated voltage output (a) and tip displacement (b) at 2 mm gap between magnets and 2 Hz actuation frequency for repelling magnets and with simulated magnetic force

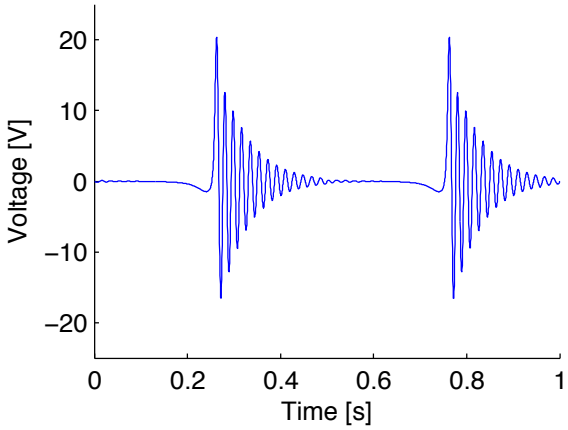

(a)

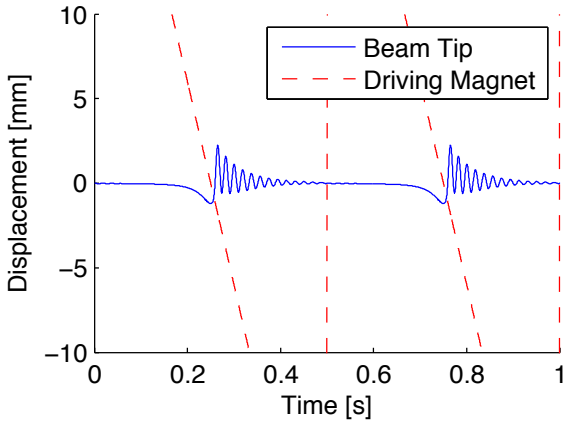

(b)

Figure 5.20: Simulated voltage output (a) and tip displacement (b) at 2 mm gap between magnets and 2 Hz actuation frequency for repelling magnets and with inverse square assumption for the magnetic force

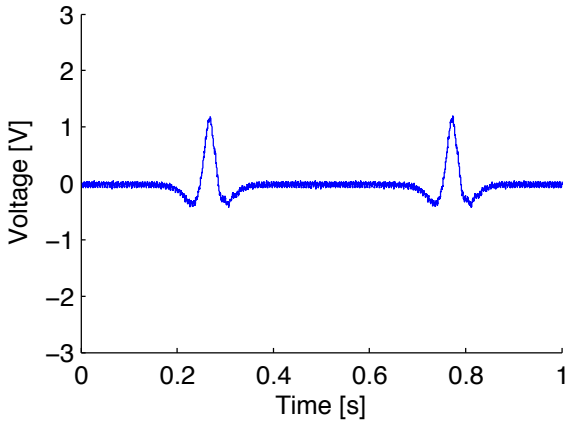

Figure 5.21: Experimental voltage output at 4 mm gap between magnets and 2 Hz actuation frequency for repelling magnets

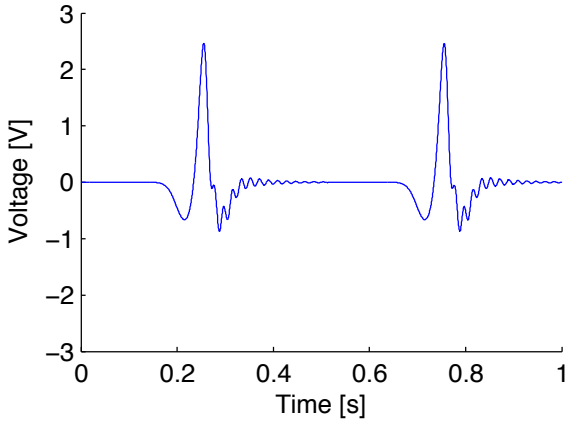

(a)

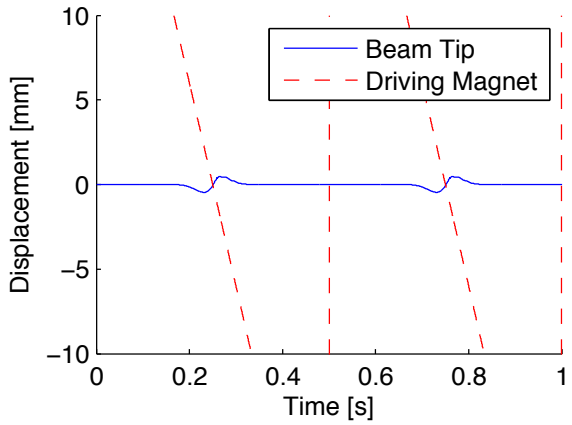

(b)

Figure 5.22: Simulated voltage output (a) and tip displacement (b) at 4 mm gap between magnets and 2 Hz actuation frequency for repelling magnets and with simulated magnetic force

5.5 Further Results

After successfully establishing the model, this section intends to highlight some of the capabilities provided by the simulations. One item of interest is the variation of the gap between the magnets. The example in this work uses fairly large piezoelectric elements with large gaps for ease of experimental set-up. However, the entire model is valid for the micro scale as well and as the overall size and gaps decrease it might be important to select a large gap to avoid collision between the different elements. However, as seen in section 5.4, an increased gap with otherwise similar parameters will dramatically lower the performance. The question is, whether this can be counteracted by using stronger or bigger magnets and to investigate this, the attraction force between two magnets with double the thickness, i.e. $5 \times 5 \times 2$ mm and $2 \times 2 \times 2$ mm was simulated at a gap of 4 mm as can be seen in figure 5.23. The resulting simulated voltage and displacement for repelling magnets at 2 Hz excitation in figure 5.24 is promising. While the shape of the curve fit in figure 5.23 is slightly lower and wider than in figure 5.13, the simulated voltage still shows a clear oscillation after initial deflection.

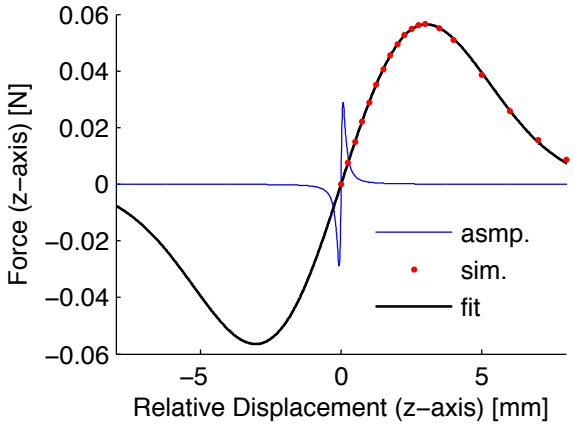

Figure 5.23: Inverse square assumption and simulated results for the magnetic force in z-direction together with curve fit for a 4 mm gap with magnets doubled in thickness

In order to maximize power output in energy harvesting it is necessary to determine the best impedance matched load for the piezoelectric beam. The simulation model allows calculation of RMS voltage and power output

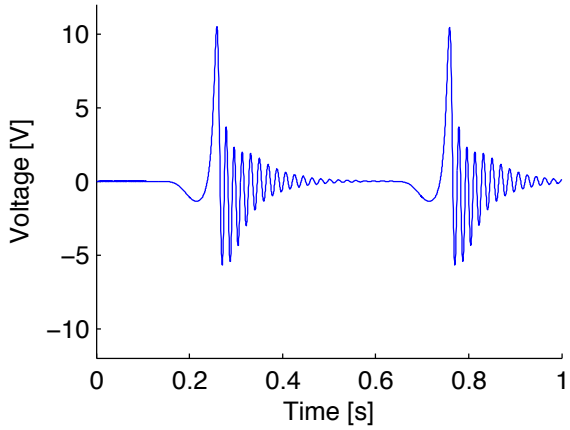

(a)

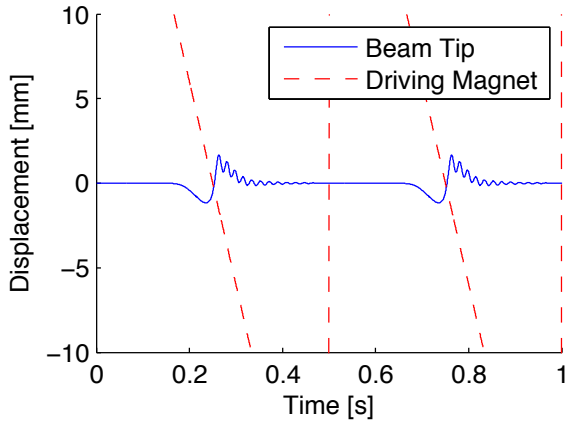

(b)

Figure 5.24: Simulated voltage output (a) and tip displacement (b) at 4 mm gap between magnets and 2 Hz actuation frequency for repelling magnets with double the initial thickness and with simulated magnetic force

across a large range of resistor values very easily and the results are shown in figure 5.25. The graph confirms that for this beam the ideal resistive load for power extraction is close to 120 kΩ.

Figure 5.26 depicts one of the advantages of frequency up-conversion in general. The graphs represent RMS voltage and power output for repelling magnets at 2 mm gap at different driving frequencies. With an increase of driving frequencies, the beam is actuated more often in the same time interval which gives an increase in RMS voltage and power output with frequency and a large operational bandwidth. Two things are worth noting in figure 5.26. First, one can observe that above approximately 4 Hz the curves are not very smooth any longer. This shows the upper limit of operation because in this area, one oscillation has not fully rung down yet before the next actuation happens. Second, if each actuation of the piezoelectric material provides the same amount of energy, then it would be expected that the power output rises linearly with frequency. However, with an increase in frequency, the passing velocity between the two magnets increases as well and the simulation shows that this relative velocity affects the magnitude of the voltage output. As a consequence, the power output rises slightly over proportional with the frequency.

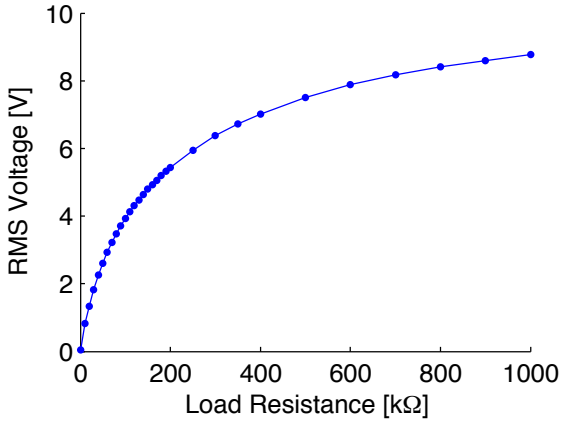

(a)

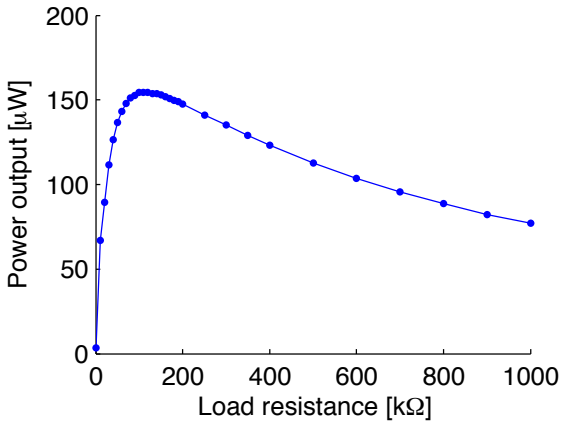

(b)

Figure 5.25: Simulated RMS voltage (a) and average power output (b) as a function of load resistance at 2 mm gap and 2 Hz actuation frequency

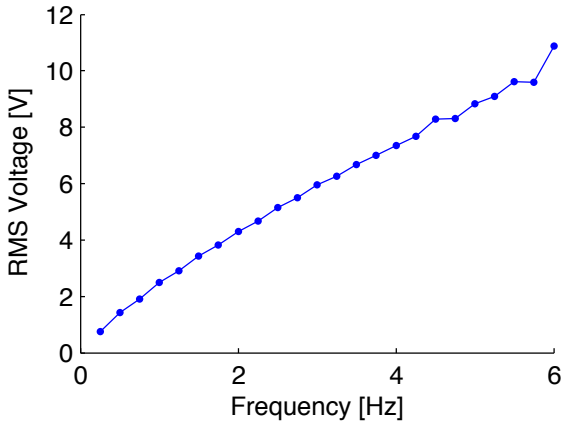

(a)

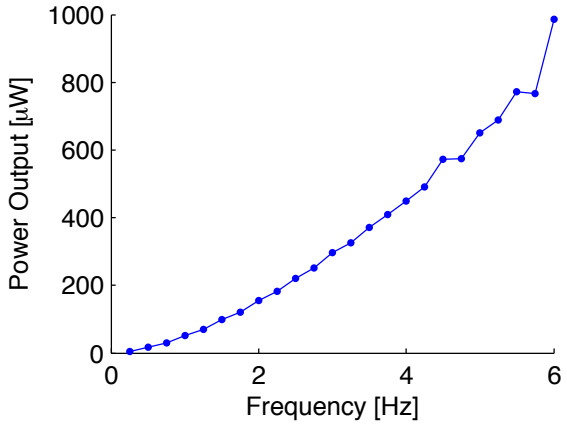

(b)

Figure 5.26: Simulated RMS voltage (a) and average power output (b) as a function of actuation frequency at 2 mm gap

5.6 Conclusions

This chapter presents an experimentally validated calculation model for magnetic actuation of piezoelectric beams with a focus on energy harvesting. First, the relevant equations for the piezoelectric bending beam are derived based on the distributed parameter solution given by Erturk and Inman [119] with omission of base excitation and introducing tip forcing and initial conditions. The procedure to reliably determine the mechanical damping coefficients from an experiment is described. Second, two different methods of incorporating the magnetic interaction forces are presented and discussed. While a simple assumption that the magnetic force is dependent on the inverse of the square of the separation between magnets cannot match the accuracy of a complete finite element simulation, it is nevertheless interesting that the final results are at least phenomenologically valid.

The validity of the entire model is established based on a number of different examples. Two different initial gap sizes as well as attractive and repelling magnet arrangements were investigated and the agreement found to be generally very good.

Some of the further capabilities of the model were explored. It was shown that the use of thicker or stronger magnets can mitigate the adverse effects of an increased gap. This is of particular interest when moving to a smaller scale while still avoiding collision. The model was used to determine the load resistance that provides the highest power output, which is one of the main concerns of energy harvesting. The voltage and power output was also discussed as a function of frequency and the usefulness of frequency up-conversion for increasing bandwidth is supported by the results.

This model can now be used for a first estimation of the power output and system behaviour of new devices that are based on the piezoelectric frequency up-conversion principle.

6 Conclusions

The final chapter summarises the results of this research and highlights the original contributions and novelties. Suggestions for further work and a list of publications arising from this project are given.

6.1 Overview

The starting point of this research is an extensive literature review, giving a brief general overview of the field of energy harvesting and possible applications before focussing on motion generators and highlighting the difficulties for human body applications. Different strategies to overcome these challenges are then discussed.

This work has yielded two different piezoelectric inertial energy harvesters for low frequency random motion based on the frequency up-conversion principle.

The first one is a linear device, operating with a rolling rod, actuating a number of piezoelectric beams. After the initial design, a proof of concept model was built and tested on a rocking platform. The results showed that the principle of frequency up-conversion was successfully implemented, with an operation over a large frequency range and at very low frequencies. A commercial voltage regulation circuit was investigated and discussed. The main drawback of this design for the purpose of human body energy harvesting is that it can only operate in one dimension and is significantly influenced by gravity and thus device orientation.

Following these findings a different approach was pursued in the form of a rotational harvester with an eccentric proof mass. The advantage is that the new design can accept linear as well as rotational excitations and is thus less dependent on gravity. The principle of beam plucking was combined with a different magnetic coupling that allows actuation of the beam without physical impact. This should be beneficial for the longevity of the device.

The first concept model was successful and further developed to arrive at a finalised device the size of a wristwatch that was extensively tested, both in a real world and a laboratory set-up.

After initial investigations on the first prototypes, mathematical models where established for optimisation of the beam plucking via a magnetic coupling. The simulated results were validated with experiments, showing the suitability of the models for future research on the ideal parameters. The modelling supported the conclusion that repelling permanent magnets are advantageous and was used during the design of the piezoelectric bimorph beam for the final device.

6.2 Original Contributions

The primary contributions of this work are on the device side, focussing on some of the main challenges encountered in the field.

The prototype with linear proof mass motion uses an external mass with high density (steel) to magnetically actuate a distributed array of piezoelectric beams. Due to this segmentation and the frequency up-conversion principle the device can operate over a large bandwidth at very low frequencies, while at the same time generating significant voltages due to piezoelectric transduction.

In addition to carrying on the benefits and novelties of the linear device, the rotational prototype introduces further advantages. The application of piezoelectric beam plucking in an inertial rotational device was never done before. The analysis as to why rotational devices are beneficial for human motion is helpful for any further work in this direction and the magnetic coupling for the actuation of the beams has been extensively analysed with resulting design recommendations. In the latter regard, the entire modelling is laid out for future reference to other researchers.

Furthermore, device testing, especially in a harsh real world example of a running race, is rarely done to a similar extent. It is however, in the author's opinion, a crucial component in forging a path for energy harvesting in medical and commercial applications.

6.3 Further Work

In terms of the prototype devices the main research challenges are well covered. Both have successfully proven the principle and comprehensive modelling has been introduced. The main topics on the device side would then be packaging considerations and possible further miniaturisation.

However, with the simulation models in place, further parameters or arrangements of the magnets could be researched. Placing additional magnets on the proof mass of the rotational device could be of interest as a means to adjust the operation bandwidth or to further optimise the power output. The use of multiple beams is a possibility. However, the additional complexity of power extraction from several beams oscillating out of phase might be an issue. An investigation on the reasons why the simulation model tends to dramatically overestimate the generated voltages could also be interesting.

Another area of high interest is the degradation of piezoelectric materials. It was shown during the running tests that the bimorph beams can degrade very rapidly when overstressed. Very little work on long term stability of these materials has been presented. This is a critical point however, if such devices are to be deployed over decades to compete with primary batteries.

The linear excitation table that was developed for the device testing currently runs on software that is limited to trapezoidal velocity profiles. This system can be further enhanced to provide the ability to test random excitation and to ultimately accept accelerometer data from on-body measurements to reproduce human motion in the laboratory.

In a grander scheme, system integration is important. The combination of these harvesters with sensors, power extraction circuitry and intermediate energy storage solutions is what ultimately makes them viable for real applications.

6.4 Publications

Patents

- P. Pillatsch, E. M. Yeatman, and A. S. Holmes, "P54821GB Power Generation Device, filing number 1207987.7," May 2012

Journals

- P. Pillatsch, E. M. Yeatman, and a. S. Holmes, "Magnetic plucking of piezoelectric beams for frequency up-converting energy harvesters," *Smart Materials and Structures*, vol. 23, p. 025009 (12pp), Feb. 2014
- P. Pillatsch, E. M. Yeatman, and A. S. Holmes, "A piezoelectric frequency up-converting energy harvester with rotating proof mass for human body applications," *Sensors and Actuators A: Physical*, vol. 206, pp. 178–185, Oct. 2013
- L. M. Miller, P. Pillatsch, E. Halvorsen, P. K. Wright, E. M. Yeatman, and A. S. Holmes, "Experimental passive self-tuning behavior of a beam resonator with sliding proof mass," *Journal of Sound and Vibration*, vol. 332, pp. 7142–7152, Dec. 2013
- P. Pillatsch, E. M. Yeatman, and A. S. Holmes, "A scalable piezoelectric impulse-excited energy harvester for human body excitation," *Smart Materials and Structures*, vol. 21, p. 115018 (9pp), Nov. 2012

Conferences

- P. Pillatsch, L. M. Miller, E. Halvorsen, P. K. Wright, E. M. Yeatman, and a. S. Holmes, "Self-tuning behavior of a clamped-clamped beam with sliding proof mass for broadband energy harvesting," *Journal of Physics: Conference Series*, vol. 476, p. 012068 (5pp), Dec. 2013
- P. Pillatsch, E. M. Yeatman, and a. S. Holmes, "Real World Testing Of A Piezoelectric Rotational Energy Harvester For Human Motion," *Journal of Physics: Conference Series*, vol. 476, p. 012010 (5pp), Dec. 2013
- P. Pillatsch, E. M. Yeatman, and A. S. Holmes, "A Model For Magnetic Plucking Of Piezoelectric Beams In Energy Harvesters," in *The 17th International Conference on Solid-State Sensors, Actuators and Microsystems, Transducers*, pp. 1364–1367, 2013
- P. Pillatsch, E. M. Yeatman, and A. S. Holmes, "A Wearable Piezoelectric Rotational Energy Harvester," in *Tenth Int. Conf. on Wearable and Implantable Body Sensor Networks*, pp. 1–6, 2013

- P. Pillatsch, E. M. Yeatman, and A. S. Holmes, "Magnetic Beam Plucking In A Piezoelectric Energy Harvester With Rotating Proof Mass," in *PowerMEMS*, pp. 476–479, 2012
- P. Pillatsch, E. M. Yeatman, and A. S. Holmes, "Piezoelectric Rotational Energy Harvester for Body Sensors Using an Oscillating Mass," in *Ninth Int. Conf. on Wearable and Implantable Body Sensor Networks*, pp. 6–10, 2012
- P. Pillatsch, E. M. Yeatman, and A. S. Holmes, "A scalable piezoelectric impulse-excited generator for random low frequency excitation," in *IEEE MEMS*, vol. 21, pp. 1205–1208, Nov. 2012
- P. Pillatsch, E. M. Yeatman, and A. S. Holmes, "Piezoelectric impulse-excited generator for low frequency non-harmonic vibrations," in *PowerMEMS*, pp. 1–4, 2011

Bibliography

[1] J. Bryzek, S. Roundy, B. Bircumshaw, C. Chung, K. Castellino, J. R. Stetter, and M. Vestel, "Marvelous MEMS," *IEEE Circuits and Devices*, 2006.

[2] R. Das, "Wireless Sensor Networks : Overcoming the Challenges to Reach $ 2 Billion in 2021," tech. rep., 2011.

[3] P. D. Mitcheson, E. M. Yeatman, G. K. Rao, A. S. Holmes, and T. C. Green, "Energy Harvesting from Human and Machine Motion for Wireless Electronic Devices," in *Proc. of the IEEE*, vol. 96, pp. 1457–1486, 2008.

[4] A. Denisov and E. Yeatman, "Ultrasonic vs . Inductive Power Delivery for Miniature Biomedical Implants," in *Body Sensor Networks*, pp. 2–7, 2010.

[5] WHO, "Controlling the global obesity epidemic."

[6] BBC, "Dead soldiers in Powys served with Territorial Army."

[7] Seiko Corp., "PARTS CATALOGUE / TECHNICAL GUIDE Cal. 5M62A, 5M63A."

[8] E. M. Yeatman, "Energy harvesting from motion using rotating and gyroscopic proof masses," *Journal of Mech. Eng. Science*, vol. 222, pp. 27–36, Jan. 2008.

[9] J. Boland, *Micro Electret Power Generators*. PhD thesis, 2005.

[10] J. Kwong, "Microwatt Electronics and Beyond," in *PowerMEMS*, vol. 77, pp. 92–96, 2012.

[11] S. Sridhara and M. DiRenzo, "Microwatt embedded processor platform for medical system-on-chip applications," *IEEE Journal of Solid-State Circuits*, vol. 46, no. 4, pp. 721–730, 2011.

[12] A. Paidimarri and P. Nadeau, "A 440pJ/bit 1Mb/s 2.4 GHz multi-channel FBAR-based TX and an integrated pulse-shaping PA," in *Symposium on VLSI Circuits*, pp. 34–35, 2012.

[13] L. Logesparan, A. J. Casson, and E. Rodriguez-Villegas, "Optimal features for online seizure detection.," *Medical & biological engineering & computing*, vol. 50, pp. 659–69, July 2012.

[14] T. Torfs, V. Leonov, R. F. Yazicioglu, P. Merken, C. Van Hoof, R. J. Vullers, and B. Gyselinckx, "Wearable Autonomous Wireless Electroencephalography System Fully Powered by Human Body Heat," in *2008 IEEE Sensors*, pp. 1269–1272, IEEE, Oct. 2008.

[15] X. Liu, Y. Zheng, M. W. Phyu, F. N. Endru, V. Navaneethan, and B. Zhao, "An Ultra-Low Power ECG Acquisition and Monitoring ASIC System for WBAN Applications," *IEEE Journal on Emerging and Selected Topics in Circuits and Systems*, vol. 2, pp. 60–70, Mar. 2012.

[16] A. P. Chandrakasan, N. Verma, and D. C. Daly, "Ultralow-power electronics for biomedical applications.," *Annual review of biomedical engineering*, vol. 10, pp. 247–74, Jan. 2008.

[17] D. Young, P. Cong, and W. Ko, "Wireless batteryless less-invasive blood pressure sensing microsystem for advanced biomedical application," in *2010 IEEE 23rd International Conference on Micro Electro Mechanical Systems (MEMS)*, pp. 31–34, 2010.

[18] E. Y. Chow, A. L. Chlebowski, S. Chakraborty, W. J. Chappell, and P. P. Irazoqui, "Fully wireless implantable cardiovascular pressure monitor integrated with a medical stent," *IEEE transactions on bio-medical engineering*, vol. 57, pp. 1487–96, June 2010.

[19] C. Hierold, B. Clasbrumme, D. Behrend, T. Scheiter, M. Steger, K. Oppermann, H. Kapels, E. Landgraf, D. Wenzel, and D. Etuodt, "Implantable low power integrated pressure sensor system for minimal invasive telemetric patient monitoring," in *Proceedings MEMS 98. IEEE. Eleventh Annual International Workshop on Micro Electro Mechanical Systems*, pp. 568–573, IEEE, 1998.

[20] H. Fassbender, W. Mokwa, M. Gortz, K. Trieu, U. Urban, T. Schmitz-Rode, T. Gottsche, and P. Osypka, "Fully implantable blood pressure sensor for hypertonic patients," *2008 IEEE Sensors*, pp. 1226–1229, Oct. 2008.

[21] P. Osypka, K. Trieu, H. Fassbender, W. Mokwa, U. Urban, T. Hilbel, R. Becker, W. Coenen, and R. Glocker, "HYPER-IMS: A Fully Implantable Blood Pressure Sensor for Hypertensive Patients," in *Sensor+Test*, vol. 7, pp. 145–149, 2009.

[22] M. Allen, "Micromachined Endovascularly-Implantable Wireless Aneurysm Pressure Sensors: From Concept To Clinic," in *TRANSDUCERS '05.*, pp. 275–278, IEEE, 2005.

[23] P. Bingger, J. Fiala, A. Seifert, N. Weber, K. Foerster, C. Heilmann, F. Beyersdorf, P. Woias, and H. Zappe, "In vivo monitoring of blood oxygenation using an implantable MEMS-based sensor," *2010 IEEE 23rd International Conference on Micro Electro Mechanical Systems (MEMS)*, pp. 1031–1034, Jan. 2010.

[24] R. Bashirullah, "Wireless Implants," *IEEE Microwave Magazine*, vol. 11, pp. S14–S23, Dec. 2010.

[25] M. Sawan, Y. Hu, and J. Coulombe, "Wireless Smart Implants Dedicated to Multichannel Monitoring and Microstimulation," *IEEE Circuits and Systems*, pp. 21–39, 2005.

[26] M. Yuce, T. Dissanayake, and H. Keong, "Wireless telemetry for electronic pill technology," *IEEE Sensors*, 2009.

[27] C. Sauer, M. Stanacevic, G. Cauwenberghs, and N. Thakor, "Power Harvesting and Telemetry in CMOS for Implanted Devices," *IEEE Transactions on Circuits and Systems - 1*, vol. 52, no. 12, pp. 2605–2613, 2005.

[28] Q. Huang and M. Oberle, "A 0.5-mW passive telemetry IC for biomedical applications," *IEEE Journal of Solid-State Circuits*, vol. 33, pp. 937–946, July 1998.

[29] X.-F. Teng, Y.-T. Zhang, C. C. Y. Poon, and P. Bonato, "Wearable Medical Systems for p-Health," *IEEE Reviews in Biomedical Engineering*, vol. 1, pp. 62–74, 2008.

[30] M. Caldara, C. Colleoni, E. Guido, G. Rosace, V. Re, and A. Vitali, "A wearable sensor platform to monitor sweat pH and skin temperature," *2013 IEEE International Conference on Body Sensor Networks*, pp. 1–6, May 2013.

[31] V. F. Curto, N. Angelov, S. Coyle, R. Byrne, S. Hughes, N. Moyna, D. Diamond, and F. Benito Lopez, "My Sweat my Health: Real Time Sweat Analysis Using Wearable Micro-fluidic Devices," in *Proceedings of the 5th International ICST Conference on Pervasive Computing Technologies for Healthcare*, pp. 196–197, IEEE, 2011.

[32] D. S. Moran, A. Shitzer, K. B. Pandolf, M. Kuennen, T. Gillum, K. Dokladny, E. Bedrick, S. Schneider, V. Miller, G. Bates, J. D. Schneider, J. Thomsen, A. O. Hyg, M. F. Bergeron, M. D. Laird, E. L. Marinik, J. S. Brenner, J. L. Waller, V. S. Miller, and G. P. Bates, "A physiological strain index to evaluate heat stress," *Am. J. Physiol. Regul. Integr. Comp. Physiol*, no. 275, pp. 129–134, 1998.

[33] W. J. Tharion, A. W. Potter, C. M. Clements, A. J. Karis, M. J. Buller, and R. W. Hoyt, "Real-Time Physiological Monitoring of Soldiers Encapsulated in Chemical-Biological Clothing," in *2013 IEEE International Conference on Body Sensor Networks*, 2013.

[34] Y.-S. Lin, D. Sylvester, and D. Blaauw, "An ultra low power 1V, 220nW temperature sensor for passive wireless applications," *2008 IEEE Custom Integrated Circuits Conference*, pp. 507–510, Sept. 2008.

[35] R. A. Croce Jr., S. Vaddiraju, A. Legassey, Y. Wang, and D. Burgess, "A Low Power Miniaturized CMOS-Based Continuous Glucose Monitoring System," in *2013 IEEE International Conference on Body Sensor Networks*, pp. 13–16, 2013.

[36] B. D. McKean and D. A. Gough, "A telemetry-instrumentation system for chronically implanted glucose and oxygen sensors," *IEEE transactions on bio-medical engineering*, vol. 35, pp. 526–32, July 1988.

[37] R. P. Feynman, "There's Plenty of Room at the Bottom," *Journal of Microelectromechanical Systems*, vol. 1, no. 1, pp. 60–66, 1992.

[38] A. Lodder, M. V. Kamath, A. R. Upton, and D. Armstrong, "Evaluation of the Efficacy and Performance of Medical Implants: A Review," *Journal of Long-Term Effects of Medical Implants*, vol. 20, no. 3, pp. 173–185, 2010.

[39] World Health Organization, "MEDICAL DEVICE REGULATIONS," tech. rep., 2003.

[40] W. H. Maisel, "Medicine and Public Issues Medical Device Regulation: An Introduction for the Practicing Physician," *Ann. Intern. Med.*, vol. 140, pp. 296–302, 2004.

[41] W. H. Maisel, "Safety Issues Involving Medical Devices," *Journal of the American Medical Association*, vol. 294, no. 8, pp. 955–958, 2005.

[42] W. H. Maisel, M. Moynahan, B. D. Zuckerman, T. P. Gross, O. H. Tovar, D.-b. Tillman, and D. B. Schultz, "Pacemaker and ICD Generator Malfunctions - Analysis of Food and Drug Administration Annual Reports," *Journal of the American Medical Association*, vol. 295, no. 16, pp. 1901–1906, 2006.

[43] A. P. Chandrakasan, D. C. Daly, J. Kwong, and Y. K. Ramadass, "Next generation micro-power systems," in *2008 IEEE Symposium on VLSI Circuits*, pp. 2–5, IEEE, June 2008.

[44] E. Romero, R. O. Warrington, and M. R. Neuman, "Energy scavenging sources for biomedical sensors.," *Physiological Measurement*, vol. 30, pp. R35–62, Sept. 2009.

[45] S. Roundy, E. Leland, J. Baker, E. Carleton, E. Reilly, E. Lai, B. Otis, J. Rabaey, V. Sundararajan, and P. Wright, "Improving Power Output for Vibration-Based Energy Scavengers," *IEEE Pervasive Computing*, vol. 4, pp. 28–36, Jan. 2005.

[46] "http://www.micropelt.com."

[47] V. Leonov, C. V. Hoof, and R. J. Vullers, "Thermoelectric and Hybrid Generators in Wearable Devices and Clothes," in *2009 Sixth International Workshop on Wearable and Implantable Body Sensor Networks*, pp. 195–200, IEEE, June 2009.

[48] V. Leonov and P. Fiorini, "Thermal Matching of a Thermoelectric Energy Scavenger with the Ambience," in *5th European Conference on Thermoelectrics*, pp. 1–5, 2007.

[49] C. Watkins, B. Shen, and R. Venkatasubramanian, "Low-grade-heat energy harvesting using superlattice thermoelectrics for applications in implantable medical devices and sensors," *ICT 2005. 24th International Conference on Thermoelectrics*, pp. 265–267, 2005.

[50] Y. K. Ramadass and A. P. Chandrakasan, "A Batteryless Thermoelectric Energy-Harvesting Interface Circuit with 35mV Startup Voltage," in *ISSCC*, pp. 296–297, 2010.

[51] P. D. Mitcheson, "Energy harvesting for human wearable and implantable bio-sensors," *Annual International Conference of the IEEE Engineering in Medicine and Biology Society*, vol. 1, pp. 3432–3436, Jan. 2010.

[52] H. J. Visser and R. J. M. Vullers, "RF Energy Harvesting and Transport for Wireless Sensor Network Applications: Principles and Requirements," *Proceedings of the IEEE*, vol. 101, pp. 1410–1423, June 2013.

[53] M. Piñuela and P. D. Mitcheson, "Ambient RF Energy Harvesting in Urban and Semi-Urban Environments," *IEEE Transactions On Microwave Theory And Techniques*, vol. 61, no. 7, pp. 2715–2726, 2013.

[54] H. Nishimoto, Y. Kawahara, and T. Asami, "Prototype implementation of ambient RF energy harvesting wireless sensor networks," in *2010 IEEE Sensors*, pp. 1282–1287, IEEE, Nov. 2010.

[55] S. Meninger, J. Mur-Miranda, R. Amirtharajah, A. Chandrakasan, and J. Lang, "Vibration-to-electric energy conversion," *IEEE Transactions on Very Large Scale Integration (VLSI) Systems*, vol. 9, no. 1, pp. 64–76, 2001.

[56] L. A. Weinstein, M. R. Cacan, P. M. So, and P. K. Wright, "Vortex shedding induced energy harvesting from piezoelectric materials in heating, ventilation and air conditioning flows," *Smart Materials and Structures*, vol. 21, p. 045003, Apr. 2012.

[57] K. Kim, D. Choi, and Y. Seo, "Piezoelectric Energy Harvester Using Flow-Induced Vibration," in *PowerMEMS*, pp. 197–200, 2008.

[58] I.-H. Kim, S.-J. Jang, and H.-J. Jung, "Performance enhancement of a rotational energy harvester utilizing wind-induced vibration of an inclined stay cable," *Smart Materials and Structures*, vol. 22, p. 075004, July 2013.

[59] K. Cunefare, E. Skow, and A. Erturk, "Energy harvesting from hydraulic pressure fluctuations," *Smart Materials and Structures*, vol. 025036 (10, 2013.

[60] M. Pozzi and M. Zhu, "Pizzicato excitation for wearable energy harvesters," *SPIE Newsroom*, pp. 3–5, June 2011.

[61] S. Almouahed, M. Gouriou, C. Hamitouche, E. Stindel, and C. Roux, "The Use of Piezoceramics As Electrical Energy Harvesters Within Instrumented Knee Implant During Walking," *IEEE/ASME Transactions on Mechatronics*, vol. 16, no. 5, pp. 799–807, 2011.

[62] P. D. Mitcheson, *Analysis and Optimisation of Energy-Harvesting Micro-Generator Systems*. PhD thesis, 2005.

[63] B. Li, J. H. You, and Y.-J. Kim, "Low frequency acoustic energy harvesting using PZT piezoelectric plates in a straight tube resonator," *Smart Materials and Structures*, vol. 22, p. 055013, May 2013.

[64] "http://www.perpetuum.com."

[65] "www.enocean.com."

[66] V. Oncescu and D. Erickson, "High volumetric power density, non-enzymatic, glucose fuel cells.," *Scientific Reports*, vol. 3, p. 1226, Jan. 2013.

[67] C. He, M. E. Kiziroglou, D. C. Yates, and E. M. Yeatman, "MEMS energy harvester for wireless biosensors," *2010 IEEE 23rd International Conference on Micro Electro Mechanical Systems (MEMS)*, pp. 172–175, Jan. 2010.

[68] S. Bandyopadhyay and A. P. Chandrakasan, "Platform Architecture for Solar, Thermal, and Vibration Energy Combining With MPPT and Single Inductor," *IEEE Journal of Solid-State Circuits*, vol. 47, no. 9, pp. 1–17, 2012.

[69] E. K. Reilly, F. Burghardt, R. Fain, and P. Wright, "Powering a wireless sensor node with a vibration-driven piezoelectric energy harvester," *Smart Materials and Structures*, vol. 20, p. 125006, Dec. 2011.

[70] R. Amirtharajah and A. P. Chandrakasan, "Self-Powered Signal Processing Using Vibration-Based Power Generation," *IEEE Journal of Solid-State Circuits*, vol. 33, no. 5, pp. 687–695, 1998.

[71] R. Amirtharajah, S. Meninger, J. O. Mur-miranda, A. Chandrakasan, and J. Lang, "A Micropower Programmable DSP Powered using a MEMS-based Vibration-to-Electric Energy Converter," in *IEEE International Solid-State Circuits Conference*, pp. 8–10, 2000.

[72] T. Zaitsu, O. Ohnishi, T. Inoue, M. Shoyama, T. Ninomiya, F. C. Lee, and G. C. Hua, "Piezoelectric Transformer operating in Thickness Extensional Vibration and Its Application to Switching Converter," in *25th Annual IEEE Power Electronics Specialists Conference, PESC '94 Record*, pp. 585–589, 1994.

[73] M. Goldfarb and L. D. Jones, "On the Efficiency of Electric Power Generation With Piezoelectric Ceramic," *Journal of Dynamic Systems, Measurement and Control*, vol. 121, pp. 566–571, 1999.

[74] M. Umeda, K. Nakamura, and S. Ueha, "Analysis of the Transformation of Mechanical Impact Energy to Electric Energy Using Piezoelectric Vibrator," *Jpn. J. Appl. Phys*, vol. 35, pp. 3267–3273, 1996.

[75] M. Umeda, K. Nakamura, and S. Ueha, "Energy Storage Characteristics of a Piezo-Generator using Impact Induced Vibration," *Jpn. J. Appl. Phys*, vol. 36, pp. 3146–3151, 1997.

[76] T. Starner, "Human-powered wearable computing," *IBM Systems Journal*, vol. 35, pp. 1–12, 1996.

[77] J. Kymissis, C. Kendall, J. Paradiso, and N. Gershenfeld, "Parasitic power harvesting in shoes," *Digest of Papers. Second International Symposium on Wearable Computers (Cat. No.98EX215)*, pp. 132–139, 1998.

[78] N. S. Shenck, *A Demonstration of Useful Electric Energy Generation from Piezoceramics in a Shoe*. PhD thesis, 1997.

[79] P. Smalser, "Power Transfer Of Piezoelectric Generated Energy," 1997.

[80] M. Kimura, "Piezo-Electricity Generation Device," 1998.

[81] S. P. Beeby, M. J. Tudor, and N. M. White, "Energy harvesting vibration sources for microsystems applications," *Measurement Science and Technology*, vol. 17, pp. R175–R195, Dec. 2006.

[82] J. Paradiso and T. Starner, "Energy scavenging for mobile and wireless electronics," *Pervasive Computing, IEEE*, 2005.

[83] K. A. Cook-Chennault, N. Thambi, and A. M. Sastry, "Powering MEMS portable devices - a review of non-regenerative and regenerative power supply systems with special emphasis on piezoelectric energy harvesting systems," *Smart Materials and Structures*, vol. 17, p. 043001 (33pp), Aug. 2008.

[84] S.-G. Kim, S. Priya, and I. Kanno, "Piezoelectric MEMS for energy harvesting," *MRS Bulletin*, vol. 37, pp. 1039–1050, Nov. 2012.

[85] N. E. Dutoit, B. L. Wardle, and S.-G. Kim, "Design Considerations for Mems-Scale Piezoelectric Mechanical Vibration Energy Harvesters," *Integrated Ferroelectrics*, vol. 71, pp. 121–160, July 2005.

[86] S. Roundy, P. K. Wright, and J. Rabaey, "A study of low level vibrations as a power source for wireless sensor nodes," *Computer Communications*, vol. 26, pp. 1131–1144, July 2003.

[87] P. D. Mitcheson, E. K. Reilly, T. Toh, P. K. Wright, and E. M. Yeatman, "Performance limits of the three MEMS inertial energy generator transduction types," *Journal of Micromechanics and Microengineering*, vol. 17, pp. S211–S216, Sept. 2007.

[88] P. D. Mitcheson, T. C. Green, A. S. Holmes, and E. M. Yeatman, "Architectures for Vibration-Driven Micropower Generators," *Journal of Microelectromechanical Systems*, vol. 13, pp. 429–440, June 2004.

[89] T. von Büren, P. D. Mitcheson, T. C. Green, E. M. Yeatman, A. S. Holmes, and G. Tröster, "Optimization of Inertial Micropower Generators for Human Walking Motion," *IEEE Sensors Journal*, vol. 6, no. 1, pp. 28–38, 2006.

[90] J. Yun, S. N. Patel, M. S. Reynolds, and G. D. Abowd, "Design and Performance of an Optimal Inertial Power Harvester for Human-powered Devices," *IEEE Transactions on Mobile Computing*, vol. 8, no. 7, pp. 1–16, 2010.

[91] E. Romero, R. O. Warrington, and M. R. Neuman, "Body motion for powering biomedical devices," in *Conf. proc. : Annual Int. Conf. IEEE Engineering in Medicine and Biology Society.*, pp. 2752–5, Jan. 2009.

[92] P. Miao, P. D. Mitcheson, A. S. Holmes, E. M. Yeatman, T. C. Green, and B. H. Stark, "MEMS Inertial Power Generators For Biomedical Applications," in *DTIP of MEMS & MOEMS*, vol. 12, pp. 1–3, Apr. 2005.

[93] T. T. Toh, P. D. Mitcheson, A. S. Holmes, and E. M. Yeatman, "A continuously rotating energy harvester with maximum power point tracking," *Journal of Micromechanics and Microengineering*, vol. 18, p. 104008 (7pp), Oct. 2008.

[94] T. Krupenkin and J. A. Taylor, "Reverse electrowetting as a new approach to high-power energy harvesting," *Nature Communications*, vol. 2, p. 448, Aug. 2011.

[95] C. Saha, T. O'Donnell, H. Loder, S. Beeby, and J. Tudor, "Optimization of an Electromagnetic Energy Harvesting Device," *IEEE Transactions on Magnetics*, vol. 42, pp. 3509–3511, Oct. 2006.

[96] C. Williams, C. Shearwood, M. Harradine, P. Mellor, T. Birch, and R. Yates, "Development of an electromagnetic micro-generator," *IEE Proceedings - Circuits, Devices and Systems*, vol. 148, no. 6, p. 337, 2001.

[97] X. Y. Wang, S. Palagummi, L. Liu, and F. G. Yuan, "A magnetically levitated vibration energy harvester," *Smart Materials and Structures*, vol. 22, p. 055016 (10pp), May 2013.

[98] R. D. Prabha, D. Kwon, O. Lazaro, K. D. Peterson, and G. A. Rincón-mora, "Increasing Electrical Damping in Energy-Harnessing Transducers," *IEEE Transactions on Circuits and Systems*, vol. 58, no. 12, pp. 787–791, 2011.

[99] P. Miao, A. S. Holmes, E. M. Yeatman, T. C. Green, and P. D. Mitcheson, "Micro-Machined Variable Capacitors for Power Generation," *Electrostatics*, vol. 178, pp. 53–58, 2003.

[100] T. Galchev, R. Raz, and O. Paul, "An Electrostatic Springless Inertial Harvester For Converting Multi-Dimensional Low-Frequency Motion," in *IEEE Conf. on MEMS*, pp. 102–105, 2013.

[101] M. Kiziroglou, "Rolling rod electrostatic microgenerator," *Industrial Electronics, IEEE*, vol. 56, no. 4, pp. 1101–1108, 2009.

[102] C. He, *Electrostatic Micro Energy Harvester with Rolling Mass*. PhD thesis, 2010.

[103] Y. Suzuki, M. Edamoto, N. Kasagi, K. Kashiwagi, and Y. Morizawa, "Micro power generator with high-performace polymer electret," in *2008 13th International Symposium on Electrets*, pp. B1204–B1204, IEEE, Sept. 2008.

[104] T. Tsutsumino, Y. Suzuki, N. Kasagi, and Y. Sakane, "Seismic Power Generator Using High-Performance Polymer Electret," in *19th IEEE International Conference on Micro Electro Mechanical Systems*, pp. 98–101, IEEE, 2006.

[105] "IEEE Standard on Piezoelectricity," tech. rep., IEEE, 1988.

[106] M. Ferrari, V. Ferrari, M. Guizzetti, and D. Marioli, "An autonomous battery-less sensor module powered by piezoelectric energy harvesting with RF transmission of multiple measurement signals," *Smart Materials and Structures*, vol. 18, p. 085023 (9pp), Aug. 2009.

[107] J. D. Hobeck and D. J. Inman, "Artificial piezoelectric grass for energy harvesting from turbulence-induced vibration," *Smart Materials and Structures*, vol. 21, p. 105024 (10pp), Oct. 2012.

[108] B. Y. Lee, J. Zhang, C. Zueger, W.-J. Chung, S. Y. Yoo, E. Wang, J. Meyer, R. Ramesh, and S.-W. Lee, "Virus-based piezoelectric energy generation," *Nature Nanotechnology*, pp. 1–6, May 2012.

[109] G. D. Pasquale, G. Di Pasquale, S. Graziani, F. Pagano, and E. Umana, "All Polymeric Transducers for Energy Harvesting," in *IEEE Sensors*, pp. 837–840, IEEE, Nov. 2010.

[110] R. V. Schaijk, R. Elfrink, T. M. Kamel, and M. Goedbloed, "Piezoelectric AlN energy harvesters for wireless autonomous transducer solutions," in *Sensors*, pp. 45–48, 2008.

[111] M. Ataur Rahman, B.-C. Lee, D.-T. Phan, and G.-S. Chung, "Fabrication and characterization of highly efficient flexible energy harvesters using PVDF graphene nanocomposites," *Smart Materials and Structures*, vol. 22, p. 085017 (10pp), Aug. 2013.

[112] R. Tiwari and K. J. Kim, "IPMC as a mechanoelectric energy harvester: tailored properties," *Smart Materials and Structures*, vol. 22, p. 015017, Jan. 2013.

[113] E. K. Reilly and P. K. Wright, "Modeling, fabrication and stress compensation of an epitaxial thin film piezoelectric microscale energy scavenging device," *Journal of Micromechanics and Microengineering*, vol. 19, p. 095014 (11pp), Sept. 2009.

[114] S.-C. Lin and W.-J. Wu, "Piezoelectric micro energy harvesters based on stainless-steel substrates," *Smart Materials and Structures*, vol. 22, p. 045016 (11pp), Apr. 2013.

[115] D. Zhu, N. White, N. Harris, J. Tudor, R. Torah, A. Almusallam, and S. Beeby, "Screen printed piezoelectric films for energy harvesting," *Advances in Applied Ceramics*, pp. 1–6, 2012.

[116] Linear Technology, "LTC3588-1 - Piezoelectric Energy Harvesting Power Supply," 2011.

[117] S. Roundy and P. K. Wright, "A piezoelectric vibration based generator for wireless electronics," *Smart Materials and Structures*, vol. 13, pp. 1131–1142, Oct. 2004.

[118] "http://commons.wikimedia.org/wiki/File:Perovskite.svg."

[119] A. Erturk and D. J. Inman, *Piezoelectric Energy Harvesting*. Wiley, 2011.

[120] L. Miller, P. Wright, C. Ho, J. Evans, P. Shafer, and R. Ramesh, "Integration of a low frequency, tunable MEMS piezoelectric energy harvester and a thick film micro capacitor as a power supply system for wireless sensor nodes," *2009 IEEE Energy Conversion Congress and Exposition*, pp. 2627–2634, Sept. 2009.

[121] L. M. Miller, E. Halvorsen, T. Dong, and P. K. Wright, "Modeling and experimental verification of low-frequency MEMS energy harvesting from ambient vibrations," *Journal of Micromechanics and Microengineering*, vol. 21, p. 045029 (13pp), Apr. 2011.

[122] L. M. Miller, *Micro-scale piezoelectric vibration energy harvesting: from fixed-frequency to adaptable-frequency devices*. PhD thesis, 2012.

[123] D. Zhu, M. J. Tudor, and S. P. Beeby, "Strategies for increasing the operating frequency range of vibration energy harvesters: a review," *Journal of Measurement Science and Technology*, vol. 21, p. 022001 (29pp), Feb. 2010.

[124] A. G. Mukherjee, P. D. Mitcheson, S. W. Wright, E. M. Yeatman, D. Zhu, and S. P. Beeby, "Magnetic Potential Well Tuning Of Resonant Cantilever Energy Harvester," in *PowerMEMS*, pp. 480–483, 2012.

[125] I. N. Ayala, D. Zhu, M. J. Tudor, and S. P. Beeby, "Autonomous Tunable Energy Harvester," in *PowerMEMS*, pp. 3–6, 2009.

[126] P. Mitcheson, T. Toh, K. H. Wong, S. G. Burrow, and A. S. Holmes, "Tuning the Resonant Frequency and Damping of an Electromagnetic Energy Harvester Using Power Electronics," *IEEE Transactions on Circuits and Systems*, vol. 58, no. 12, pp. 792–796, 2011.

[127] H.-P. Hu, H. Xue, J. Jin, H.-R. Wang, Y.-T. Hu, and X.-D. Chen, "Adjusting the resonant frequency of a segmented energy harvester through circuit connection patterns," *2009 Symposium on Piezoelectricity, Acoustic Waves, and Device Applications (SPAWDA 2009)*, pp. 48–48, Dec. 2009.

[128] S. Roundy, "Toward self-tuning adaptive vibration-based microgenerators," *Proceedings of SPIE*, vol. 5649, pp. 373–384, 2005.

[129] M. Marzencki, M. Defosseux, and S. Basrour, "MEMS Vibration Energy Harvesting Devices With Passive Resonance Frequency Adaptation Capability," *Journal of Microelectromechanical Systems*, vol. 18, no. 6, pp. 1444–1453, 2009.

[130] L. M. Miller, P. Pillatsch, E. Halvorsen, P. K. Wright, E. M. Yeatman, and A. S. Holmes, "Experimental passive self-tuning behavior of a beam resonator with sliding proof mass," *Journal of Sound and Vibration*, vol. 332, pp. 7142–7152, Dec. 2013.

[131] A. Boudaoud, Y. Couder, and M. Ben Amar, "A self-adaptative oscillator," *The European Physical Journal B*, vol. 9, pp. 159–165, May 1999.

[132] E. C. Miranda and J. J. Thomsen, "Vibration Induced Sliding: Theory and Experiment for a Beam with a Spring-Loaded Mass," *Journal of Nonlinear Dynamics*, no. 16, pp. 167–186, 1998.

[133] I. Kozinsky, "Study Of Passive Self-Tuning Resonator For Broadband Power Harvesting," in *PowerMEMS*, pp. 388–391, 2009.

[134] L. Gu and C. Livermore, "Passive self-tuning energy harvester for extracting energy from rotational motion," *Applied Physics Letters*, vol. 97, no. 8, p. 081904 (3pp), 2010.

[135] L. Gu and C. Livermore, "Compact passively self-tuning energy harvesting for rotating applications," *Smart Materials and Structures*, vol. 21, p. 015002 (9pp), Jan. 2012.

[136] T. Petropoulos, E. M. Yeatman, and P. D. Mitcheson, "MEMS coupled resonators for power generation and sensing," in *Micromechanics Europe*, pp. 261–264, 2004.

[137] M. Ferrari, V. Ferrari, M. Guizzetti, D. Marioli, and A. Taroni, "Piezoelectric multifrequency energy converter for power harvesting in autonomous microsystems," *Sensors and Actuators A: Physical*, vol. 142, pp. 329–335, Mar. 2008.

[138] D. Castagnetti, "Experimental modal analysis of fractal-inspired multi-frequency structures for piezoelectric energy converters," *Smart Materials and Structures*, vol. 21, p. 094009 (9pp), Sept. 2012.

[139] A. Marin, J. Turner, D. S. Ha, and S. Priya, "Broadband electromagnetic vibration energy harvesting system for powering wireless sensor nodes," *Smart Materials and Structures*, vol. 22, p. 075008 (13pp), July 2013.

[140] R. L. Harne and K. W. Wang, "A review of the recent research on vibration energy harvesting via bistable systems," *Smart Materials and Structures*, vol. 22, p. 023001 (12pp), Feb. 2013.

[141] S. P. Beeby, L. Wang, D. Zhu, A. S. Weddell, G. V. Merrett, B. Stark, G. Szarka, and B. M. Al-Hashimi, "A comparison of power output from linear and nonlinear kinetic energy harvesters using real vibration data," *Smart Materials and Structures*, vol. 22, p. 075022, July 2013.

[142] C. P. Le, E. Halvorsen, O. Sorasen, and E. M. Yeatman, "Wideband excitation of an electrostatic vibration energy harvester with power-extracting end-stops," *Smart Materials and Structures*, vol. 22, p. 075020 (9pp), July 2013.

[143] A. Abdelkefi, F. Najar, A. H. Nayfeh, and S. Ben Ayed, "An energy harvester using piezoelectric cantilever beams undergoing cou-

pled bending torsion vibrations," *Smart Materials and Structures*, vol. 20, p. 115007 (11pp), Nov. 2011.

[144] Y. Zhu, J. Zu, and W. Su, "Broadband energy harvesting through a piezoelectric beam subjected to dynamic compressive loading," *Smart Materials and Structures*, p. 045007 (13pp), 2013.

[145] J. Yang, Y. Wen, P. Li, X. Dai, and M. Li, "A broadband vibration energy harvester using magnetoelectric transducer," in *Sensors*, pp. 1905–1909, 2010.

[146] W. Jones, B. Alphenaar, and D. Alphenaar, "Passive magnetic coupling to enhance piezoelectric cantilever response in energy scavenging applications," *2008 17th IEEE International Symposium on the Applications of Ferroelectrics*, pp. 1–2, Feb. 2008.

[147] Z. Hadas, C. Ondrusek, and V. Singule, "Power sensitivity of vibration energy harvester," *Microsystem Technologies*, vol. 16, pp. 691–702, Feb. 2010.

[148] M. Ferrari, M. Baù, M. Guizzetti, and V. Ferrari, "A single-magnet nonlinear piezoelectric converter for enhanced energy harvesting from random vibrations," *Sensors and Actuators A: Physical*, vol. 172, pp. 287–292, Dec. 2011.

[149] M. Ferrari, V. Ferrari, M. Guizzetti, B. Andò, S. Baglio, and C. Trigona, "Improved energy harvesting from wideband vibrations by nonlinear piezoelectric converters," *Sensors and Actuators A: Physical*, vol. 162, pp. 425–431, Aug. 2010.

[150] B. Marinkovic and H. Koser, "Demonstration of wide bandwidth energy harvesting from vibrations," *Smart Materials and Structures*, vol. 21, p. 065006 (5pp), June 2012.

[151] A. Hajati, S. P. Bathurst, H. J. Lee, S. G. Kim, F. Dimatix, and S. Clara, "Design and Fabrication of a Nonlinear Resonator for Ultra Wide-Bandwidth Energy Harvesting Applications," in *2011 IEEE 24th International Conference on Micro Electro Mechanical Systems*, pp. 1301–1304, 2011.

[152] A. Hajati and S. G. Kim, "Wide-Bandwidth MEMS-Scale Piezoelectric Energy Harvester," in *PowerMEMS*, 2009.

[153] A. Hajati and S.-G. Kim, "Ultra-wide bandwidth piezoelectric energy harvesting," *Applied Physics Letters*, vol. 99, no. 8, p. 083105, 2011.

[154] F. Cottone, L. Gammaitoni, H. Vocca, M. Ferrari, and V. Ferrari, "Piezoelectric buckled beams for random vibration energy harvesting," *Smart Materials and Structures*, vol. 21, p. 035021 (11pp), Mar. 2012.

[155] S. A. Emam and A. H. Nayfeh, "On the Nonlinear Dynamics of a Buckled Beam Subjected to a Primary-Resonance Excitation," *Nonlinear Dynamics*, vol. 35, pp. 1–17, Jan. 2004.

[156] J. F. Blackburn and M. G. Cain, "Nonlinear piezoelectric resonance: A theoretically rigorous approach to constant I-V measurements," *Journal of Applied Physics*, vol. 100, no. 11, p. 114101, 2006.

[157] Y. Zhang and C. S. Cai, "A retrofitted energy harvester for low frequency vibrations," *Smart Materials and Structures*, vol. 21, p. 075007 (14pp), July 2012.

[158] T. Galchev, H. Kim, and K. Najafi, "Micro Power Generator for Harvesting Low-Frequency and Nonperiodic Vibrations," *Journal of Microelectromechanical Systems*, vol. 20, no. 4, pp. 852–866, 2011.

[159] T. Galchev, H. Kim, and K. Najafi, "Non-resonant bi-stable frequency-increased power scavenger from low-frequency ambient vibration," in *TRANSDUCERS*, pp. 632–635, IEEE, June 2009.

[160] T. Galchev, E. E. Aktakka, H. Kim, and K. Najafi, "A piezoelectric frequency-increased power generator for scavenging low-frequency ambient vibration," in *IEEE 23rd International Conference on Micro Electro Mechanical Systems (MEMS)*, pp. 1203–1206, IEEE, Jan. 2010.

[161] O. Zorlu, E. Topal, and H. Kulah, "A vibration-based electromagnetic energy harvester using mechanical frequency up-conversion method," *Sensors Journal, IEEE*, vol. 11, no. 2, pp. 481–488, 2011.

[162] A. Rahimi, O. Zorlu, A. Muhtaroglu, and H. Külah, "An electromagnetic energy harvesting system for low frequency applications with a passive interface ASIC in standard CMOS," *Sensors and Actuators A: Physical*, vol. 188, pp. 158–166, Dec. 2012.

[163] H. Kulah and K. Najafi, "Energy Scavenging From Low-Frequency Vibrations by Using Frequency Up-Conversion for Wireless Sensor Applications," *IEEE Sensors Journal*, vol. 8, no. 3, pp. 261–268, 2008.

[164] I. Sari, T. Balkan, and H. Külah, "An Electromagnetic Micro Power Generator for Low-Frequency Environmental Vibrations Based on the Frequency Upconversion Technique," *Journal of Microelectromechanical Systems*, vol. 19, pp. 14–27, Feb. 2010.

[165] H. Kulah and K. Najafi, "An electromagnetic micro power generator for low-frequency environmental vibrations," *17th IEEE International Conference on Micro Electro Mechanical Systems. Maastricht MEMS 2004 Technical Digest*, pp. 237–240, 2004.

[166] K. Ashraf, M. H. Md Khir, J. O. Dennis, and Z. Baharudin, "A wideband, frequency up-converting bounded vibration energy harvester for a low-frequency environment," *Smart Materials and Structures*, vol. 22, p. 025018, Feb. 2013.

[167] M. Pozzi, M. S. H. Aung, M. Zhu, R. K. Jones, and J. Y. Goulermas, "The pizzicato knee-joint energy harvester: characterization with biomechanical data and the effect of backpack load," *Smart Materials and Structures*, vol. 21, p. 075023 (8pp), July 2012.

[168] M. Pozzi and M. Zhu, "Plucked piezoelectric bimorphs for knee-joint energy harvesting: modelling and experimental validation," *Smart Materials and Structures*, vol. 20, p. 055007 (10pp), May 2011.

[169] M. Pozzi and M. Zhu, "Characterization of a rotary piezoelectric energy harvester based on plucking excitation for knee-joint wearable applications," *Smart Materials and Structures*, vol. 21, p. 055004 (9pp), May 2012.

[170] P. Janphuang and D. Isarakorn, "Energy harvesting from a rotating

gear using an impact type piezoelectric MEMS scavenger," in *Transducers*, pp. 735–738, 2011.

[171] L. Gu and C. Livermore, "Impact-driven, frequency up-converting coupled vibration energy harvesting device for low frequency operation," *Smart Materials and Structures*, vol. 20, p. 045004 (10pp), Apr. 2011.

[172] L. Gu, "Low-frequency piezoelectric energy harvesting prototype suitable for the MEMS implementation," *Microelectronics Journal*, vol. 42, pp. 277–282, Feb. 2011.

[173] E. Jacquelin, S. Adhikari, and M. I. Friswell, "A piezoelectric device for impact energy harvesting," *Smart Materials and Structures*, vol. 20, p. 105008 (12pp), Oct. 2011.

[174] M. Renaud, P. Fiorini, R. van Schaijk, and C. van Hoof, "An Impact Based Piezoelectric Harvester Adapted to Low Frequency," in *TRANSDUCERS 2009 - 2009 International Solid-State Sensors, Actuators and Microsystems Conference*, pp. 2094–2097, 2009.

[175] M. Renaud, P. Fiorini, and C. van Hoof, "Optimization of a piezoelectric unimorph for shock and impact energy harvesting," *Smart Materials and Structures*, vol. 16, pp. 1125–1135, Aug. 2007.

[176] J. Rastegar and R. Murray, "Novel two-stage piezoelectric-based ocean wave energy harvesters for moored or unmoored buoys," *Proceedings of SPIE*, vol. 7288, p. 8pp, 2009.

[177] J. Rastegar, "Piezoelectric-based power sources for harvesting energy from platforms with low-frequency vibration," *Proc. SPIE 6171, Smart Structures and Materials 2006: Industrial and Commercial Applications of Smart Structures Technologies*, vol. 6171, 2006.

[178] J. L. Fu, Y. Nakano, L. D. Sorenson, and F. Ayazi, "Multi-Axis ALN-On-Silicon Vibration Energy Harvester With Integrated Frequency-Upconverting Transducers," in *IEEE 25th International Conference on Micro Electro Mechanical Systems (MEMS)*, pp. 1269–1272, 2012.

[179] H. Liu, C. Lee, T. Kobayashi, C. J. Tay, and C. Quan, "Piezoelectric MEMS-based wideband energy harvesting systems using a frequency-up-conversion cantilever stopper," *Sensors and Actuators A: Physical*, pp. 1–7, Feb. 2012.

[180] D.-G. Lee, G. P. Carman, D. Murphy, and C. Schulenburg, "Novel Micro Vibration Energy Harvesting Device using Frequency Up Conversion," in *TRANSDUCERS 2007 - 2007 International Solid-State Sensors, Actuators and Microsystems Conference*, pp. 871–874, IEEE, 2007.

[181] Q. C. Tang, X. Y. Xia, and X. X. Li, "Non-Contact Frequency-Up-Conversion Energy Harvester For Durable & Broad-Band Automotive TPMS Application," in *MEMS*, vol. 1, pp. 1273–1276, 2012.

[182] Q. C. Tang, Y. L. Yang, and X. Li, "Bi-stable frequency up-conversion piezoelectric energy harvester driven by non-contact magnetic repulsion," *Smart Materials and Structures*, vol. 20, p. 125011 (6pp), Dec. 2011.

[183] Y. Yang, Q. Tang, and X. Li, "Non-Contact Repulsive-Force Excitation For Highly Endurable Wide Frequency-Range Energy-Harvesting," in *IEEE Transducers*, pp. 687–690, 2011.

[184] H. T. Luong and N. S. Goo, "Use of a magnetic force exciter to vibrate a piezocomposite generating element in a small-scale windmill," *Smart Materials and Structures*, vol. 21, p. 025017 (9pp), Feb. 2012.

[185] A. M. Wickenheiser and E. Garcia, "Broadband vibration-based energy harvesting improvement through frequency up-conversion by magnetic excitation," *Smart Materials and Structures*, vol. 19, p. 065020 (11pp), June 2010.

[186] A. Wickenheiser, "Analysis of Energy Harvesting Using Frequency Up-Conversion by Analytic Approximations," in *Small-scale Energy Harvesting*, 2012.

[187] D. Arnold, S. Das, F. Cros, I. Zana, M. Allen, and J. Lang, "Magnetic Induction Machines Integrated Into Bulk-Micromachined Sili-

con," *Journal of Microelectromechanical Systems*, vol. 15, pp. 406–414, Apr. 2006.

[188] S. Das, D. Arnold, I. Zana, J.-W. Park, M. Allen, and J. Lang, "Microfabricated High-Speed Axial-Flux Multiwatt Permanent-Magnet Generators-Part I: Modeling," *Journal of Microelectromechanical Systems*, vol. 15, pp. 1330–1350, Oct. 2006.

[189] S. Das, D. Arnold, I. Zana, J. Park, J. Lang, and M. Allen, "Multiwatt electric power from a microfabricated permanent-magnet generator," in *18th IEEE International Conference on Micro Electro Mechanical Systems*, pp. 287–290, IEEE, 2005.

[190] F. Herrault, C.-H. Ji, R. Shafer, S.-H. Kim, and M. Allen, "Ultraminiaturized Milliwatt-Scale Permanent Magnet Generators," in *TRANSDUCERS 2007 - International Solid-State Sensors, Actuators and Microsystems Conference*, pp. 899–902, IEEE, 2007.

[191] F. Herrault, B. C. Yen, C.-H. Ji, Z. S. Spakovszky, J. H. Lang, and M. G. Allen, "Fabrication and Performance of Silicon-Embedded Permanent-Magnet Microgenerators," *Journal of Microelectromechanical Systems*, vol. 19, pp. 4–13, Feb. 2010.

[192] F. Herrault, D. P. Arnold, I. Zana, P. Galle, and M. G. Allen, "Multiwatt Microscale Permanent-Magnet Generators Operating at High Temperatures," *INTERMAG 2006 - IEEE International Magnetics Conference*, pp. 597–597, May 2006.

[193] M. Fralick, B. Dick, H. Jazo, R. Waters, and T. Russin, "Characterization and Optimization of a Novel Electromagnetic Transduction Technique for Rotational Energy Harvesting," in *Sensors*, pp. 1869–1874, 2010.

[194] R. J. Hergert, *Rotary Micro-Ball Bearing Designs for MEMS Applications*. PhD thesis, 2013.

[195] T. T. Toh, *A Gravitational Torque Energy Harvesting System For Rotational Motion*. PhD thesis, 2011.

[196] E. Romero, M. Neuman, and R. Warrington, "Rotational energy harvester for body motion," in *2011 IEEE 24th International Conference on Micro Electro Mechanical Systems*, pp. 1325–1328, IEEE, Jan. 2011.

[197] P. Pillatsch, E. M. Yeatman, and A. S. Holmes, "A scalable piezoelectric impulse-excited energy harvester for human body excitation," *Smart Materials and Structures*, vol. 21, p. 115018 (9pp), Nov. 2012.

[198] F. Goldschmidtboeing and P. Woias, "Characterization of different beam shapes for piezoelectric energy harvesting," *Journal of Micromechanics and Microengineering*, vol. 18, p. 104013 (7pp), Oct. 2008.

[199] S. P. Matova, M. Renaud, M. Jambunathan, M. Goedbloed, and R. Van Schaijk, "Effect of length/width ratio of tapered beams on the performance of piezoelectric energy harvesters," *Smart Materials and Structures*, vol. 22, p. 075015 (8pp), July 2013.

[200] D. Zhu, A. Almusallam, S. P. Beeby, J. Tudor, and N. R. Harris, "A Bimorph Multi-Layer Piezoelectric Vibration Energy Harvester," in *PowerMEMS*, 2010.

[201] D. Zhu, S. Beeby, J. Tudor, N. White, and N. Harris, "Improving Output Power of Piezoelectric Energy Harvesters using Multilayer Structures," *Procedia Engineering*, pp. 4–7, 2011.

[202] T.-B. Xu, E. J. Siochi, J. H. Kang, L. Zuo, W. Zhou, X. Tang, and X. Jiang, "Energy harvesting using a PZT ceramic multilayer stack," *Smart Materials and Structures*, vol. 22, p. 065015, June 2013.

[203] J. Dicken, P. D. Mitcheson, A. Elliott, and E. M. Yeatman, "Single-Supply Pre-Biasing Circuit For Low-Amplitude Energy Harvesting Applications," in *PowerMEMS*, 2011.

[204] J. Dicken, P. D. Mitcheson, I. Stoianov, and E. M. Yeatman, "Increased Power Output From Piezoelectric Energy Harvesters By Pre-Biasing," in *PowerMEMS*, pp. 75–78, 2009.

[205] J. Dicken, P. D. Mitcheson, I. Stoianov, and E. M. Yeatman, "Power-Extraction Circuits for Piezoelectric Energy Harvesters in Miniature

and Low-Power Applications," *IEEE Transactions on Power Electronics and Industrial Electronics*, 2012.

[206] H. Xu and M. Ortmanns, "A Temperature and Process Compensated Ultralow-Voltage Rectifier in Standard Threshold CMOS for Energy-Harvesting Applications," *IEEE Transactions on Circuits and Systems II*, vol. 58, no. 12, pp. 812–816, 2011.

[207] A. Romani, M. Tartagni, E. Sangiorgi, and R. P. Paganelli, "An energy autonomous switching converter for harvesting power from multiple piezoelectric transducers," in *2010 IEEE Sensors*, pp. 1173–1176, IEEE, Nov. 2010.

[208] C. Shi, B. Miller, K. Mayaram, and T. Fiez, "A multiple-input boost converter for low-power energy harvesting," *IEEE Transactions on Circuits and Systems*, vol. 58, no. 12, pp. 827–831, 2011.

[209] P. Pillatsch, E. M. Yeatman, and A. S. Holmes, "Piezoelectric Rotational Energy Harvester for Body Sensors Using an Oscillating Mass," in *Ninth Int. Conf. on Wearable and Implantable Body Sensor Networks*, pp. 6–10, 2012.

[210] P. Pillatsch, E. M. Yeatman, and A. S. Holmes, "A Wearable Piezoelectric Rotational Energy Harvester," in *Tenth Int. Conf. on Wearable and Implantable Body Sensor Networks*, pp. 1–6, 2013.

[211] P. Pillatsch, E. M. Yeatman, and a. S. Holmes, "Real World Testing Of A Piezoelectric Rotational Energy Harvester For Human Motion," *Journal of Physics: Conference Series*, vol. 476, p. 012010 (5pp), Dec. 2013.

[212] P. Pillatsch, E. M. Yeatman, and A. S. Holmes, "A piezoelectric frequency up-converting energy harvester with rotating proof mass for human body applications," *Sensors and Actuators A: Physical*, vol. 206, pp. 178–185, Oct. 2013.

[213] Q. M. Zhang and J. Zhao, "Electromechanical properties of lead zirconate titanate piezoceramics under the influence of mechanical stresses.," *IEEE transactions on ultrasonics, ferroelectrics, and frequency control*, vol. 46, pp. 1518–26, Jan. 1999.

[214] M. Bhattacharyya and A. Arockiarajan, "Electrical fatigue behaviour in lead zirconate titanate: an experimental and theoretical study," *Smart Materials and Structures*, vol. 22, p. 085032 (12pp), Aug. 2013.

[215] I. Rodriguez, T. Moise, S. Summerfelt, R. Udayakumar, S. Gilbert, and C. Dunn, "Empirical Model for Fatigue of PZT Ferroelectric Memories," in *IEEE, 40th Annual International Reliability Physics Symposium*, pp. 39–44, 2002.

[216] S. Sherrit, C. M. Jones, J. B. Aldrich, C. J. Blodget, J. D. Moore, J. W. Carson, R. Goullioud, and B. Jau, "Piezoelectric stack actuator life test," *2011 Aerospace Conference*, pp. 1–8, Mar. 2011.

[217] S. Sherrit, X. Bao, C. M. Jones, J. B. Aldrich, C. J. Blodget, J. D. Moore, J. W. Carson, and R. Goullioud, "Piezoelectric multilayer actuator life test," *IEEE transactions on ultrasonics, ferroelectrics, and frequency control*, vol. 58, pp. 820–8, Apr. 2011.

[218] M. Laurent, H. Bödinger, T. Steinkopff, K. Lubitz, and C. Schuh, "Limitation of the Degradation Effect in Piezoelectric Multilayer Actuators with Ceramic Layer Thickness below 50 um," in *IEEE International Ultrasonics, Ferroelectrics, and Frequency Joint 50th Anniversary Conference*, pp. 3–6, 2004.

[219] B. Zickgraf, "Fatigue behaviour of multilayer piezoelectric actuators," *IEEE*, pp. 325–328, 1991.

[220] N. Jiang, J. Liu, T. Tao, and L. Han, "Fatigue evaluation of piezo impact drive mechanism," *Micro-NanoMechatronics*, no. 6, pp. 255–259, 2007.

[221] M. G. Cain, M. Stewart, and M. G. Gee, "Degradation of Piezoelectric Materials," Tech. Rep. January, NPL, 1999.

[222] P. Pillatsch, E. M. Yeatman, and a. S. Holmes, "Magnetic plucking of piezoelectric beams for frequency up-converting energy harvesters," *Smart Materials and Structures*, vol. 23, p. 025009 (12pp), Feb. 2014.

[223] S. Priya, "Modeling of electric energy harvesting using piezoelectric windmill," *Applied Physics Letters*, vol. 87, no. 18, p. 184101, 2005.

[224] J. Ajitsaria, S. Y. Choe, D. Shen, and D. J. Kim, "Modeling and analysis of a bimorph piezoelectric cantilever beam for voltage generation," *Smart Materials and Structures*, vol. 16, pp. 447–454, Apr. 2007.

[225] J. Kim, B. Grisso, J. Kim, D. Sma Ha, and D. Inman, "Electrical modeling of piezoelectric ceramics for analysis and evaluation of sensory systems," in *IEEE Sensors Applications Symposium*, pp. 122–127, 2008.

[226] P. Dalzell and P. Bonello, "Analysis of an energy harvesting piezoelectric beam with energy storage circuit," *Smart Materials and Structures*, vol. 21, p. 105029 (12pp), Oct. 2012.

[227] F. Lu, H. P. Lee, and S. P. Lim, "Modeling and analysis of micro piezoelectric power generators for micro-electromechanical-systems applications," *Smart Materials and Structures*, vol. 13, pp. 57–63, Feb. 2004.

[228] R. Ballas, *Piezoelectric Multilayer Beam Bending Actuators*. Springer, 2007.

[229] G. Buchberger and J. Schoeftner, "Modeling of slender laminated piezoelastic beams with resistive electrodes-comparison of analytical results with three-dimensional finite element calculations," *Smart Materials and Structures*, vol. 22, p. 032001 (13pp), 2013.

[230] Y. Liao and H. Sodano, "Optimal placement of piezoelectric material on a cantilever beam for maximum piezoelectric damping and power harvesting efficiency," *Smart Materials and Structures*, vol. 21, p. 105014 (9pp), Oct. 2012.

[231] A. Erturk and D. J. Inman, "An experimentally validated bimorph cantilever model for piezoelectric energy harvesting from base excitations," *Smart Materials and Structures*, vol. 18, p. 025009 (18pp), Feb. 2009.

[232] S. S. Rao, *Vibrations of continuous systems*. John Wiley & Sons, 2007.

[233] W. C. Young, *Roark's Formulas for Stress & Strain*. McGraw-Hill, 2002.

[234] G. Akoun and J.-P. Yonnet, "3D Analytical Calculation Of The Forces Exerted Between Two Cuboidal Magnets," *IEEE Transactions on Magnetics*, vol. 20, no. 5, pp. 1962–1964, 1984.

[235] H. Choi, I. Park, and S. Lee, "Force Calculation of Magnetized Bodies in Contact Using Kelvin's Formula and Virtual Air-Gap," *IEEE Transactions on Applied Superconductivity*, vol. 16, pp. 1832–1835, June 2006.

[236] D. Vokoun, M. Beleggia, L. Heller, and P. Šittner, "Magnetostatic interactions and forces between cylindrical permanent magnets," *Journal of Magnetism and Magnetic Materials*, vol. 321, pp. 3758–3763, Nov. 2009.

[237] B. D. Cullity and C. D. Graham, *Introduction to Magnetic Materials*. IEEE, 2009.

[238] J. Coey, *Magnetism And Magnetic Materials*. Cambridge University Press, 2010.

[239] A. Cammarano, *Increasing the Bandwidth of Resonant Vibration-Based Energy Harvesters*. PhD thesis, 2012.

[240] P. Pillatsch, E. M. Yeatman, and A. S. Holmes, "P54821GB Power Generation Device, filing number 1207987.7," May 2012.

[241] P. Pillatsch, L. M. Miller, E. Halvorsen, P. K. Wright, E. M. Yeatman, and a. S. Holmes, "Self-tuning behavior of a clamped-clamped beam with sliding proof mass for broadband energy harvesting," *Journal of Physics: Conference Series*, vol. 476, p. 012068 (5pp), Dec. 2013.

[242] P. Pillatsch, E. M. Yeatman, and A. S. Holmes, "A Model For Magnetic Plucking Of Piezoelectric Beams In Energy Harvesters," in *The 17th International Conference on Solid-State Sensors, Actuators and Microsystems, Transducers*, pp. 1364–1367, 2013.

[243] P. Pillatsch, E. M. Yeatman, and A. S. Holmes, "Magnetic Beam Plucking In A Piezoelectric Energy Harvester With Rotating Proof Mass," in *PowerMEMS*, pp. 476–479, 2012.

[244] P. Pillatsch, E. M. Yeatman, and A. S. Holmes, "A scalable piezoelectric impulse-excited generator for random low frequency excitation," in *IEEE MEMS*, vol. 21, pp. 1205–1208, Nov. 2012.

[245] P. Pillatsch, E. M. Yeatman, and A. S. Holmes, "Piezoelectric impulse-excited generator for low frequency non-harmonic vibrations," in *PowerMEMS*, pp. 1–4, 2011.